Doctoral Dissertations   Student Scholarship

Fall 2008

An analysis of reconnection dynamics in an eruptive flare model

Daniel B. Seaton
University of New Hampshire, Durham

AN ANALYSIS OF RECONNECTION DYNAMICS IN AN ERUPTIVE FLARE MODEL

BY

DANIEL B. SEATON

B.A., Williams College (2001)

DISSERTATION

Submitted to the University of New Hampshire
in partial fulfillment of
the requirements for the degree of

Doctor of Philosophy

in

Physics

September 2008

UMI Number: 3333527

INFORMATION TO USERS

®
UMI
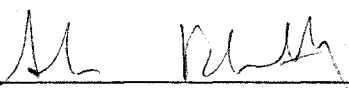
This dissertation has been examined and approved.
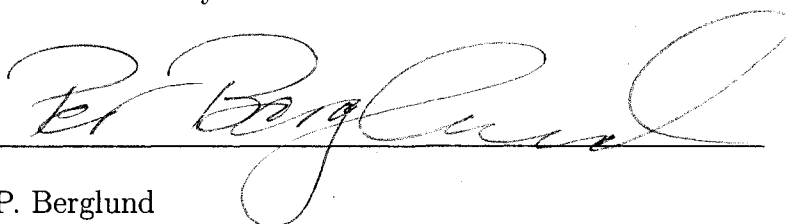
Dissertation director, T. G. Forbes
Research Professor of Physics

A. Bhattacharjee
Professor of Physics

P. Berglund
Assistant Professor of Physics

B. D. G. Chandran
Associate Professor of Physics

D. C. Meredith
Associate Professor of Physics

5/21/08

Date

ACKNOWLEDGMENTS

Many people have contributed to both my success in graduate school and this research project. Most notably, I would like to thank my thesis advisor, Terry Forbes, for being both an exceptional mentor and colleague. Kathy Reeves offered good advice and lots of help, especially with the work described in chapter 3. Others who have been supportive colleagues, professionally and personally, and who have generally kept me entertained and sane throughout my time at UNH include Phil Isenberg, Marty Lee, Yong Liu, Monica Bobra, Jack O'Reilly, Deans Harry Richards and Cari Moorhead, and Jessie Knapp and other members of the Graduate Student Organization.

I would also like to thank those who have served as mentors and friends and have helped me develop as a scientist: John Gaustad, Bruce Partridge, Leon Golub, Ed Deluca, Karen Kwitter, and Jay Pasachoff.

Thanks especially to my parents and family, my friends, and most of all, my wife Mindi, without whose love and support none of this would have been possible.

TABLE OF CONTENTS

LIST OF TABLES

LIST OF FIGURES

ABSTRACT

AN ANALYSIS OF RECONNECTION DYNAMICS IN AN
ERUPTIVE FLARE MODEL

by

Daniel B. Seaton
University of New Hampshire, September, 2008

This dissertation develops a one-dimensional, analytic model for current sheets that form during solar flares. The model uses a method developed by B. V. Somov & V. S. Titov for Petschek-type reconnection. The first part of this dissertation provides a detailed analysis of the Somov-Titov model, its assumptions, strengths and weaknesses. We consider the role of both the diffusion region and nonuniform resistivity in the generation of Petschek-type solutions.

The second part of this dissertation extends the averaging method to the dynamics of an asymmetric current sheet during a solar flare. We determine the location of the x-line and the distribution of incoming Poynting flux into upward and downward directed reconnection jets. We find that, except at the very beginning of a flare when the current sheet is most symmetric, the x-line is generally located near the lower tip of the sheet. We predict that it should be low enough in the corona to be observed by X-ray and EUV telescopes. We find that in most cases the majority of incoming flux exits the current sheet through the upward jet, in contrast to previous studies that assumed as much as 50% of the incoming flux is directed into the downward jet and flare ribbons.

In the third part, we integrate thermal conduction into the Somov-Titov framework using a slow-shock model that includes conduction, and allows us to describe the thermal halo that surrounds the current sheet because of heat flow across the current sheet boundary. We find that thermal conduction has a significant effect on the fast-mode mach number of the

reconnection outflow, producing mach numbers as high as 7 for solar-flare conditions, three times greater than previously calculated. We conclude that these termination shocks are considerably more efficient at producing particle acceleration than previously thought since the efficiency of particle acceleration at shocks increases dramatically with Mach number. We compare this model with numerical simulations by T. Yokoyama & K. Shibata and find good agreement.

CHAPTER 1

INTRODUCTION

1.1   Introduction to Solar Eruptions

The Sun is a relatively ordinary star, one of nearly 100 million G2V stars in our galaxy, which puts it approximately in the middle of the main sequence on the Hertzspring-Russell diagram where most stars spend the majority of their lives. Like other stars similar to it, the Sun is essentially a sphere made of plasma, surrounded by a more irregular atmosphere, the solar corona. While the surface of the Sun, the photosphere, is about 5800 K, temperatures in the corona can reach 100 million K, especially during solar eruptions. These eruptions, commonly referred to as coronal mass ejections and solar flares, generally unfold in the corona, and are responsible for heating the plasma there to such high temperatures.

The entire Sun is permeated by complex magnetic fields, which undergo evolution in activity over the course of a cycle of approximately 11 years. These fields are generated by a magnetic dynamo at the center of the Sun, and become "frozen in" to the plasma that makes up the Sun due to it's high conductivity. During periods of inactivity, referred to as solar minima, the Sun's magnetic field is essentially a dipole, but this magnetic structure becomes increasingly complicated as the solar cycle unfolds. Because the magnetic field is frozen into the plasma that makes up the Sun, fields are dragged along with the rotation of the Sun. Because the Sun rotates faster at its equator than at its poles, the magnetic field becomes increasingly stretched out as the Sun

rotates, eventually becoming twisted and complex at solar maximum. This period of increased activity is generally characterized by the appearance of many sunspots in the photosphere and many eruptions in the corona. Over time, these eruptions provide a mechanism for releasing the stress on the Sun's magnetic field, eventually allowing it to return to the simpler configuration seen during solar minimum.

The mechanisms that trigger these eruptions and allow the reconfigurations of the magnetic fields that drive them are not completely understood. Our work here is based on a loss-of-equilibrium mechanism (see Section 1.2.2) that causes the solar magnetic field lines to become highly stretched. The process that allows these stretched field lines to relax is referred to as magnetic reconnection. Reeves (2006) and Lin (2001) previously studied the loss of equilibrium mechanism that triggers and drives the eruptions, but they did not formally model the reconnection process itself. It is this process that will be a principal focus of the rest of this dissertation.

In fact, there are many processes on the Sun in which reconnection plays an important role, with eruptions only serving as the most prominent—and, perhaps, dramatic—example. Although a primary goal of this project is to inject realistic reconnection physics into the models of coronal mass ejections and solar flares described by Reeves and Lin, our results could also be applied, at least in principle, to other phenomena involving reconnection.

1.1.1 Solar Flares

Solar flares were first observed in 1859 in white-light. While conducting observations of sunspots, Carrington (1859) observed a transient brightening on the disk of the Sun that lasted a few minutes. This event was simultaneously observed by Hodgson (1859), and was, Carrington noted, followed by a considerable magnetic storm later in the day. Because the sunspot group remained essentially unchanged after the

event, Carrington concluded that whatever he had observed had occurred above the photosphere.

The flare that Carrington observed must have been a very large one, because flares large enough to be visible in white-light are relatively rare (Neidig & Cliver, 1983). Flares are much more commonly seen in narrow pass-band instruments centered on the Hα hydrogen line. The majority of solar emission in this line comes from the chromosphere—in fact, it is the bright red appearance of this line from which the chromosphere takes its name (Golub & Pasachoff, 2001). Light curves for the Hα emission during a flare as a function of time (see Figure 1-1) have a number of classic characteristics. First, in the impulsive phase, there is a sudden increase in emission at the beginning of the event. This is followed by a gradual decline in emission back to the background levels over several hours; this is called the decay phase. Flares with long decay phases are usually refered to as long duration events (LDEs), while flares with short decay times are often refered to as compact or impulsive flares. Generally, these compact flares occupy only a small region, while LDEs are large in extent and are characterized by double ribbons of bright Hα emission (see Figure 1-1). For this reason, LDEs are sometimes referred to as "two-ribbon flares" (Moore et al., 1980). As the event progresses, these ribbons gradually separate at speeds of a couple of km s^{-1} (Dodson, 1949; Servajean & Olivieri, 1946). After an acceleration at the beginning of the event, the velocities remain constant or decrease slightly as the flare progresses (Dodson, 1949; Malville & Moreton, 1963).

The location and orientation of flare ribbons in the larger corona helps shed some light on the role of magnetic fields in the overall evolution of the flare. Flare ribbons generally form parallel to the boundary between regions of opposite magnetic polarity, which is commonly referred to as the magnetic neutral line (Martres et al., 1966). Magnetic loops that appear to connect these ribbons often appear in the Hα passband,

3

chromosphere

BBSO

$H\alpha$

original plage intensity

corona

Yohkoh

soft X-rays

nonthermal

RHESSI

hard X-rays

UT
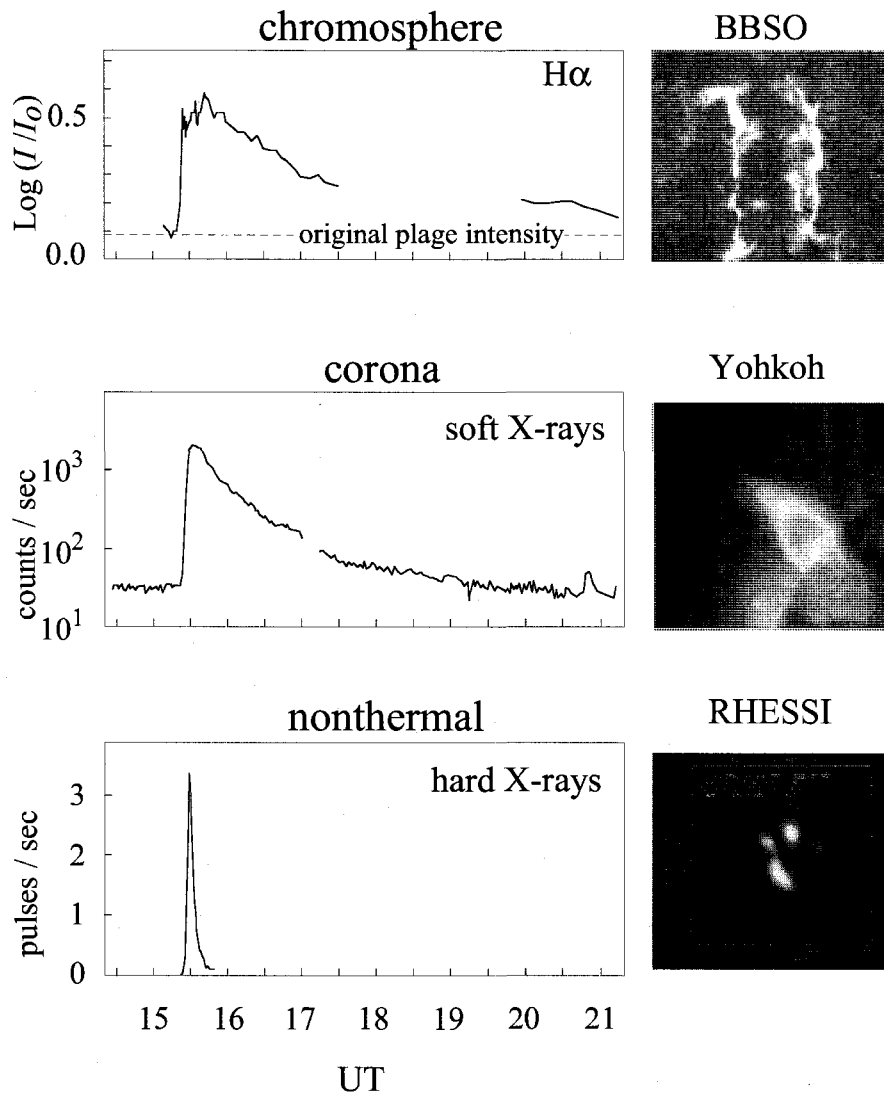
Figure 1-1: Light curves in three passbands—$H\alpha$, soft X-rays and hard X-rays—for a flare from August 28, 1966, and images of the types of features commonly associated with such emission from different events. (Figure from Forbes, 2003, used with permission.)

so we can conclude that these loops are filled with relatively cool plasma (relative to the surrounding corona) with temperatures on the order of 10^4 K. During the early phases of the flare, these loops form at an acute angle to the neutral line, which suggests the presence of sheared magnetic fields (Zirin & Tanaka, 1973; Tanaka & Nakagawa, 1973). Loops that form later in the events generally are perpendicular to the neutral line, which suggests that a more relaxed field has developed: this is consistent with the idea that the sheared field has released its stored energy during the course of the event.

More recently, a number of space-based telescopes have allowed the observation of much higher temperature plasma that emits in the ultraviolet and X-ray wavelengths. The earliest of these X-ray missions was the S-054 X-ray Telescope onboard the orbiting space station *Skylab*. Observations by Vaiana et al. (1973) using this telescope revealed emission bridging the gap between Hα flare ribbons, which showed that the flare ribbons are merely footpoints of loops that are too hot to be seen in Hα. Subsequent observations of flares in soft X-rays using a variety of instruments revealed that hot loops form higher in altitude than their companions in Hα (Moore et al., 1980; Svestka et al., 1987; Harra-Murnion et al., 1998). Figure 1-1 shows observations of such high temperature loops from the Soft X-ray Telescope on the *Yohkoh* satellite.

Flares are also associated with other types of high energy, non-thermal radiation. When high energy particles collide with the chromosphere at flare loop footpoints they generate hard X-rays via thermal *bremsstrahlung*. These X-rays are frequently observed during flares (as in Takakura et al., 1995). Hard X-ray radiation is also observed at loop-tops during flares (Masuda et al., 1994). There appears to be a correlation between these hard X-rays and the derivative of the soft X-ray light curve (Tanaka et al., 1982; Starr et al., 1988; Dennis & Zarro, 1993). This correlation is usually referred to as the Neupert effect, after Neupert (1968), who discovered a

similar relationship between microwave emissions and the derivative of the soft X-ray light curve. In both cases, the cause of the radaition is thought to be the same population of accelerated particles.

1.1.2 Coronal Mass Ejections

Although Carrington had noted a possible correlation between solar flares and magnetic storms on Earth as early as his first observation of a solar flare, Chapman & Ferraro (1931) offered the first formal theory of the nature of these terrestrial disturbances. They proposed that the connection between solar activity and magnetic storms on Earth could be explained if this activity was associated with the impact of ionized material ejected by the Sun during a flare on the Earth's magnetic field. After the advent of the space age, Demastus et al. (1973), who observed "dramatic transient events" in the 5303 Å coronal line using the Sacramento Peak Observatory coronagraph, Tousey et al. (1973), who observed using the *OSO-7* coronagraph, and Gosling et al. (1974), who observed with the coronagraph on *Skylab*, confirmed the ejections of ionized clouds at velocities of 400–1000 $km\,s^{-1}$ outwards from the Sun. These explosions of ionized gase came to be known as Coronal Mass Ejections (CMEs). Figure 1-2 shows one example of CME evolution observed by the Large Angle and Spectrometric Coronagraph (LASCO) onboard the *Solar and Heliospheric Observatory (SOHO)*.

More recent coronagraph observations show that CMEs can have an even wider range of velocities than the initial observations suggested, with speeds as slow as 50 $km\,s^{-1}$ and as fast as 3200 $km\,s^{-1}$. The CMEs that occurred around Halloween 2003 had measured speeds as fast as 3000 $km\,s^{-1}$ Gopalswamy et al. (2005a), which were only surpassed by an event on 20 January 2005, which may have been as fast as about 3700 $km\,s^{-1}$ (Gopalswamy et al., 2005b). Because of the wide range of
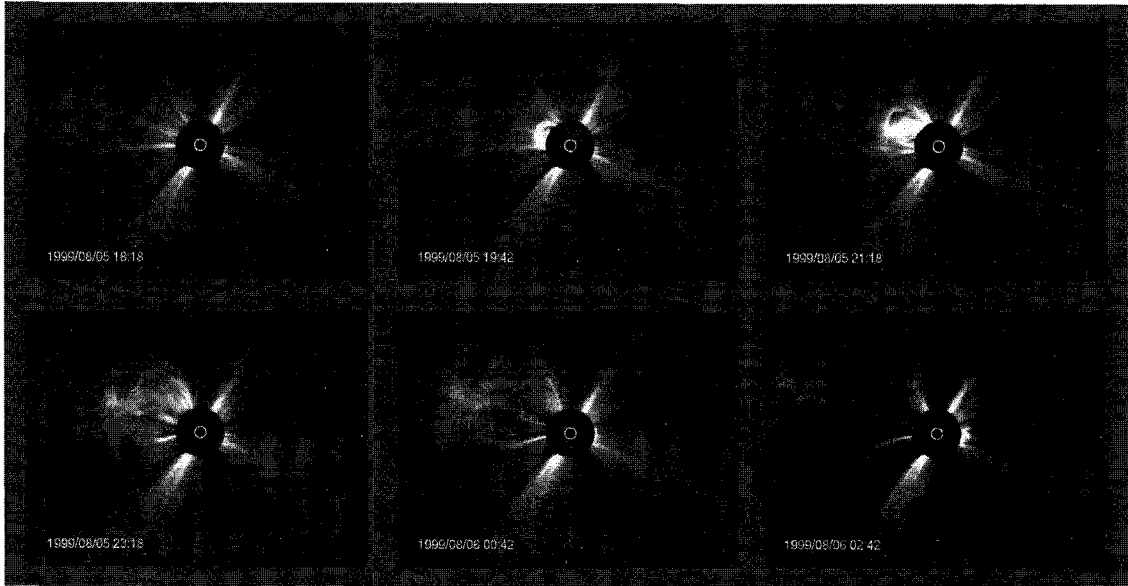
Figure 1-2: The evolution of a CME observed with LASCO onboard the *SOHO* spacecraft. (Figure from the *SOHO*-LASCO consortium.)

speeds of CMEs, they are generally classified into two categories: gradual CMEs, the slower speed events which have measurable accelerations in coronagraph observations, and impulsive CMEs, the high speed events that tend to slow down as they move through coronagraph fields of view (MacQueen & Fisher, 1983; Sheeley et al., 1999; Moon et al., 2002). Recent work by (Vršnak et al., 2005), however, has suggested that instead of two distinct classes of CMEs, the variation in properties make up a continuum of CME behavior.

Long-term statistical studies of CMEs using instruments such as *P78-1*, the *Solar Maximum Mission (SMM)*, and *SOHO*, as well as ground-based coronagraphs, have revealed the connection between the solar cycle and CME properties. Hildner et al. (1976) used *Skylab* data to uncover a correlation between the average sunspot number and the likelihood of CMEs occurring. Later, Webb & Howard (1994) confirmed this relationship using data taken from a number of coronagraphs. A further connection between solar activity and CMEs was presented by Howard et al. (1986), who

found that CMEs generally originate at the same latitudes as helmet streamers—low latitudes during solar minimum conditions and high latitudes during solar maximum.

1.1.3 Prominence Eruptions

Prominences are clouds of cool, dense material, similar to that of the chromosphere, but which are magnetically suspended in the corona, generally forming above the magnetic neutral line (Martin, 1973). In Hα observations, they appear as bright emission features when observed on the limb of the Sun, and dark absorption features, referred to as filaments, when viewed on the disk. When prominences form in quiet regions of the Sun they are called quiescent prominences, but they can form in both quiet and active regions of the Sun. Active region prominences generally form at low altitudes, while quiescent prominces form higher (Tang, 1987). Prominences in quiet regions are generally straight in shape and are long-lived, while active region prominences are often curved and evolve faster than their quiescent counterparts (Low, 1996).

Erupting prominences, called "*disparitions brusques*" (sudden disappearances) by D'Azambuja (1955), were first reported based on daily spectroheliogram observations from the Meudon Observatory in Paris. D'Azambuja found that prominences often erupt and reform in the same place, frequently more than once. Both quiescent and active region prominences can erupt, but, while active region eruptions are almost always associated with a solar flare, quiescent prominences are rarely associated with a flare (Jing et al., 2004). On the other hand, both types of eruptions are associated with a CME about half of the time (Jing et al., 2004).

1.1.4 Are Flares and CMEs Related?

Carrington did not observe a CME when he observed his flare in 1859, but he clearly recognized the connection between geomagnetic activity and the flare. (In hindsight,

it seems clear that his flare was associated with a CME, and he was correct in noticing this correlation.) Although he was careful not to draw too strong a conclusion from his observations, others also noticed a similar relatioship between solar activity and geomagnetic effects (Hale, 1931; Newton, 1943). Eventually, it became clear that geomagnetic activity was caused by material that had been expelled from the Sun (Gold, 1962).

The exact nature of the connection between flares and CMEs has been an outstanding problem ever since. One of the earliest studies, by Munro et al. (1979), used the coronagraph on *Skylab* to survey CMEs and found that about 40% of them were associated with observed flares, while 70% were associated with filament eruptions. More recently, studies using the coronagraph on *SMM* found a similar relationship (Webb & Hundhausen, 1987; St. Cyr & Webb, 1991). Thus it is clear that CMEs can occur without an associated flare. Similarly, many flares, espcially small flares and the even smaller microflares and nanoflares, occur without the observation of a CME, but may contribute to the heating of the corona (Golub & Pasachoff, 1997; Priest & Forbes, 2000). Flares of this type are too small to cause an eruption, but may be linked to eruptions by contributing to the destabilization of the flux rope that leads to a CME and larger flare (Sterling & Moore, 2005).

This relationship (or, perhaps, occasional lack of a relationship) established, the question became: what are the conditions under which a CME will be associated with a flare? Observations using the coronagraph on *Skylab* suggested that the CMEs most likely to be associated with flares were fast CMEs, with an average speed of 775 $km\,s^{-1}$. Meanwhile, CMEs that were associated with prominence eruptions were generally slower, averaging only 330 $km\,s^{-1}$ (Gosling et al., 1976). Other observations with other instruments, including the K-coronameter at the Mauna Loa Observatory (MacQueen & Fisher, 1983) and LASCO on *SOHO* (Sheeley et al., 1999; Moon et al.,

2002) have confirmed the relationship between fast CMEs and flares.

Conversely, some authors have investigated whether the flares that tend to be associated with CMEs have anything in common. Sheeley et al. (1975) compared observations from *Skylab* with observations from the X-ray flux monitor on the *SOLRAD* spacecraft and found that long-lasting soft X-ray flares are almost always associated with CMEs. Later Sheeley et al. (1983) revisited the question and found a correlation between the duration of a flare and the probability it will be accompanied by a CME. However, other studies using later missions such at *Solwind* (Kahler et al., 1989) and *SMM* (Harrison, 1991) found that CMEs occur with both impulsive and long-duration flares, shedding doubt on the proposition that CMEs only occur with long-lived flares.

Because coronagraphs cover the disc of the Sun—and often a good deal more space—it is often impossible to see the initiation of a CME, and thus determining the relative timing of a CME and flare is a difficult task. Harrison (1986; 1991) and collaborators (Harrison et al., 1985, 1990) studied this problem using *SMM* by assuming CMEs accelerate at a constant rate and extrapolating CMEs backwards to estimate their origins. They concluded that CMEs generally begin before the onset of the flare. Other observations with *SMM* and the Mauna Loa Coronameter did manage to estimate the initiation of the CME to within about 10 minutes and showed similar results to the Harrison observations (Kahler, 1992). Zhang et al. (2001) followed CME evolution using LASCO and the Extreme-Ultraviolet Imaging Telescope (EIT) on board *SOHO* to conclude that CME initiation occurs before the associated flare.

1.2 Theories of Solar Eruptions

After the first direct observations of CMEs in 1972, many researchers concluded that CMEs must be caused by the expansion of the hot plasma produced by large flares.

In light of the more recent work on the connection between CMEs and flares, we now know this is not the case. Gosling (1993), for example, shows that on 20% of all CMEs are associated with large flares. Further, as we discussed above, CMEs often appear to begin before the onset of their associated flare. Finally, the thermal energy produced by flares is insufficient to accelerate CMEs to the high speeds they often achieve (Canfield et al., 1980; Webb et al., 1980; Linker et al., 1990). Most contemporary theories of CMEs hold that they are produced by a loss of stability of an equilibrium of the coronal magnetic field. As magnetic flux constantly bubbles up from the convection zone of the Sun, just below the photosphere, the motion of the footpoints of coronal structures causes a buildup of stress in the field. When these stresses exceed the equilibrium point of the field, stability is lost and the field erupts. It is the eruption that releases stored magnetic energy, accelerating the CME and heating the plasma and causing a flare. The process that releases this energy is referred to as reconnection.

1.2.1 Reconnection and Solar Eruption Models

Reconnection of field lines of opposite polarity as a mechanism for releasing the energy necessary to heat coronal plasma and cause a flare was first proposed by Carmichael (1964) in order to explain the reason for flare ribbons to separate in time. Carmichael's theory was later extended by Sturrock (1968) and Kopp & Pneuman (1976) in order to include observations of expanding post-flare loop systems. These papers argued that a rising reconnection site in the corona will continually create new, reconnected magnetic loops and that these loops create the observed flare loop system. According to these theories, the apparent expansion of a flare loop system is actually due to the continued appearance of new and increasingly large loops of hot plasma, rather than the expansion of a single, hot loop.

When field lines reconnect, stored magnetic energy is converted to heat, and transported along field lines into the chromosphere, which leads to the ablation of chromospheric plasma. This process is often called "chromospheric evaporation." There are two models that attempt to explain the physical process by which chromospheric evaporation occurs. The first suggests heating is caused by the impact of accelerated particles on the chromosphere (Lin & Hudson, 1976; Emslie et al., 1981; Fletcher & Martens, 1998), while the second argues thermal energy is conducted along magnetic field lines and into the chromosphere (Hirayama, 1974; Antiochos & Sturrock, 1978; Forbes & Acton, 1996; Yokoyama & Shibata, 2001). Figure 1-3 shows the Forbes & Acton version of this model.

The Forbes & Acton model shown in the figure accounts for a number of important features of observed flares. In particular, there are many observations that show that the hot X-ray loops appear above the cooler Hα loops in a postflare loop arcade (Moore et al., 1980; Svestka et al., 1987; Harra-Murnion et al., 1998). In this model, the hottest loops are the newly formed loops closest to the reconnection site, while the loops lower in altitude, and further from the reconnection, have cooled somewhat. It also explains observations of shrinkage—the observed relaxation of cusp shape loops into more rounded loops which has been observed by both SXT on *Yohkoh* (Hiei & Hundhausen, 1996) and XRT on board *Hinode* (Reeves et al., 2008b).

Reconnection also plays a role in prominent theories of CMEs. These theories can be divided into two classes, directly driven models and energy storage models (Klimchuk, 2001). In directly driven models, the energy necessary to accelerate the CME is injected directly into the corona from below the solar surface, while energy storage models assume that magnetic energy is stored in the corona until a loss of equilibrium occurs, releasing this stored energy and causing a CME.

Most versions of directly driven models have been discounted by modern observa-

super hot or
nonthermal

current sheet

Mach 2 outflow

isothermal slow shock
fast shock

conduction front

x-ray loops (10^7 K)

Hα loops (10^4 K)

evaporation

chromosphere

ribbon
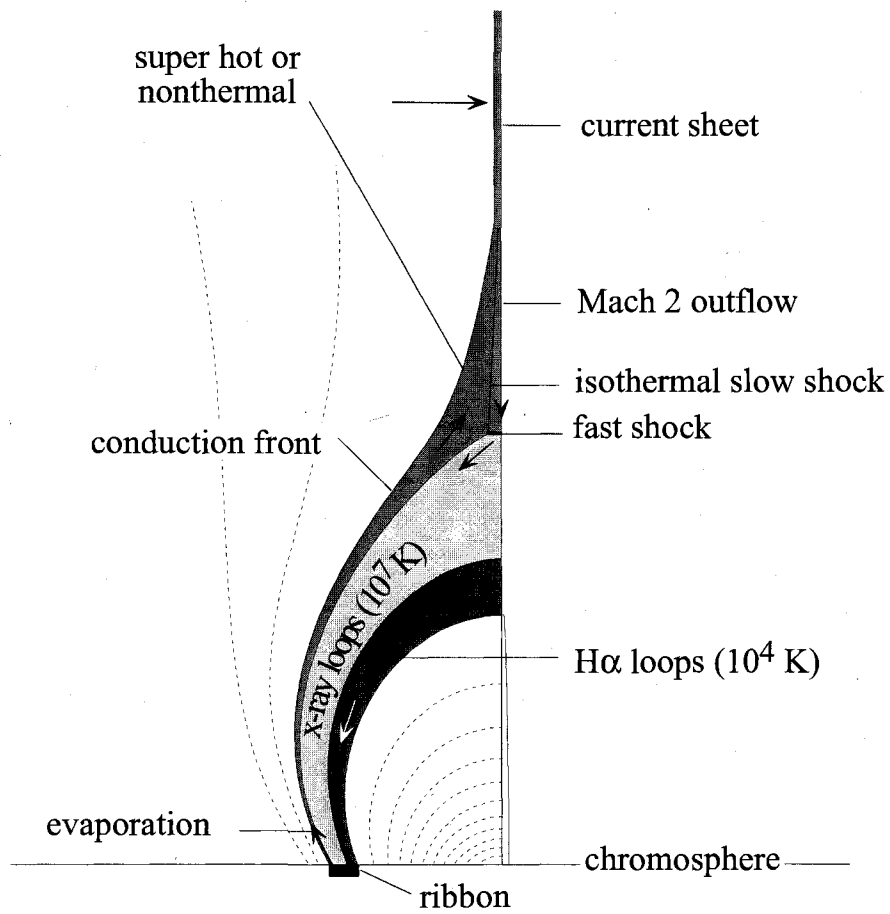
Figure 1-3: A schematic of a flare that includes reconnection and chromospheric evaporation. (Figure adapted from Forbes, 2003, used with permission.)

tions. Some models used the energy released by a solar flare to drive the CME (Wu et al., 1975; Wu, 1982; Dryer, 1982), which requires that the flare preceeds the CME. We have already discussed that most observations show that flares follow CMEs, which leaves most of these models unworkable. Other directly driven models suppose that a sudden increase in current due to motions of plasma below the Sun's surface causes a CME (Sen & White, 1972; Kan et al., 1983). Such models also would require easily detectable flows over a large area of the photosphere, but such flows are not seen (Forbes, 1993).

There are three classes of energy storage models that are viable. The first, the "breakout model" is driven by reconnection above a quadrupolar coronal magnetic field caused by shearing of the inner arcade (Antiochos et al., 1999; MacNeice et al., 2004). This reconnection removes the overlying field, and allows an eruption. As the eruption progresses, an x-line forms under the erupting flux rope and reconnection at this x-line allows the eruption to accelerate. A second class of CME models, the SAIC CME initiation model also depends on sheared arcades (Linker & Mikic, 1995; Linker et al., 2001). This is a 2.5D numerical model in which flux cancellation in a sheared arcade causes the eruption. This model is closely related to the loss-of-equilibrium model below.

1.2.2 Loss-of-Equilibrium Models

In the loss-of-equilibirum—or catastrophe, as they are sometimes called—models, magnetic energy is stored in a flux rope which evolves quasi-statically until the mechanical equilibrium of the stressed magnetic field is lost and the flux rope erupts. This model dates to conceptual models first developed by van Tend & Kuperus (1978) and van Tend (1979). In this model, a flux rope is balanced in the corona by compression and tension forces. When the current in the flux rope reaches a critical value

the equilibrium disappears. Later this model was developed into a "circuit model" by Martens & Kuin (1989), who treated the flux rope like a wire suspended in the corona. Here, the loss of equilibrium occurs when motions of magnetic field in the photosphere cause an increase in coronal flux.

More recently, a two-dimensional magnetohydrodynamic (MHD) version of the catastrophe model has been developed by van Ballegooijen & Martens (1989) and Forbes and a number of collaborators (Forbes & Isenberg, 1991; Isenberg et al., 1993; Forbes & Priest, 1995; Lin & Forbes, 2000; Reeves & Forbes, 2005; Reeves et al., 2007). This work investigates the equilibrium states of a flux rope with finite cross-section in the presence of a number of background field configurations: a sunken dipole (Forbes & Isenberg, 1991) and quadrupole (Isenberg et al., 1993) as well as two magnetic point sources attached (Forbes & Priest, 1995) and detached (Lin & Forbes, 2000; Reeves & Forbes, 2005) current sheets. In each case, the loss of equilibrium is caused by photospheric motions on timescales similar to observations, while reconnection allows the rising flux rope to escape the corona in an eruption (Lin & Forbes, 2000). Figure 1-4 shows the evolution of the loss of equilibrium of the flux rope.

Lin & Forbes (2000) and Lin (2001) added reconnection to the framework developed in the Forbes & Priest (1995) loss of equilibrium model. Without reconnection, the loss of equilibrium causes the flux rope to jump to a new equilibrium point, higher in the corona, where it oscillates, but does not escape. With the addition of reconnection, it becomes possible to cut the field lines that effectively tether the flux rope in place and allow it to escape as a CME. Because it was based on the same framework as the Forbes and Priest model, the Lin and Forbes model is a two-dimensional model which evolves through a series of quasi-steady states as the CME progresses. This model did a good job of capturing the overall characteristics of an eruption, but it also had several limitations. First, it did not include the effects of gravity or the
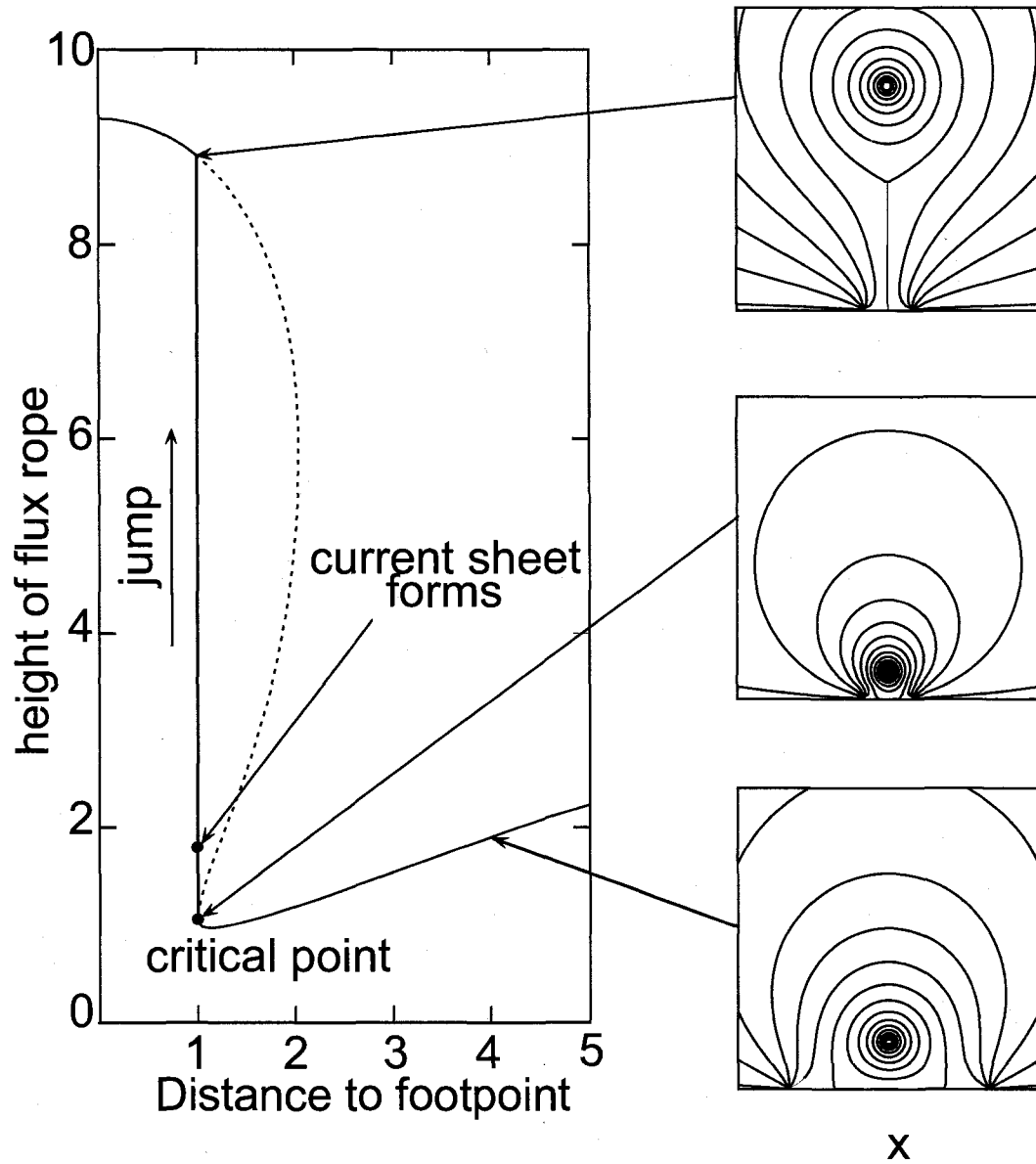
Figure 1-4: Evolution of the loss of equilibrium of a flux rope. (Figure from Forbes & Priest, 1995, used with permission.)

generation of MHD waves. Second, it made no predictions about the dynamics of the current sheet, which it treated as having zero thickness. In fact, Lin himself wrote about this in his Ph.D. dissertation: "...although we have already investigated the importance of magnetic reconnection to the eruptive phenomena, there is still much that remans to be determined. For example, what is the actual dynamics of the reconnection process in the current sheet during an eruption[?]" (Lin, 2001).

Reeves & Forbes (2005) and Reeves (2006) extended this model further in several important ways. First, they determined the radiative energetics of the model by including the thermal energy released in the current sheet. Second, they included the effects of gravity on the evolution of the eruption and energy release. Third, they present a detailed investigation of the relationship between flux rope acceleration and energy release. Finally, they use the thermal energy release to model light curves produced by various solar telescopes, including the spatial and spectral properties of the CME associated flare. Thus the Reeves and Forbes model provides a more complete picture of the unfolding eruption, including both the CME dynamics and predictions for the observed intensities of the evolving flare. They, too, however treat the current sheet as infinitely thin and make no predictions about its dynamics. This limitation served as one major motivation for the research discussed in the rest of this dissertation.

1.3 Theories of Magnetic Reconnection

As we mentioned above, all of the contemporary CME and flare models depend on magnetic reconnection in order to convert energy stored in the coronal fields into heat and kinetic energy. The term "magnetic reconnection" was coined by Dungey (1953) who had been studying particle acceleration in the Earth's magnetosphere. Several earlier studies (Giovanelli, 1946; Hoyle, 1949) had considered the question of

particle acceleration at magnetic neutral points, but did not include the magnetic field produced by the particle motions themselves. Dungey used an MHD framework to show that these moving particles would produce current in a thin sheet where the dynamics would be dominated by magnetic field diffusion—a feature we (perhaps unsurprisingly) now refer to as a current sheet. Dungey argued that diffusion of the field as it passed through this layer would cause a change in overall magnetic connectivity, a process he described as field line "disconnection" followed by "reconnection." Nearly simultaneously, Cowling (1953) also realized the importance of current sheets for plasma heating and particle acceleration during solar flares as well. Recent developments in reconnection theory have led to numerous models, both steady-state and time-dependent; one-, two-, and three-dimensional geometries; analytic and numerical (Priest & Forbes, 2000). This dissertation focuses on a two-dimensional, steady-state treatment of the reconnection problem. It should be noted, however, that during the impulsive phase of a flare the field evolves rapidly, and the quasi-steady approximation may not be a good one. On the other hand, during the gradual and late phase of the flare, when the current sheet evolves on long timescales, a quasi-steady approximation is not unreasonable.

1.3.1 The Sweet-Parker Reconnection Model

Dungey's 1953 reconnection model was a conceptual model rather than a mathematical one; it was only several years later that the first quantitative reconnection models appeared. Sweet (1958) and Parker (1957) presented the first such model, for the 2D, steady-state, incompressible case. They assumed that the reconnection would occur in a long, thin current layer whose length was set by the global scale-length of the field, L_e. A schematic of their model, now commonly referred to as the Sweet-Parker model, is shown in Figure 1-5. Sweet and Parker estimated that, under the conditions

shown in the figure, the speed at which plasma enters the current sheet is given, in MKS units, by

$$v_e = v_{Ae} L_u, \tag{1.1}$$

where $L_u = \mu_0 L_e v_{Ae}/\eta$ is the Lundquist number (sometimes also notated S, and called the magnetic Reynolds number), $v_{Ae} = B_e/\sqrt{\mu_0 \rho_e}$ is the Alfvén speed in the inflow region, η is the resistivity, B_e is the field strength in the inflow region, and ρ_e is the plasma density in the inflow region. The outflow speed in the Sweet-Parker framework is v_{Ae} and does not depend on the Lundquist number. In 2D models, the reconnection rate is given simply by the electric field perpendicular to the plane of the model at the reconnection site. Since the field is uniform in space in steady state models like the Sweet-Parker model, the Alfvén Mach number, $M_{Ae} = v_e/v_{Ae}$, gives the reconnection rate, normalized by the characteristic electric field $v_{Ae} B_e$. Thus the Sweet-Parker reconnection rate is simply given by

$$M_{Ae} = L_u^{-1/2}. \tag{1.2}$$

In astrophysical plasmas, like the corona, the Lundquist number is very large ($L_u \gg 10^6$) so the reconnection rate is very slow—far too slow to be the mechanism that drives events like solar flares, which happen on very short timescales.

1.3.2 The Petschek Reconnection Model

Petschek (1964) recognized this limitation of the Sweet-Parker model, and thus proposed a mechanism by which magnetic fields could reconnect at a much faster rate. He did this by significantly reducing the length of the diffusion region in the Sweet-Parker model. In Petschek's model there is a small central Sweet-Parker-like diffusion region attached to two pairs of standing slow-mode shocks which radiate outwards and consititute the bulk of the field reversal layer. Petschek's configuration appears in Figure 1-6. These shocks provide the majority of the conversion of the field from
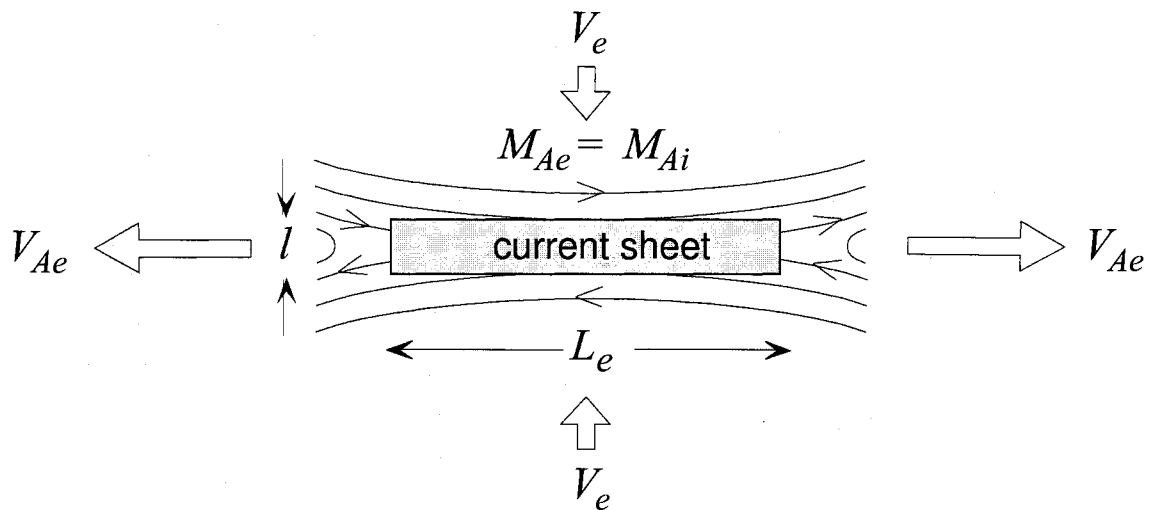
Figure 1-5: Field and flow configuration for the Sweet-Parker model. Plasma flows into the current sheet, length L_e, from above and below and exits through the narrow tips of the sheet, which have thickness l. The field is assumed to be uniform in the inflow region, so the external Alfvén Mach number, M_{Ae}, is equal to the internal Alfvén Mach number, M_{Ai}, which is measured at the midpoint of the edge of the current sheet. (Figure from Forbes, 2007, used with permission.)
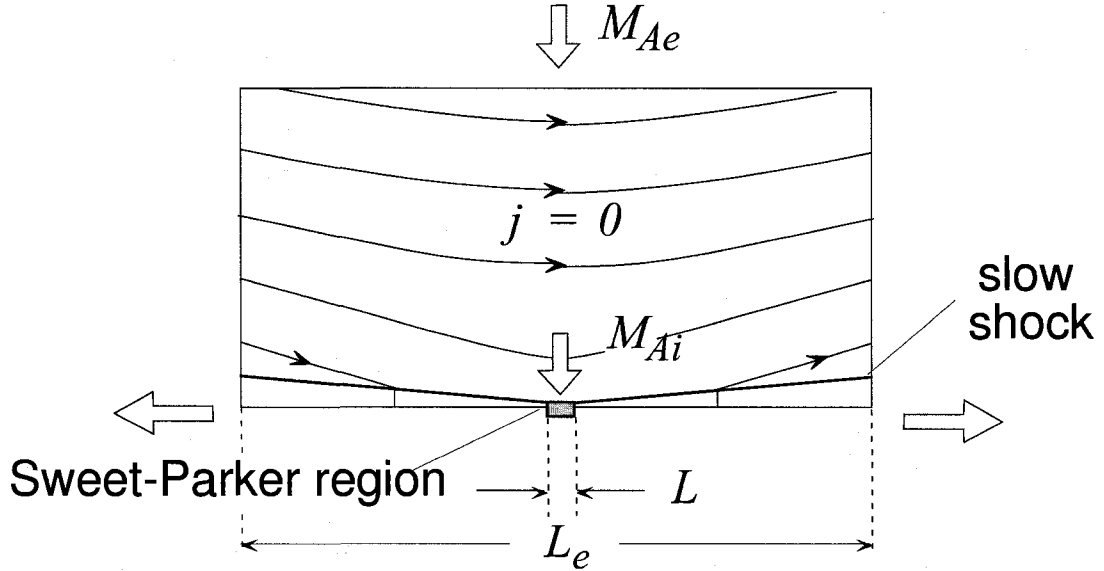
Figure 1-6: Field configuration for the Petschek model. The length, L, of the Sweet-Parker diffusion region is much shorter than the global scale length L_e and the entering field is not uniform as in the Sweet-Parker model. To pairs of slow-mode shocks extend out from the central diffusion region. (Figure from Forbes, 2007, used with permission.)

stored magnetic energy to heat and flow, and lead to the appearance of two hot outflow jets at the ends of the current layer.

In deriving his model, Petschek assumed that the inflow region was current-free and that there were no field sources at large distance. When combined with the trapezoidal shape of the inflow region caused by the presence of the slow shocks, these assumptions cause a logarithmic decrease in the magnetic field as the inflowing plasma approaches the diffusion region. The variation of the field leads to a new formula for the maximum reconnection rate:

$$M_{Ae(max)} = \pi/(8 \ln L_u), \tag{1.3}$$

where the Lunquist number, L_u, and Alfvén speed on which it depends are now
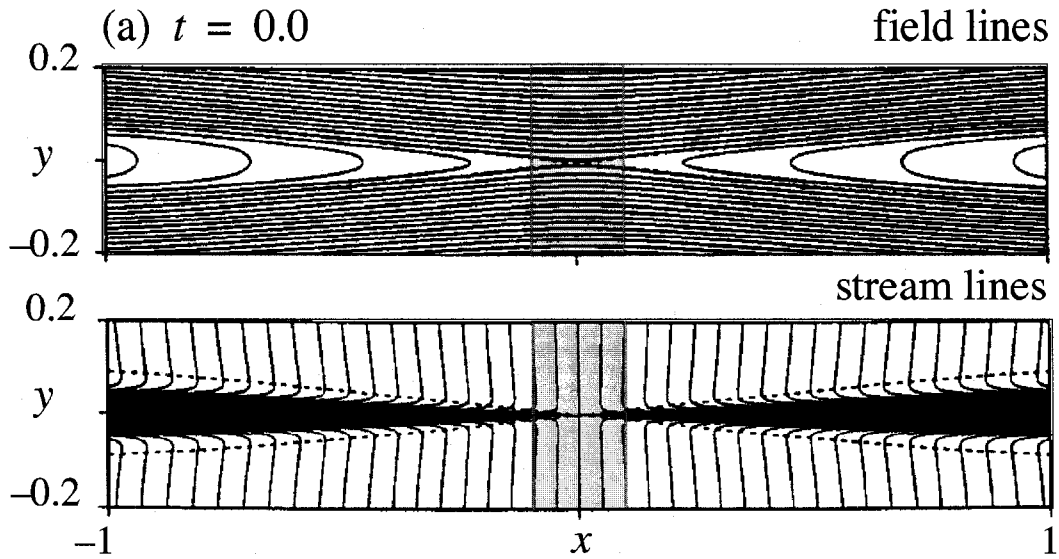
Figure 1-7: The configuration used by (Yan et al., 1992) to produce a Petschek-like solution. The red box indicates the location of the resistivity enhancement.

measured in the region far upstream of the current layer (see Figure 1-6). Because of the logarithmic dependence on the Lundquist number, the Petschek reconnection rate is much higher than the Sweet-Parker reconnection rate. For most plasmas, the Petschek formula predicts a reconnection rate, given by the Alfvén Mach number, of $M_{Ae} \approx 10^{-1}$ or 10^{-2}.

Since its introduction, the validity of the Petschek model has been a subject of much debate. Various numerical simulations carried out during the last 30 years show that it is a valid solution provided that there is some additional mechanism introduced to restrict the length of the central diffusion region. For example, the addition of a localized resistivity enhancement near the x-line, such as that seen in Figure 1-7 can force Petschek-like behavior (Yan et al., 1992; Baty et al., 2006). The use of more realistic kinetic treatments of the plasma in the current layer has also been shown to lead to Petschek type behavior (Wang et al., 2000).
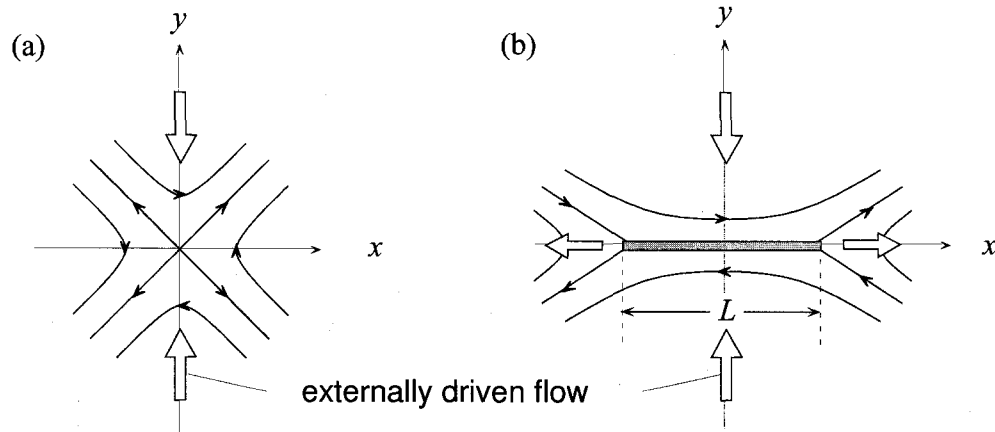
Figure 1-8: The Syrovatskii field configuration. Here, external sources produce an x-line even when local sources of current are not present. External driving then creates a current sheet, length L, whose length depends on the history of the driving and reconnection rate (Somov, 1992). The fastest reconnection occurs when L is equal to the global scale length, L_e. (Figure from Forbes, 2007, used with permission.)

1.3.3   The Syrovatskii Model

While both the Petschek and Sweet-Parker models relied on the same mechanism, Green (1965) and Syrovatskii (1971) approached the reconnection problem in another way. They studied what happened when a weak flow interacts with an X-type neutral point (or x-line) in a magnetized plasma. Figure 1-8 shows an illustration of this type of reconnection configuration. When the external flow matches the rate at which field lines diffuse through the current sheet there is a steady state. It is this model which provides the starting point for the Somov-Titov model, which is described in detail in Chapter 2, and forms the basis for our own analysis of the reconnection problem.

As we saw above for the Petschek model, in steady-state MHD models the variation of the field in the inflow region is the key quantity for dertermining how the reconnection rate will scale with the Lundquist number. In all such models the electric field will be uniform and perpendicular to the plane of the magnetic field. Outside

the diffusion region, the electric field can be expressed as $E_0 = -v_y B_x$, where E_0 is a constant, while v_y and B_x are the inflow and field along the axis of symmetry (this corresponds to the y axis in our picture of the Syrovatskii model). We can then write the inflow Alfvén Mach number far upstream as

$$M_{Ae} = M_{Ai} B_i^2 / B_e^2, \tag{1.4}$$

where M_{Ai} is the Alfvén Mach number in the current sheet, B_i is the magnetic field at the edge of the current sheet, and B_e is the magnetic field far upstream. In the Syrovatskii model the inflowing field along the y axis varies according to

$$B_x = B_i (1 + y^2 / L^2)^{1/2}, \tag{1.5}$$

where, again, B_i is the field at the current sheet and L is the length of the current sheet. We can combine equations 1.4 and 1.5 in order to find the variation of the reconnection rate as a function of the length of the current sheet. We find that

$$M_{Ae} = M_{Ai} / (1 + L_e^2 / L^2). \tag{1.6}$$

Thus the Syrovatskii reconnection rate is largest when $L = L_e$. In this case, the reconnection rate scales as $L_u^{-1/2}$, the same as the Sweet-Parker model.

1.3.4 Other Reconnection Models

Several other reconnection solutions, which are obtained by relaxing some of the assumptions made in the Petschek model, also exist. In particular, one can assume that the current density, j, in the inflow region is nonzero (Petschek assumed that $j = 0$ to first-order). In this case, the removal of the assumption allows an additional degree of freedom (the value of j) and thus creates a family of solutions. One way to characterize these solutions is by considering the relationship between internal Alfvén Mach number (M_{Ai}, measured at the entrance to the diffusion region) and external Alfvén Mach number (M_{Ae}, measured at the exterior inflow boundary).

24

In the flux pile-up solution the streamlines near the y axis diverge, and the field lines come closer together as they approach the diffusion region. Thus the field strength increases close to the diffusion region—this is the flux pile-up from which this type of reconnection takes its name. Because the divergence of the streamlines tends to expand the plasma, this type of flow is also referred to as a slow-mode expansion. In the flux pile-up case, the central diffusion region is much larger than in the Petschek case, but the reconnection is nonetheless fairly fast. Figure 1-9 shows an illustration of this type of solution.

The other solution in Figure 1-9 is similar in character to flux pile-up and is called stagnation-point-flow (Clark, 1964; Sonnerup & Priest, 1975; Litvinenko et al., 1996). In the case when the resistivity is low, a very thin current sheet is created (with a very large magnetic gradient and, therefore, a very large current density, j). As magnetic field enters this sheet, it is destroyed by cancellation with the field entering from below. Plasma, which is physical matter, cannot be cancelled, and so must flow out sideways (Parker, 1973; Sonnerup & Priest, 1975). While the flow entering away from the y axis tends to diverge, the flow along the axis must necessarily stop at the current sheet, thus a stagnation point—where there is no flow—forms at the origin in this solution. The streamlines in stagnation-point-flow solutions behave similarly to those in solutions for fluids flowing into a stationary obstacle; this type of hydrodynamic flow solution gives these MHD solutions their name.

The solutions above are only a few of the steady-state models that have been developed over the years. Many others also exist (e.g. Sonnerup, 1970; Yeh & Axford, 1970; Shivamoggi, 1985; Craig et al., 1995), but these are the ones most relevant to the discussion in subsequent chapters.
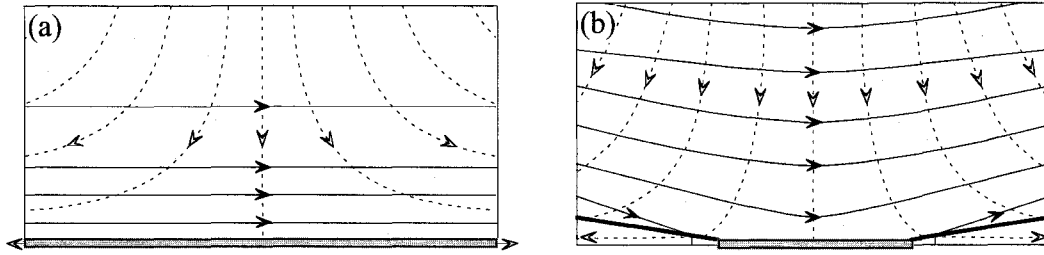
Figure 1-9: The stagnation-point flow solution (panel a) for field annhilation and the related flux pile-up solution (panel b). (Figure from Forbes, 2007, used with permission.)

1.4 New Research Presented in this Dissertation

This dissertation extends the reconnection model first discussed by Somov et al. (1987) in several important ways. First, this is the first time that an asymmetric version of the model has been developed. Such an asymmetric model is essential for analyzing the reconnection process in eruptive flares. We use this new asymmetric model to improve the Reeves & Forbes (2005) flare model in order to capture some of the dynamics of the current sheet. Second, we consider the effects of thermal conduction on the properties of the plasma in the reconnection outflow. This new analysis also includes, for the first time in an analytical model, a study of the effect of thermal conduction on the plasma surrounding the current layer. Third, we also carry out an in-depth analysis of the Somov-Titov model and discuss its strengths and weaknesses. Specifically, we explain why it is unable to determine the rate of reconnection. We compare results from each of these extended versions of the Somov-Titov model with observations and numerical models of similar current sheets.

Chapter 2 of this dissertation begins with a complete analysis of the Somov-Titov model, including all of the assumptions made in deriving the model and an exploration of the justification for these assumptions. After rederiving the Somov-Titov system we

present a discussion of the range of solutions allowed by this framework. We explore the relationship between the Somov-Titov model and the Sweet-Parker and Petschek models, and consider the implications of these results for those earlier reconnection models. In particular, we focus on the effects of several of the key assumptions of this model concerning the diffusion region. We also consider, for the first time, the effect that a non-uniform resistivity has on the model.

In chapter 3 of this dissertation we integrate the Somov-Titov model into the asymmetric field from the Reeves and Forbes model. This allows us to make several improvements to the assumptions Reeves and Forbes made about the dynamics of the current layer and the energy budget of their model. Incorporating these improvements into the Reeves and Forbes model, we re-examine one of the CME cases presented in Reeves & Forbes (2005) to see the effect of these improvements. The key question of what determines the rate of reconnection remains unanswered. We compare these improved predictions to similar predictions made by numerical models by Reeves et al. (2008a). We also consider the implications of an asymmetric background field on the Somov-Titov model itself, including such a field's effect on the family of solutions obtained in the simpler, Syrovatskii-like model employed originally by Somov and Titov.

Finally, in chapter 4, we consider the effects of thermal conduction on the Somov-Titov model. Using work on the structure of slow-mode shocks by Xu & Forbes (1992), we are able to extend the model to include the effects on and effects of the plasma surrounding the current layer. We compare these results to predictions that Yokoyama & Shibata (1997) and Yokoyama & Shibata (2001) made using numerical simulations of current sheets during flares, also including thermal conduction. Finally, we consider the role of thermal conduction on the generation and strength of fast-mode shocks in the reconnection outflow jet.

CHAPTER 2

AN ANALYSIS OF THE

SOMOV-TITOV SOLUTION FOR

2D STEADY-STATE

RECONNECTION

2.1 The Somov-Titov Approach to the Reconnection Problem

In this treatment of the steady-state 2D reconnection problem we use a technique by Somov & Titov first discussed in Somov (1992) and Somov et al. (1987). This approach returns the variation of averaged quantities along the length of the diffusion region including any associated slow-mode, Petschek-type shocks. The advantage of working with average quantities is that one can reduce the full set of 2D MHD equations to a set of 1D equations. The primary disadvantage is that information about the internal variations across the layer are lost.

Although not well known, this approach to the reconnection problem makes use of a common procedure for the analysis of fluid flow through a nozzle. Perhaps the best known example, found in many fluid dynamics textbooks, is the analysis of the de Laval nozzle. This is an hourglass shaped nozzle that is used to accelerate fluid flow

to supersonic speed (Leipmann & Roshko, 1957, pp. 124–130 and Schreier, 1982, pp. 46–57). This type of nozzle is used in all modern rocket engines and supersonic jet engines, so solutions to this problem are widely known. The de Laval nozzle works by forcing subsonic flow to pass through a narrow throat, which forces the flow to accelerate to supersonic speed. The problem is often simplified by averaging the flow over the width of the nozzle, reducing the problem from two-dimensional to one-dimensional. This approximation is valid as long as the width of the nozzle is small compared to the scale of the variation of the thickness along the nozzle to the length of the nozzle. The principal difference between this approach and the Somov-Titov approach, however, is that a nozzle has a definite profile, and thus there is a known function that describes the width of the nozzle as a function of the distance along it. In Somov & Titov's treatment of reconnection flow, the current layer's shape is not known—its thickness depends on how the other parameters act on it. Thus an additional assumption about the character of the reconnection layer must be imposed in order to obtain a solution for the 1D system. In fact, this aspect of the problem also has a counterpart in nozzle flow: once the flow from a nozzle exits into free space, it is bounded by shocks whose shape and location are not known. Nonetheless, the 1D treatment can still be used in this region to provide some useful results. (See pp. 127–130 of Leipmann & Roshko, 1957.)

In order to solve the reconnection problem, Somov begins with the complete set of steady-state 2D MHD equations. These equations, given by Roberts (1967), are the *continuity equation,*

$$\frac{\partial}{\partial x_i}(\rho V_i) = 0, \tag{2.1}$$

the *momentum equation,*

$$\rho\left(V_j \frac{\partial}{\partial x_j}\right)V_i = -\frac{\partial p}{\partial x_i} - \frac{\partial}{\partial x_j}M_{ij}, \tag{2.2}$$

where,

$$M_{ij} = \frac{1}{2} \left| \mathbf{B} \right|^2 \delta_{ij} - B_i B_j,$$

the *energy equation*,

$$\frac{\partial q_i}{\partial x_i} = 0, \tag{2.3}$$

where,

$$q_i = \left(\frac{\gamma}{\gamma - 1} p + \frac{\rho}{2} \mathbf{V}^2 \right) V_i + \frac{c}{4\pi} \left(\mathbf{E} \times \mathbf{B} \right)_i - \lambda \frac{\partial T}{\partial x_i},$$

and *Ohm's Law*,

$$\mathbf{j} = \sigma(x) \left(\mathbf{E} + \mathbf{V} \times \mathbf{B} \right). \tag{2.4}$$

Here, x_i are the planar cartesian coordinates, ρ is the density of plasma, $\mathbf{V}$ is a vector representing the velocity of flow, p is the gas pressure, M_{ij} is the Maxwell stress tensor (for a plasma), $\mathbf{B}$ is the magnetic field, λ is a conduction coefficient, T is the plasma temperature, c is the speed of light, $\mathbf{E}$ is the electric field, $\mathbf{j}$ is the electric current, γ is the ratio of specific heats (taken, throughout this paper, to be 5/3), and $\sigma(x)$ is the electrical conductivity.

2.2 Deriving the Averaged Equations

Before we apply the averaging approach used by Somov (1992), it is useful to introduce some of the notation and assumptions we will use below. Figure 2-1 shows a schematic of the field and flow configuration to be considered. First, we compute averages by integrating each term of the MHD equations over the half-thickness, $a(x)$, of a current layer centered along the x-axis, so that, for example,

$$\langle Q \rangle = \frac{1}{a(x)} \int_0^{a(x)} Q(x, y) dy, \tag{2.5}$$

where y is the direction normal to the layer and $\langle Q(x) \rangle$ is the average value of some function $Q(x, y)$. The location $y = a(x)$ corresponds to an external point, just ouside

30

of the layer. This point represents the division between the potential field region where there is no current density, and the non-potential current layer itself, where current density is not necessarily zero. That is, for locations where $y > a$ the magnetic field is potential, while for locations where $y < a$ there is some current density. This current density may be spread uniformly throughout the layer, as in the diffusion region, or may be bifurcated into shocks, as in the Petscheck shocks region. Note that in the diffusion region, the dynamics are dominated by plasma diffusion (the $\eta\mathbf{j}$ term) while in the shocks region, dynamics are dominated by the $\mathbf{V} \times \mathbf{B}$ term.

Because every quantity that remains after averaging is a function of x only, we will simplify our notation by dropping the (x) from here on. Subscripted variables such as V_{ya} will indicate boundary values at a. Subscripted variables such as V_{y0} indicate values at the center of the layer at $y = 0$. Finally, following the standard practice for nozzle flow, we assume that quantities defined inside the current layer are uniform across the layer, allowing us to rewrite averages of products as products of averages, so

$$\langle Q \cdot R \rangle \approx \langle Q \rangle \langle R \rangle.$$

Here Q and R represent two arbitrary variables which have been averaged using the procedure above.

In order to evaluate boundary terms in averaged equations, we need to know the properties of the plasma outside of the current layer. Most of these properties are the result of the inherent symmetry of the current sheet to be considered. Working with the configuration shown in Figure 2-1, we suppose the following properties hold:

- The current layer is much thinner than the scale of the variations in x along the layer,

- The field and flow configuration has the four-fold symmetry and anti-symmetry properties show in Figure 2-1,

- The dominant contribution to the magnetic field outside the current layer is B_x,

- The density in the current layer is nearly uniform across the layer, hence $\rho_0 = \langle \rho \rangle$,

- Terms of order two and higher in Alfvén Mach number, M_A, can be dropped.

The assumptions about the symmetry have particular consequences for several quantities along the axes. Because the magnetic field in the x-direction reverses as one crosses the x-axis, $B_{x0} = 0$. Similarly, because the incoming flow above the x-axis is in the the negative direction while incoming flow below the x-axis is in the positive direction, the flow in the y-direction must reverse sign at the x axis, thus $V_{y0} = 0$. We will make use of both of these facts when we derive the averaged MHD equations below.

This treatment involves the use of several parameters: the inflow Alfvén Mach number, M_A, the plasma beta, β, and the Lundquist number (or magnetic Reynold's number), L_u, and the normalized thermal conductivity coefficient, λ. We normalize each equation so that solutions depend only on these four input parameters. Table 2.1 shows how each physical quantity is normalized.

We note, as does Somov (1992), that the assumption that the thickness of the sheet is much less than its length and that it is relatively uniform in variation means that

$$\frac{a}{L} \ll 1; \frac{da}{dx} \ll 1.$$

Additionally, as we have pointed out above, variations across the current layer are assumed to be much smaller than variations along the layer. That is,

$$\frac{d}{dy} \ll \frac{d}{dx}.$$

Both of these will be important in deriving the equations that follow.
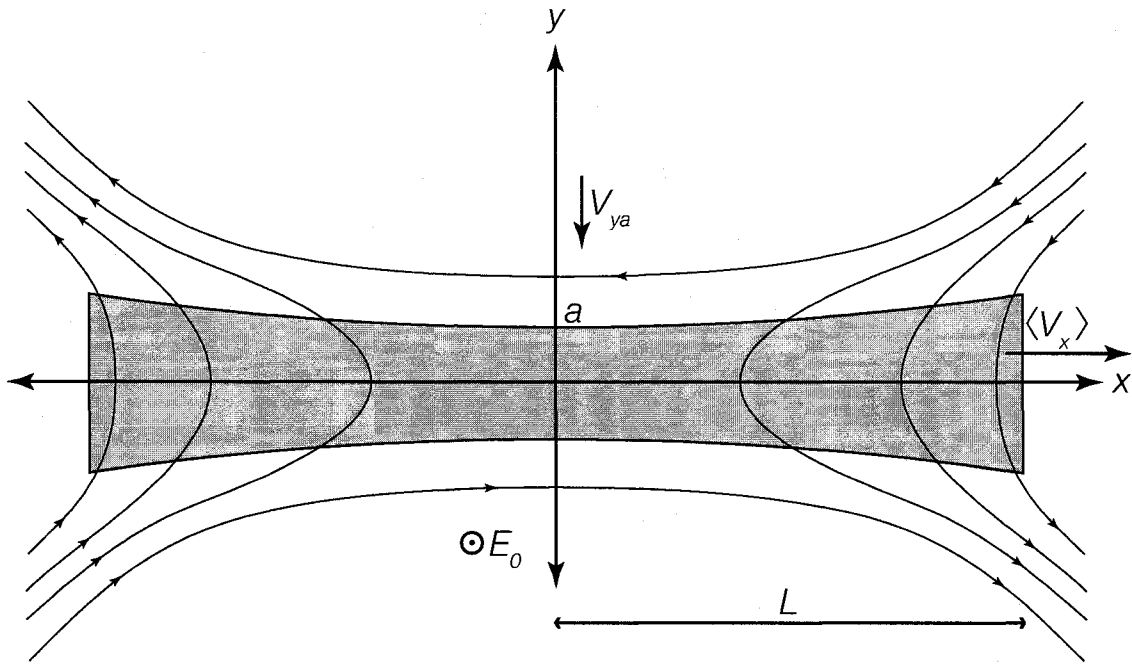
Figure 2-1: Schematic of the field and flow configuration used in the Somov-Titov approach. The shaded region, with thickness $a(x)$, represents the current layer. Field is carried into the current layer from the top and bottom, reconnects, and is ejected in two oppositely directed jets in the x-direction.

Quantity	Symbols	Normalization
Magnetic Field	B	B_0
Velocity	V	$B_0/\sqrt{4\pi\rho_0}$
Density	ρ	ρ_a
Pressure	p	$B_0^2/4\pi$
Length	x	L

Table 2.1: Normalization of physical quantities. B_a and ρ_a are the magnitude of **B** and the value of the density at $x = 0$, $y = a$. β is the ratio of gas to magnetic pressures at the same location, and L is the length of the current layer.

2.2.1 The Continuity Equation

We begin our derivation of the Somov-Titov equations by taking the average of the continuity equation (Equation 2.1). Integrating it across y leads to

$$- (\rho_a V_{ya} - \langle \rho \rangle V_{y0}) = \frac{\partial}{\partial x} \int_0^{a(x)} \rho V_x dy - \rho_a V_{xa} \frac{\partial a}{\partial x},$$

Here, we have integrated the left hand side of the equation directly and have applied Leibniz's Rule in order to move the derivative outside the integral on the right-hand side. Because $V_{y0} = 0$ by symmetry, we can eliminate the second term on the left. Then, deconvolving the integral in the first term on the right-hand side and noting that ρ_a is normalized to 1 everwhere (see Table 2.1), we obtain

$$-\rho_a V_{ya} = \frac{d}{dx} \left(a \langle \rho \rangle \langle V_x \rangle \right) - \rho_a V_{xa} \frac{da}{dx}. \tag{2.6}$$

2.2.2 The Momentum Equation

Before taking the average of the momentum equation (Equation 2.2), we divide it into x- and y-components. In normalized units, we now have,

$$\rho \left(V_x \frac{\partial}{\partial x} + V_y \frac{\partial}{\partial y} \right) V_x = -\frac{\partial}{\partial x} p + \frac{\partial}{\partial y} B_x B_y - \frac{\partial}{\partial x} \left(\frac{\mathbf{B}^2}{2} - B_x^2 \right), \tag{2.7}$$

and

$$\rho \left(V_x \frac{\partial}{\partial x} + V_y \frac{\partial}{\partial y} \right) V_y = -\frac{\partial}{\partial y} p + \frac{\partial}{\partial x} B_x B_y - \frac{\partial}{\partial y} \left(\frac{\mathbf{B}^2}{2} - B_y^2 \right). \tag{2.8}$$

Averaging over the x-component of the momentum equation gives us

$$\int_0^a \rho \left(V_x \frac{\partial}{\partial x} V_x \right) dy + [\rho V_y V_x]_0^a - \int_0^a \left(V_x \frac{\partial}{\partial y} \rho V_y \right) dy =$$

$$= - \left[\frac{\partial}{\partial x} \int_0^{a(x)} \left(p + \frac{B_x^2}{2} \right) dy - \left(p_a \frac{\partial a}{\partial x} + \frac{B_{xa}^2}{2} \frac{\partial a}{\partial x} \right) \right]$$

$$+ \int_0^{a(x)} \left(\frac{\partial}{\partial x} B_x^2 + \frac{\partial}{\partial y} B_y B_x - \frac{1}{2} \frac{\partial}{\partial x} B_y^2 \right) dy,$$

where we have used integration by parts on the left-hand side of the equation, and Leibniz's Rule on the bracketed term on the right-hand side. On the left-hand side,

34

we can immediately simplify the bracketed term, because we know that $V_{y0} = 0$ by symmetry. We can apply Equation 2.1 again and rewrite the left-hand side of the equation

$$LHS = \rho_a V_{ya} V_{xa} + \int_0^a \rho \left(V_x \frac{\partial}{\partial x} V_x \right) dy + \int_0^a \left(V_x \frac{\partial}{\partial x} \rho V_x \right) dy =$$

$$= \rho_a V_{ya} V_{xa} + \int_0^a \left(\frac{\partial}{\partial x} \rho V_x^2 \right) dy = \rho_a V_{ya} V_{xa} + \frac{d}{dx} \left(a\rho \langle V_x \rangle^2 \right) - \frac{da}{dx} \rho_a V_{xa}^2,$$

where we have used Leibniz's Rule to complete the intergral.

To evaluate the right-hand side, we will make use of the y-component of the momentum equation, which, after averaging, can be straightforwardly written

$$\langle p \rangle = p_a + \frac{B_{xa}^2}{2} - \frac{\langle B_x^2 \rangle}{2}. \tag{2.9}$$

Since the kinetic energy density of the inflowing plasma is of second order, the total pressure (gas plus magnetic) must be balanced in the y-direction everywhere. Therefore, $p_0 = \langle p \rangle$. By averaging Gauss's Law for magnetic fields, and assuming that B_y is essentially uniform in the current sheet (so, similarly to pressure, $B_{y0} = \langle B_y \rangle$) we find a relationship between B_{ya} and the other quantities in the momentum equation,

$$B_{ya} = < B_y > + B_{xa} \frac{da}{dx} - \frac{d}{dx} \left(a \langle B_x \rangle \right). \tag{2.10}$$

Carrying out the integration on the right-hand side and applying Leibniz's Rule one more time, the right-hand-side becomes

$$RHS = - \left\{ \frac{d}{dx} \left[a \left(\langle p \rangle + \frac{\langle B_x \rangle^2}{2} \right) \right] dy - \left(p_a \frac{da}{dx} + \frac{B_{xa}^2}{2} \frac{da}{dx} \right) \right\}$$

$$+ B_{ya} B_{xa} + \left[\frac{d}{dx} \left(a \langle B_x \rangle^2 \right) - \frac{da}{dx} B_{xa}^2 \right] - \left[\frac{d}{dx} \left(a \langle B_y \rangle^2 \right) - \frac{da}{dx} B_{ya}^2 \right].$$

Following standard practice (Priest & Forbes, 2000) we observe that the inflow Alfvén Mach number, M_A, is small and that terms that are of second order in M_A can be dropped. Since $\langle B_y \rangle$ and B_{ya} are proportional to M_A, the squared terms $\langle B_y \rangle^2$

35

and B_{ya}^2 are of second order and are therefore eliminated. We can then expand the first term and apply Equation 2.9 to eliminate the second term in the curly brackets. We use Equation 2.10 to expand the term $B_{ya}B_{xa}$, and find that several terms cancel. We can then find the final form of the momentum equation,

$$\frac{d}{dx}\left(a\rho\langle V_x\rangle^2\right) + \rho_a V_{xa}\left(V_{ya} - \frac{da}{dx}V_{xa}\right) =$$
$$= -a\frac{d\langle p\rangle}{dx} + \langle B_y\rangle B_{xa} + a\frac{d}{dx}\left(\frac{\langle B_x\rangle^2}{2}\right) + \langle B_x\rangle^2\frac{da}{dx} - B_{xa}\frac{d}{dx}\left(a\langle B_x\rangle\right).$$

2.2.3 The Energy Equation

Somov & Titov originally treated the case of reconnection using a relatively simple energy equation. More recently Oreshina & Somov (1998) and Somov & Oreshina (2000) have considered the effect of radiative losses and thermal conduction. Here we follow the original treatment of Somov & Titov. We will reconsider these equations, including the effect of thermal conduction, in Chapter 4.

Integrating both sides of Equation 2.3 above yields

$$\int_0^a \frac{\partial}{\partial x}\left[\left(\frac{\gamma}{\gamma-1}p + \frac{\rho}{2}\mathbf{V}^2\right)V_x - E\,B_y\right]dy =$$
$$-\int_0^a \frac{\partial}{\partial y}\left[\left(\frac{\gamma}{\gamma-1}p + \frac{\rho}{2}\mathbf{V}^2\right)V_y + E\,B_x\right]dy.$$

Here, E is the electric field, which is constant everywhere and normalized to $V_{A0}B_0/c$. The integration on the right-hand side can be carried out directly. Noting that V_{y0} and B_{x0} must be zero by symmetry, and that V_{ya}^3 is a third-order term that can be neglected, the right side becomes

$$RHS = -\left(\frac{\gamma}{\gamma-1}p_a + \frac{\rho_a\left(V_{xa}^2\right)}{2}\right)V_{ya} - E\,B_{xa}.$$

As before, we use Leibniz's Rule on the left-hand side, and rewrite the averaged Equation

$$LHS = \frac{d}{dx}\left\{\left[\left(\frac{\gamma}{\gamma-1}\langle p\rangle + \frac{\langle\rho\rangle}{2}\langle\mathbf{V}\rangle^2\right)\langle V_x\rangle - c\,E\,\langle B_y\rangle\right]a\right\}$$

$$-\frac{da}{dx}\left[\left(\frac{\gamma}{\gamma-1}p_a + \frac{\rho_a}{2}\mathbf{V}_a^2\right)V_{xa} - cEB_{ya}\right].$$

Terms containing $\langle V_y \rangle^2$ and V_{ya}^2 are second-order terms that we can drop (since $\langle V_y \rangle$ and V_{ya} are proportional to M_A these squared terms are again of second order). At the boundary of the current layer, in our normalized units, the electric field can be written $E = V_{ya}B_{xa} = M_A$ (since $B_{xa} = 1$ where $x = 0$ and $V_{ya} = M_A$ at this point) so the final form of the energy equation becomes,

$$\frac{d}{dx}\left[\left(\frac{\gamma}{\gamma-1}\langle p \rangle + \frac{\langle \rho \rangle}{2}\langle V_x \rangle^2\right)\langle V_x \rangle a\right]$$
$$-\frac{da}{dx}\left[\left(\frac{\gamma}{\gamma-1}p_a + \frac{\rho_a}{2}V_{xa}^2\right)V_{xa}\right] = -\left(\frac{\gamma}{\gamma-1}p_a + \frac{\rho_a\left(V_{xa}^2\right)}{2}\right)V_{ya} - M_A B_{xa}.$$

$$(2.11)$$

2.2.4 Ohm's Law

Finally, we can rearrange and expand Ohm's Law and average it,

$$\int_0^a \left(\frac{1}{\sigma}\right)\left(\frac{\partial}{\partial x}B_y - \frac{\partial}{\partial y}B_x\right)dy = \int_0^a \left[E + (V_xB_y - V_yB_x)\right]dy.$$

Note that the term containing that B_y is of higher order than any of the other terms, and is therefore dropped. Also note that, because the electric field is uniform in the 2D steady-state flow, integrating the first term on the right hand side simply yields aE. We can then integrate the entire equation directly, to find

$$-\frac{1}{\sigma}B_{xa} = a\left[E + (\langle V_x \rangle \langle B_y \rangle - \langle V_y \rangle \langle B_x \rangle)\right].$$

Although neither $\langle B_x \rangle$ nor $\langle V_y \rangle$ in the second term on the right are necessarily zero in general, this term is negligible for the type of reconnection flows considered by Somov & Titov. In the diffusion region $\langle V_y \rangle$ is negligible by definition since a is defined here as the location in y where the diffusive electric field dominates. Outside the diffusion region, $\langle B_x \rangle$ is negligible. Thus we neglect this term entirely. Finally,

using that $E = M_A$ again and that $L_u = c^2/\sigma$ we can find the final form of Ohm's Law,

$$a = \frac{-B_{xa}}{L_u \left(M_A + \langle V_x \rangle \langle B_y \rangle \right)}.$$ (2.12)

2.3   The Somov-Titov System

The assumptions made so far are fairly general ones that concern the geometry of the current layer and the ordering of quantities involved. In deriving their solutions, however, Somov & Titov have made several additional assumptions that restrict the set of possible solutions to those that resemble the Sweet-Parker and Petschek-like configurations. Other types of reconnection solutions, such as stagnation-point-flow (Sonnerup & Priest, 1975) and flux-pile-up (Priest & Forbes, 2000, pp. 152–153), are eliminated by these additional assumptions. The additional assumptions that Somov & Titov make that restrict the set of solutions that are obtained are:

- There is no significant tangential flow outside the current layer, thus $V_{xa} = 0$.

- The background magnetic field corresponds to the Syrovatskii solution to the current sheet problem, that is, $B_{xa} = -\sqrt{1 - x^2}$.

- There is no tangential magnetic field inside the current layer, thus $\langle B_x \rangle = 0$.

The first assumption eliminates stagnation-point-flow type solutions because these solutions have a significant tangential flow in the x-direction outside the current layer. This assumption, however, is very appropriate for the Petschek-like solutions where the exterior tangential flow is of second order in the Alfvén Mach number (Priest & Forbes, 1986).

The second assumption, that the fields involved are Syrovatskii-like, is one that has been recently used by several authors (Uzdensky & Kulsrud, 2000; Malyshkin

38

et al., 2005). It represents an improvement over the assumption made by Petschek that the external field is uniform. The Syrovatskii expression naturally incorporates the length of the current sheet (or current layer, if shocks are present) determined by the external field sources. By contrast, the uniform field does not include this length in a natural way, but presupposes that the uniform field is simply terminated at some external length-scale (corresponding to $x = 1$ in our dimensionless units.) This termination is formally accomplished by putting the Petschek solution in a box whose dimensions are arbitrary and are not coupled to the external field.

In the limit that $\langle B_y \rangle \to 0$, the Somov-Titov solution reverts to that of Syrovatskii. Thus to first order, this formula, which describes the tangential field near a neutral sheet formed close to the zero-line, is a good choice. It is possible to improve this model by applying a formalism described in Chapter 3.4 of Somov (1992) that allows for the external Syrovatskii field to be improved by an iteration process that uses the solution for $\langle B_y \rangle$ to obtain a new B_{xa}. (This process will be discussed in detail in the final chapter of this thesis.)

The third assumption, that there is no tangential field inside the current layer, is motivated by the fact that in the shock region of the Petschek model, the reconnected field is entirely perpendicular. Thus Somov & Titov presuppose a similar geometry. The validity of this assumption must be considered carefully for two reasons. First, even for the Petschek model there is a substantial component of tangential field in the small diffusion region. At the x-line $|\langle B_x \rangle| \approx 1/2\, M_A$, so $|\langle B_x \rangle| = 0$ seems a somewhat dubious assumption in this region. Second, the very need to assume something about the behavior of $\langle B_x \rangle$ underscores an important point about the Somov-Titov model, which is that the lack of a prescription for $a(x)$ causes a problem. Without an equation for $a(x)$, the averaging method leaves us without a closed set of equations. While the other assumptions Somov & Titov make about the system apply to *external* variables,

this assumption applies to an *internal* variable. Normally we would solve a problem like this by making assumptions about the background values—the model input—and using these assumptions to solve for the internal variables. Somov & Titov eliminate one of the internal variables (i.e. $\langle B_x \rangle$) in order to close the system of equations they obtain. Further, even with this assumption they do not fully fix the solution because, as we will see, their solution still contains the reconnection rate as a free parameter. (In fact, this is also the case for Petschek's solution, which similarly fails to determine a unique reconnection rate.) Because this is an especially important point, we will discuss it more completely in Section 2.4.

Using the assumptions detailed above, Somov & Titov arrive at their averaged MHD equations: the continuity equation,

$$-V_{ya} = \frac{d}{dx}\left(a\langle\rho\rangle\,\langle V_x\rangle\right),$$
(2.13)

the momentum equation,

$$\frac{d}{dx}\left(a\rho\langle V_x\rangle^2\right) = -a\frac{d\,\langle p\rangle}{dx} + \langle B_y\rangle\,B_{xa},$$
(2.14)

the energy equation,

$$\frac{d}{dx}\left[\left(\frac{\gamma}{\gamma-1}\,\langle p\rangle + \frac{\langle\rho\rangle}{2}\,\langle V_x\rangle^2\right)\langle V_x\rangle\,a\right] = -\frac{\gamma}{\gamma-1}p_a V_{ya} - M_a\,B_{xa},$$
(2.15)

and Ohm's Law,

$$a = \frac{-B_{xa}}{L_u\left(M_A + \langle V_x\rangle\,\langle B_y\rangle\right)}.$$
(2.16)

Note that in order to solve these equations we also make use of the pressure balance equation, which comes from Equation 2.9 and in normalized units becomes

$$\langle p\rangle = \frac{\beta}{2} + \frac{B_{xa}^2}{2}.$$
(2.17)

We solve this system with the computer application *Mathematica 6.0.1* using the default method in the "NDSolve" routine. "NDSolve" finds numerical solutions to

40

analytic systems of differential equations. The Appendix shows the complete *Math-ematica* code used to solve this system, including the effects of thermal conduction, which are discussed in Chapter 4.

2.3.1 Solutions to the Somov-Titov System

The Somov-Titov equations produce a family of solutions that depend on the choice of input parameters, M_A, β, and L_u. As for the Sweet-Parker model, the length of diffusion region, α, is related to the sheet thickness by

$$\alpha = \frac{a_0}{M_A},\tag{2.18}$$

where a_0 is simply $a(0)$. Since $a_0 = 1/L_u M_A$, we also have

$$\alpha = \frac{1}{L_u M_A^2}.\tag{2.19}$$

The parameter α can be as small as $\alpha = a_0$ and as large as $\alpha = 1$. Figure 2-2 shows examples of each of these solutions. The four variables plotted are $\langle V_x \rangle$, $\langle B_y \rangle$, $\langle \rho \rangle$, and a. In the case of the small α solutions (solid curve) $\langle V_x \rangle$ and $\langle B_y \rangle$ characteristically rise to nearly their maximum outflow values quickly inside the diffusion region, then remain relatively constant through the shock region, much like the Petschek solution. The thickness of the current layer, a, also increases in a manner expected for the slow-shocks present in the Petschek model. The solutions' tendency away from Petschek-like behavior as they approach the end of the current layer is due to the decrease in B_{xa} of the Syrovatskii background field. This effect is absent from Petschek's solution because of its use of a uniform background field (i.e. $B_{xa} = -1$).

In the case of a Sweet-Parker-like solution where $\alpha \approx 1$ (dashed line), $\langle V_x \rangle$ and $\langle B_y \rangle$ do not achieve their maximum outflow values until they reach the end of the current layer, which, in this case, is also the end of the diffusion region. When α is slightly greater than 1, $\langle B_y \rangle$ increases as x^3. (In Figure 2-2 we have chosen L_u
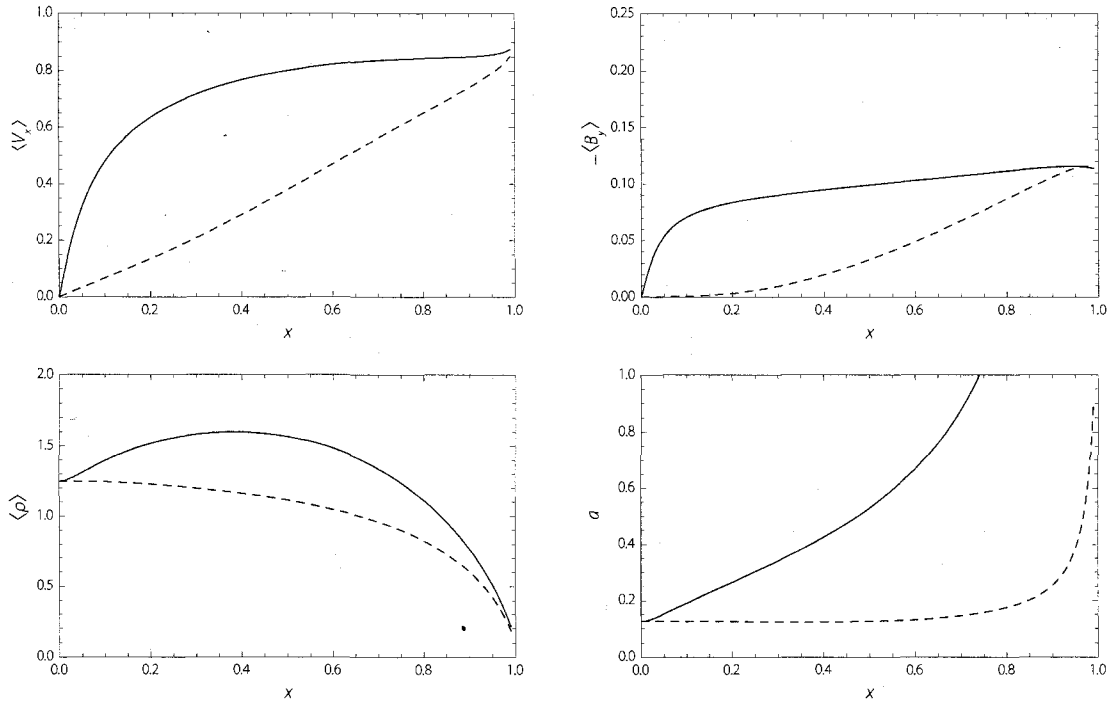
Figure 2-2: Two possible solutions to the Somov-Titov system for an inflow Alfvén Mach number $M_A = 0.1$. The solid line is a Petschek-like solution, with $L_u = 1000$, and thus $\alpha = 0.1$, while the dashed line is a Sweet-Parker-like solution with $L_u \approx 80$ and $\alpha \approx 1.25$.

so that $\langle B_y \rangle$ behaves in this way.) This choice of α produces the most sheet-like solution, and we refer to the value of α that produces it as the *critical* α. We discuss the implications of the fact that the Somov-Titov system, like Petschek's, does not predict a unique reconnection rate, as one would expect for a physical parameter in the next section.

2.3.2 Relation to the Petschek and Sweet-Parker Solutions

As we have discussed above, Somov & Titov have approached the reconnection problem by assuming *a priori* that the field reversal layer—that is, the current layer plus shocks—have a Petschek-like character. Two of the assumptions they make—that

flow enters the layer entirely perpendicularly to it ($V_{xa} = 0$) and that the tangential field inside the layer is negligible ($\langle B_x \rangle = 0$)—presuppose this type of behavior. The first assumption rules out alternate types of reconnection that are associated with external driving such as stagnation-point flow (Sonnerup & Priest, 1975) and flux-pile-up (Priest & Forbes, 1986). The second assumption is only plausible for Petschek-type solutions with shocks that are close to the switch-off limit. As we discussed before, this is especially problematic in the diffusion region, where $\langle B_x \rangle$ is never zero.

Somov & Titov's approach does not lead to a unique answer for the reconnection rate, but instead, they recover a family of solutions with M_A ranging from $L_u^{-1/2}$ to 1. The former corresponds to the Sweet-Parker value, where the diffusion region runs the full length of the current sheet. The latter corresponds to a diffusion region whose length, $\alpha = 1/Lu = a_0$—that is, a diffusion region whose length is approximately the same as its thickness. This behavior parallels that of Petschek's solution, which also produces a family of solutions for Alfvén Mach numbers over the same range. In Petschek's solution, the reconnection rate is usually expressed in terms of the external Alfvén Mach number, M_{Ae}, which is measured at a large distance upstream of the current layer. Thus the correspondence between the Somov-Titov and Petschek models is not immediately apparent. The maximum Petschek reconnection rate is expressed as $M_{Ae} = (4/\pi)/\ln(L_u)$. This value occurs when the length of the diffusion region is approximately the same as its thickness and when the Alfvén Mach number at the entrance to the diffusion region is close to or equal to unity (See Priest & Forbes, 1986).

The similarity between the Somov-Titov solution and Petschek's solution is even more striking when we replace $B_{xa} = -\sqrt{1 - x^2}$ with $B_{xa} = -1$, so that the external magnetic field is uniform instead of decreasing with distance as it does in the Sy-

rovatskii case. Then the most important difference between the two models is the use of the assumption $\langle B_x \rangle = 0$ in the Somov-Titov formalism. Instead of this assumption, Petschek uses the condition that outside of the diffusion region the position of the current reversal layer, a, is determined by the speed at which the slow-mode wave propagates. Thus, in order to obtain a steady-state solution, the outward propagating wave must balance exactly with the inflow velocity upstream of the shocks. In the incompressible limit, one can derive the simple equation:

$$\frac{da}{dx} = \frac{V_\perp(x)}{V_{A\perp}(x)}, \tag{2.20}$$

where $V_{A\perp}$ is the Alfvén speed based on the component of the magnetic field normal to the shock. If we attempt to solve this equation by integration, we find it is necessary to supply a constant of integration, which Petcheck sets by assuming the slow shocks are attached to the end of the diffusion region, such that $a(\alpha) = a_0$. Petschek makes no prescription for the value of α, however, except that it must lie between the sheet thickness ($\alpha = 1/L_u$) and the global scale length ($\alpha = 1$).

The similarity between the Somov-Titov and Petschek solutions has some bearing on the question of whether Petschek reconnection can take place in a plasma with uniform electrical resistivity. Numerical simulations suggest that Petschek's solution only occurs if the diffusivity is localized near the x-line. Some simulations have explicitly localized the diffusivity in this way by imposing a fixed spatial distribution on the resistivity (Yan et al., 1992; Baty et al., 2006), while others do it implicitly by relating the resistivity to some other variable like current density, which is naturally enhanced near the x-line (Ugai, 1988; Bhattacharjee & Wang, 1991). Some have argued that Petschek assumed that the resistivity of the current layer is uniform (e.g. Biskamp, 2000, pp. 387), and therefore his solution is inconsistent. However, Petschek's solution does not actually specify what the resistivity does at all, it only assumes that the length of the diffusion region can be shorter than the global length

scale. (As we noted, there is no equation that determines what this length should be.) As a result, Petschek's solution makes no prediction about the specific reconnection rate, it only provides a family of solutions with a range of possible reconnection rates.

In the Somov-Titov framework, the indeterminacy is a consequence of the lack of an independent equation for the location of the boundary a. If such an equation existed, it would apply to both diffusion and shock regions, and would have to include the physics that creates the slow shocks. The length of the diffusion region remains a free parameter, while the only inherent length scales in the model are the global length and the thickness of the current sheet at the origin. In the case they consider, with uniform resistivity, it is difficult to see what causes the genesis of the slow shocks without the introduction of an additional length scale. This scale length could come from an imposed nonuniform resistivity (we will consider this case in Section 2.3.3) or perhaps the ion-inertial scale length associated with Hall resistivity.

Somov & Titov's work suggests, then, that the problem with Petschek's solution is not that it is inconsistent, but rather, it is incomplete. The apparent inconsistency arises from the interpretation that all reconnection rates allowed by Petschek's solution are equally valid. Previously, some authors (Forbes & Priest, 1987) have argued that the correct reconnection rate for Petschek-like solutions should be set by the boundary condition at large distance, specifically the flow provided by the external driving. However, this line of argument is inconsistent with the fact that characteristic rays in the upstream region of Petschek's solution require that there is no external driving (Soward & Priest, 1977). Thus it may very well be that the only valid Petschek solution for the case of uniform resistivity is the one where the length of the diffusion region is the same as the global length scale—that is, $\alpha = 1$ in our terms, or the Sweet-Parker solution. In order to obtain faster reconnection rates, it seems that some physical mechanism must be present to trigger the formation of

Petschek's slow shocks. In the next section, we show analytically that imposing a nonuniform resistivity, is sufficient to force a Petschek-like solution.

2.3.3 Effects of Nonuniform Resistivity

In order to understand the effects of nonuniform resistivity on the Somov-Titov solution, we introduce a conductivity, σ, in Section 2.2.4 that varies with the distance x. Following Yan et al. (1992) and Baty et al. (2006) we assume a prescribed profile of the form

$$\sigma(x)^{-1} = \frac{1}{L_u} \left[1 + q \, \exp(-x/x_s)^2 \right], \tag{2.21}$$

where q is the degree of nonuniformity and x_s is the scale length over which σ varies. To match the numerical simulations of Yan et al. (1992) and Baty et al. (2006) x_s is set equal to α. We compare the results from this case to a case with uniform resistivity that has the same value of σ outside of the diffusion region. Figure 2-3 shows a plot of normal magnetic field, $\langle B_y \rangle$, as calculated in each case. The red curve is the case with nonuniform resistivity, while the blue curve has uniform resistivity. Adding nonuniform resistivity alters the profile of the field inside the diffusion region by a small amount, while outside the diffusion region the solutions quickly become indistinguishable. This is because only a small percentage of magnetic flux enters the current sheet through the diffusion region, while the majority of flux enters through the shocks. Thus the shocks completely dominate the dynamics of the current layer. Thus the effect of nonuniform resistivity is primarily seen in the properties of the diffusion region.

The two curves shown in Figure 2-3 both correspond to the same small α, low β case. Here $M_A = 0.1$, $\beta = 0.03$, and $L_u = 3600$, so $\alpha = 0.03$. Therefore, even the case with uniform resistivity already exhibits the short diffusion region behavior characteristic of Petschek-like solutions. The nonuniformity only serves to enhance
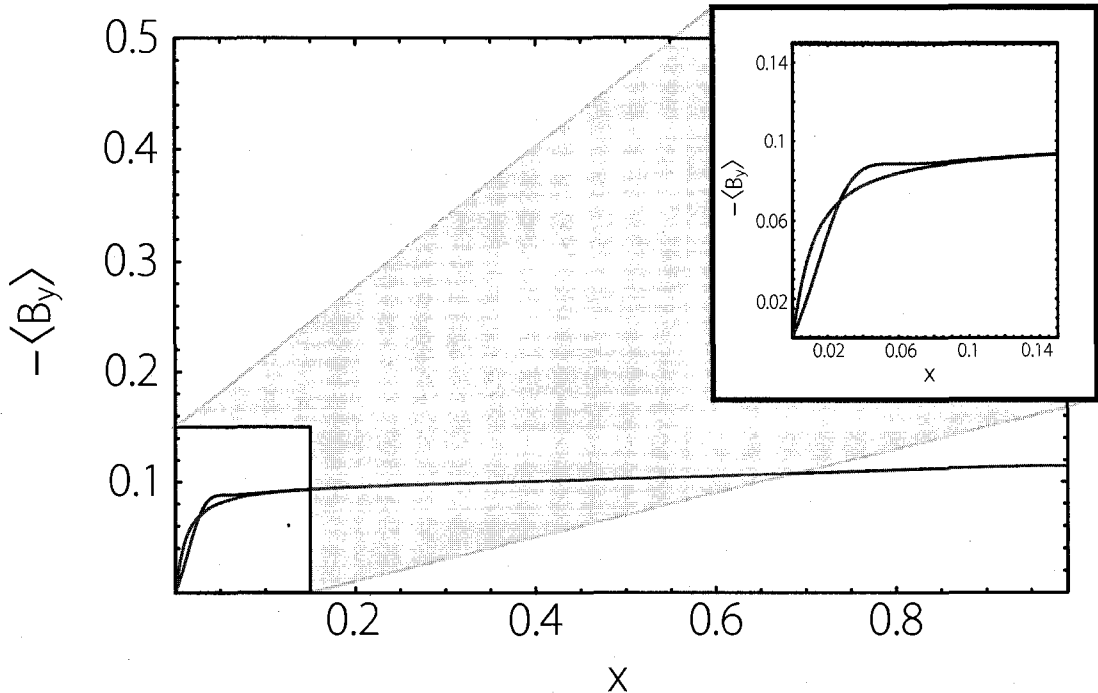
Figure 2-3: A comparison of solutions with non-uniform (red curve) and uniform (blue curve) resistivity. Outside the diffusion, where the slow-mode shocks dominate the plasma dynamics, the solutions are exactly the same. Here $M_A = 0.1$, $\beta = 0.03$, and $\alpha = 0.03$.

the boundary between diffusion and shocks regions, creating a more kinked curve, which corresponds to a sharper division between the two different regimes—the rising field (with respect to x) seen in the diffusion region and the relatively constant (also with respect to x) field seen in the shocks region. However, the external behavior of $\langle B_y \rangle$ and $\langle V_x \rangle$ is unaffected by the changes within the diffusion region.

As we pointed out above, numerical solutions have shown that nonuniformity is required to generate the shocks that allow the Petschek solutions to occur. Here, however, the Petschek-like behavior is built-in to the solution through the assumptions that $\langle B_x \rangle = 0$ and that the free parameter α is significantly less than unity. Once these assumptions are made, a Petschek-like solution is guaranteed. The formal addition

of nonuniform resistivity (i.e. $L_u(x)$) leads to an improved solution for the diffusion region. However, the physics needed to specify a unique reconnection rate are still missing. Thus we can say that including nonuniform resistivity in the Somov-Titov system has only a small effect on the diffusion region, while leaving the shocks region unaffected. The question of how the nonuniform resistivity leads to Petschek-type configurations remains unaddressed.

2.4   Expansion of the Solution within the Diffusion Region

Although Somov & Titov's assumption that there is no tangential field inside the current layer is reasonable between the slow shocks in the Petschek-like case, it is problematic in the diffusion region, especially in the vicinity of the x-line. In fact, an x-line cannot exist at $x = 0$ unless the average field tangential field is nonzero. As we discussed earlier, the assumption that $\langle B_x \rangle = 0$ allows Somov & Titov to close their system of equations and thereby determine the thickness of the current layer. Although it is not obvious how to obtain a more realistic equation for $\langle B_x \rangle$, we can investigate the general effect of the presence of a non-zero tangential field by considering a Taylor expansion of the Somov-Titov system for small distances from the x-line.

In order to examine this question in more detail we consider the situation at $x = 0$, which is the one place where it is possible to get a reasonable estimate of what $\langle B_x \rangle$ should be, and, therefore, its effect on the other variables. Somov & Titov (in Somov, 1992) provide expansions for the major variables at this point in the case that $\langle B_x \rangle = 0$, and we can use these expansions as the basis for our analysis of what the effect of the tangential field is. Here we repeat these expansions, assuming instead that $\langle B_x \rangle \neq 0$. We use the equations described in 2.2, but will continue to assume $V_{xa} = 0$. Then we expand the equations around $x = 0$, and compare to the Somov &

Titov results. They obtained the following expressions (in normalized units):

$$\langle V_x \rangle = \frac{4 + 5\beta}{5(1 + \beta)\alpha} x + O(x^3),$$ (2.22)

$$\langle B_y \rangle = -M_A \left[\frac{2(4 + 5\beta)}{5(1 + \beta)\alpha} - \alpha \right] x + O(x^3),$$ (2.23)

$$a = a_0 \left[1 + \frac{4(2 + 2.5\beta)^2 - 2.5\alpha^2(1 + \beta)(6.5 + 7.5\beta)}{12.5\alpha^2(1 + \beta)^2} x^2 + O(x^4) \right].$$ (2.24)

Note that the Somov-Titov expansion for a contains a series of typos when it appears in both Somov (1992) and Somov et al. (1987) which we have corrected above. Using these results, we can add the additional expansion,

$$\langle \rho \rangle = \frac{5(1 + \beta)}{4 + 5\beta} + O(x^2).$$ (2.25)

To generalize these expressions for the case where $\langle B_x \rangle \neq 0$, we must first determine the behavior of $\langle B_x \rangle$ at $x = 0$. By definition, at the entrance to the current layer at a, $B_x(0, a) = -1$ (consistent with Syrovatskii's expression). We also know that, by symmetry, at the x axis $B_x(0, 0) = 0$. If we assume that the current density is relatively uniform throughout the current layer, then B_x should vary relatively linearly across the current layer, and therefore $\langle B_x \rangle \approx -1/2$ at $x = 0$.

However, knowing the value of $\langle B_x \rangle$ at $x = 0$ is insufficient to determine the coefficients to first order in the expansion. The second derivative of $\langle B_x \rangle$ is required as well. (Because $\langle B_x \rangle$ is an even function, the first derivative of $\langle B_x \rangle$ is zero.) We know that the tangential field is nonzero inside of the diffusion region and should fall off to around zero at the end of the diffusion region at $x = \alpha$. Therefore, we suppose that

$$\langle B_x \rangle = -\frac{1}{2} + \frac{1}{2}\frac{x^2}{\alpha^2},$$

Corresponding to $\langle B_x \rangle'' \approx 1/\alpha^2$. With this expression we then can find, for $\langle B_x \rangle \neq 0$:

$$\langle V_x \rangle = \frac{4(4 + 5\beta)}{5(3 + 4\beta)\alpha} x + O(x^3),$$ (2.26)

49

$$\langle B_y \rangle = -M_A \left[\frac{158 + 200\beta}{(28 + 40\beta)\alpha} - \frac{75 + 100\beta}{28 + 40\beta}\alpha \right] x + O(x^3), \tag{2.27}$$

$$\langle \rho \rangle = \frac{5(3 + 4\beta)}{4(4 + 5\beta)} + O(x^2), \tag{2.28}$$

and

$$a = a_0 \left[1 + \frac{4(4 + 5\beta)(79 + 100\beta) - 5\alpha^2(3 + 4\beta)(47 + 60\beta)}{10\alpha^2(3 + 4\beta)(7 + 10\beta)} x^2 + O(x^4) \right] \tag{2.29}$$

Interestingly, the addition of tangential magnetic field does not affect the overall form of the expansions with respect to α—that is, $\langle V_x \rangle$ is still proportional to x/α and $< B_y >$ is still proportional to $(c_1/\alpha + c_2\alpha)\,x$, where c_1 and c_2 are coefficients that depend on β. This suggests that the Somov-Titov solutions are fairly robust with regard to the assumption concerning the effect of the behavior of $\langle B_y \rangle$ in the diffusion region as long as the scale over which $\langle B_x \rangle$ varies corresponds to α. The effect of allowing $\langle B_x \rangle \neq 0$ is to decrease the derivative of $\langle V_x \rangle$, and to increase the derivative of $\langle B_y \rangle$, and to decrease the value of $\langle \rho \rangle$. At the x-line, the thickness of the current layer is $a_0 = 1/(L_u M_A)$, regardless of the presence of tangential field (see Equation 2.12). The presence of $\langle B_x \rangle$ does, however, contribute to the overall pressure balance, helping support the current sheet against the exterior pressure. Less plasma compression is therefore needed to support a given sheet thickness, thus the density decreases in the presence of this additional field. This has the effect of reducing the density in the diffusion region from a value slightly greater than the external density ($\langle \rho \rangle > 1$) to a value slightly less than the external density ($\langle \rho \rangle < 1$).

The additional tangential magnetic field inside the diffusion region means that less of the exterior field is annihilated as it enters the current sheet. Consequently, less energy is available to accelerate the flow, resulting in an overall reduction of $\langle V_x \rangle$. As the flow leaves the diffusion region and the tangential field falls off, $\nabla \cdot \mathbf{B} = 0$ requires the normal field, $\langle B_y \rangle$, to increase at a higher rate than when the tangential field is left out.

In the case of a Petschek-like solution, all of these effects are small, since the bulk of the material enters the current layer through the shocks, rather than the diffusion region. For Petschek-like solutions, the shock dynamics dominate the diffusive dynamics, and the effect of the presence of $\langle B_x \rangle$ is likely only a few percent near the diffusion region, and is negligible outside of the diffusion region. In the Sweet-Parker-like case, however, the diffusion region is approximately the same length as the entire current sheet. In this case, we would conclude that the Somov-Titov result is more likely to contain error due to the assumption that there is no tangential field. However, because of the similarities in the expansions in either case, it is likely that the overall error remains less than a factor of two.

One other issue concerning $\langle B_x \rangle$ that should be considered is how accurate the assumption that $\langle B_x \rangle = 0$ is even in the shock region. Vasyliunas (1975) noted that when there is a gradient in the external tangential field along the current layer and shocks, the field lines between the shocks will be curved outwards. This curvature is a direct consequence of the velocity gradient across the current layer—the fact that the central portion of the reconnection jet moves faster than the edges. Field lines that enter the current layer inside the diffusion region are carried into the fast moving center of the reconnection jet, while field lines that enter in the shocks region remain in the slower moving outside of the reconnection jet. This velocity gradient has the effect of bowing the field lines outward. Our concern about $\langle B_x \rangle$ so far has been that field lines inside of the current layer will be curved inwards—bending towards the x-line—rather than the outward bend described by Vasyliunas. We supposed that in the shocks region, field lines would be essentially perpendicular to the outflow, and that the assumption that $\langle B_x \rangle = 0$ would not be in doubt in this region. This additional result suggests that this assumption may be suspect even in this other region. (And, in fact, some very crude experimentation using our own model, with

a prescribed shape for a and allowing the presence of some $\langle B_x \rangle$ suggested that this outward bowing of the field lines was likely to be real.) Nonetheless, this curvature is a second order effect in the shocks region, and thus $\langle B_x \rangle$ can be taken to be zero without introducing significant error into the solution.

In addition to considering the effect of $\langle B_x \rangle$ on expansions of the solution inside the diffusion region, we can also consider the effect of nonuniform-resistivity on the same region. For simplicity, we will consider only the incompressible (high β), $\langle B_x \rangle = 0$ case here. Because we wish to explore the effects of nonuniform resistivity, we adopt a simple nonuniform resistivity model, which has the effect of converting the Lundquist number from a constant into a function. The resulting Lundquist can be expanded such that,

$$L_u(x) = L_{u0} + L_{u2}x^2 + O(x^4), \tag{2.30}$$

where is defined as

$$L_{u2} \equiv \left. \frac{\partial^2 L_u}{\partial x^2} \right|_{x=0}.$$

In this case, Somov & Titov's expansions for the diffusion region become:

$$\langle V_x \rangle = \frac{1}{\alpha}x + O(x^3), \tag{2.31}$$

$$\langle B_y \rangle = -M_A \left[\frac{2}{\alpha} - \alpha \right] x + O(x^3), \tag{2.32}$$

$$a = a_0 \left[1 + \left(\frac{2}{\alpha^2} - \frac{3}{2} - \frac{L_{u2}}{L_{u0}} \right) x^2 + O(x^4) \right]. \tag{2.33}$$

In this case, we omit the expansion for $\langle \rho \rangle$ above because in the incompressible case, density is uniform everywhere. We also note that a_0 must be redefined slightly to $a_0 \equiv 1/L_{u0}M_A$, since the Lundquist number is now a function of x. We can estimate the value of the ratio L_{u2}/L_{u0} in the expansion for a by noting that

$$\frac{L_{u2}}{L_{u0}} = \left. \frac{\partial^2 L_u}{\partial x^2} \right|_{x=0} \frac{1}{L_{u0}} \approx \frac{1}{L_\eta^2},$$

where L_η is the scale length of the variation in $L_u(x)$.

In order to get some insight on the effect of the resistivity on the type of reconnection taking place, we consider the behavior of the current sheet under different reconnection conditions. One reasonable assumption we can make is that, regardless of the type of reconnection taking place, the current layer must have a thickness greater than zero—that is, $a(x) > 0$ for all x—otherwise, the current sheet is closed off to outflow, and reconnection cannot proceed. Because these expansions are valid only in the diffusion region, and because α represents the scale-length of the diffusion region, we can use these assumptions to conclude that, at the very least, $a(\alpha) > 0$. (Because $a(0)$ is, by definition, larger than zero, this condition is sufficient to ensure that the thickness of the current layer is greater than zero everywhere in the diffusion region.)

Inserting the expansion formula for $a(x)$, we conclude that for reconnection to take place, we must have

$$\frac{L_\eta}{\alpha} > \sqrt{\frac{2}{3\left(2 - \alpha^2\right)}}. \tag{2.34}$$

This means that if the ratio of the scale-length of the variation in resistivity to the length of the diffusion region is less than what is specified above, reconnection cannot occur. In the case where $\alpha = \sqrt{2}$, the critical α in the incompressible case, this ratio becomes infinity, thus it is impossible to recover the critical case in the presence of nonuniform resistivity. For small values of L_η, α will always be a small number. So nonuniform resistivity that varies over a short length-scale will requires that the diffusion region be small in order for reconnection to occur. Thus we conclude that the presence of nonuniform resistivity is sufficient to force a Petschek-like solution. This conclusion agrees with the finding of Yan et al. (1992), who found that it is the variation of resistivity over the length of the current sheet that determines whether reconnection is fundamentally Petschek or Sweet-Parker-like.

CHAPTER 3

THE ASYMMETRIC CURRENT

LAYER

In the previous chapter, we discussed the Somov-Titov method for modeling the field and flows in a reconnecting current sheet. Previous studies by Somov et al. (1987), Somov (1992), and Oreshina & Somov (1997, 1998) have applied this method only to symmetric configurations with a background field like the one used by Syrovatskii (1971). Here we apply this method to the asymmetric background field that develops during an eruptive solar flare using the field model of Lin & Forbes (2000) and Reeves & Forbes (2005). Like Syrovatskii's model, their model treats the current sheet as an infinitely thin layer and does not provide any information about the magnetic field and flows within the layer.

We discussed the Lin & Forbes model in Chapter 1 of this thesis. Because this model serves as the basis for our asymmetric solution to this problem, we will briefly review its basic properties before continuing with our discussion. The overall magnetic field configuration of the model depends, first, on four principle length scales: h, the height of the flux rope over the solar surface; q, the location of the upper tip of the current sheet; p, the location of the lower tip of the current sheet; and λ, the half-distance between the coronal loop footpoints. Figure 3-1 shows a schematic of the magnetic configuration of this model.

The model uses rectangular geometry, with the y axis aligned along the axis of
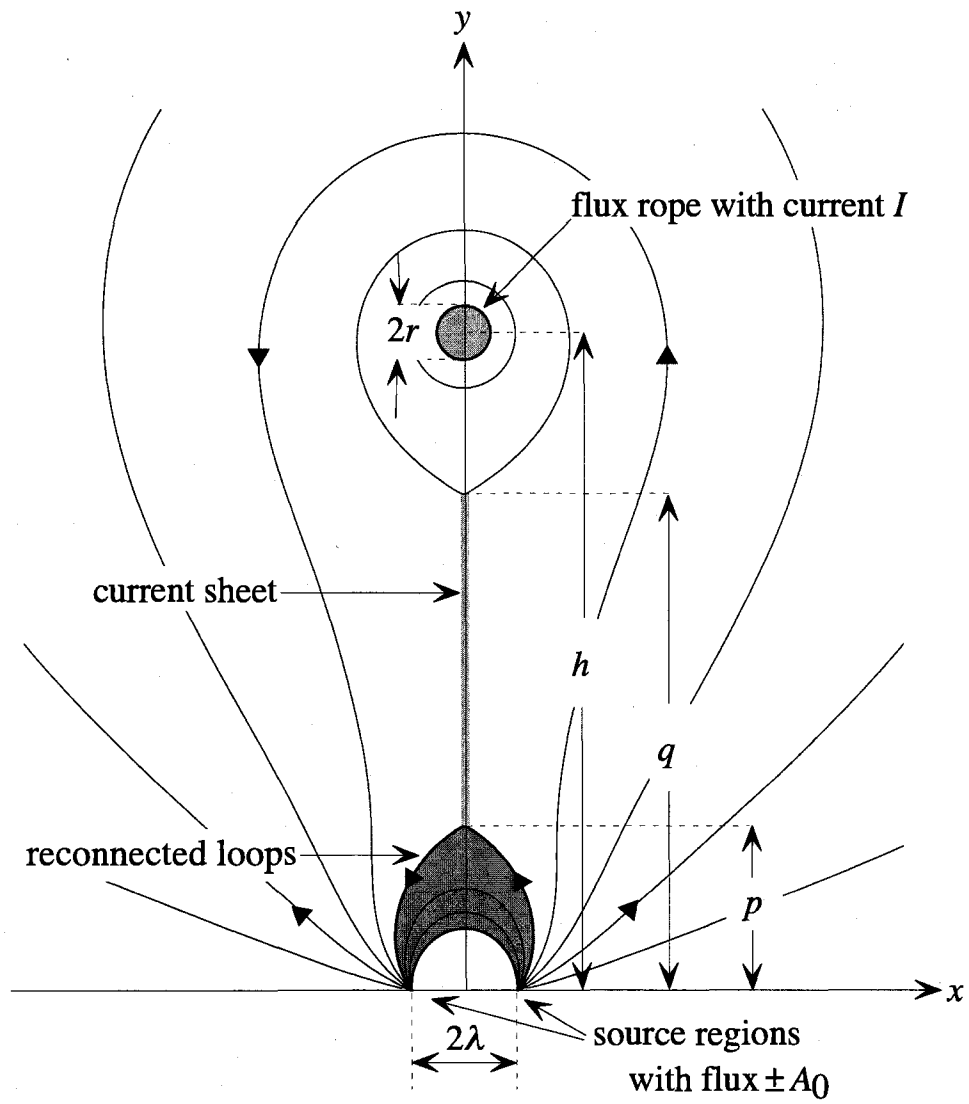
Figure 3-1: Magnetic configuration of the CME model of Lin & Forbes and Reeves & Forbes. (Figure from Reeves & Forbes, 2005, used with permission.)

symmetry of the model and $y = 0$ defined as coincident with the solar surface. Thus h, q, and p lie along the y axis, while λ sits on the x-axis, offset from the center line. The field is then given, in complex notation, by

$$B_y + iB_x = \frac{2iA_0\lambda\left(h^2 + \lambda^2\right)\sqrt{\left(\zeta^2 + p^2\right)\left(\zeta^2 + q^2\right)}}{\pi\left(\zeta^2 - \lambda^2\right)\left(\zeta^2 + h^2\right)\sqrt{\left(\lambda^2 + p^2\right)\left(\lambda^2 + q^2\right)}} \tag{3.1}$$

where A_0 is the source field strength and $\zeta = x + iy$. The current in the flux rope, I, is

$$I = \frac{c\lambda A_0}{2\pi h}\frac{\sqrt{\left(h^2 - p^2\right)\left(h^2 - q^2\right)}}{\sqrt{\left(\lambda^2 + p^2\right)\left(\lambda^2 + q^2\right)}}. \tag{3.2}$$

Another key parameter of the model is the location of the x-line, y_0. Because the Lin & Forbes model treats the current sheet as an infinitely thin layer, it makes no prediction about its behavior. It also does not predict the position of the x-line within the current layer, and consequently does not provide a good method for determining how much of the incoming Poynting flux into the layer is divided into the upward and downward jets. The flare model by Reeves & Forbes (2005), which is based on the Lin & Forbes CME model, made the *ad hoc* assumption that the x-line is located exactly in the middle of the current sheet—that is, at the point

$$y_0 = \frac{p + q}{2}. \tag{3.3}$$

This assumption, as we will see later in this section, only holds when the current sheet is very short and very symmetric, which, in this model, only occurs at the beginning of an event. During the bulk of the event, this approach overestimates the height of the x-line considerably.

Because the Somov-Titov model provides a prediction for the variation of flows and fields within the current sheet, we can obtain a more physically based estimate of the location of the x-line. As we will see, the relocation of the x-line will lead to a significant change in the energy output predicted by the Reeves & Forbes model for a given reconnection rate.

3.1 Locating the X-Line in an Asymmetric Current Sheet

In a symmetric current layer, the location of the x-line is necessarily at the midpoint of the layer, but in the asymmetric case, this is no longer true. In order to identify its location, we return to the unaveraged x-component of the momentum equation (Equation 2.7),

$$\rho \left(V_x \frac{\partial}{\partial x} + V_y \frac{\partial}{\partial y} \right) V_x = -\frac{\partial}{\partial x}p + \frac{\partial}{\partial y}B_x B_y - \frac{\partial}{\partial x}\left(\frac{\mathbf{B}^2}{2} - B_x^2 \right).$$

We consider this equation along the x-axis. Here, $V_y(y = 0) = 0$ and $B_x(y = 0) = 0$ by symmetry. Thus the equation becomes

$$\rho V_x \frac{\partial}{\partial x}V_x = -\frac{\partial}{\partial x}p + B_y \frac{\partial}{\partial y}B_x - \frac{\partial}{\partial x}\frac{B_y^2}{2}.$$

We can then assume that we are located at the x-line itself. Since this is a magnetic neutral point, both of the terms that include B_y must be zero and can be eliminated. Because the total pressure is in balance in the y direction to good approximation, we can write

$$p(y = 0) = p_a + \frac{B_{xa}^2}{2}.$$

In this treatment p_a is a constant and so its derivative is zero. Substituting the remaining term into the equation gives us a final result

$$\rho V_x \frac{\partial}{\partial x}V_x = -B_{xa}\frac{\partial B_{xa}}{\partial x}. \tag{3.4}$$

In the case where the stagnation point, the point at which the flow speed, and thus V_x goes to zero, and the x-line are co-located, then we find that the x-line will occur where

$$\frac{\partial B_{xa}}{\partial x} = 0, \tag{3.5}$$

which occurs where the external magnetic field reaches a maximum. However, even if the stagnation point and x-point are not co-located, as long as there is no acceleration

of flow through the x-line, this result still holds. In our quasi-steady treatment, any flow that does occur at the x-line must necessarily be diffusive and, therefore, small. Thus, the x-line will tend to be located close to the point where the magnitude of the external magnetic field reaches a maximum. We refer to this point as the *pinch point*. We note that because this result follows from the unaveraged momentum equation, it is completely independent of the assumptions made by Somov & Titov about the behavior of the plasma inside the current layer.

In many CME models, the external field around the current sheet becomes very uniform high in the corona, near the upper tip of the current sheet. Thus the possibility exists that small variations in the flow, caused by waves or turbulence, for example, may introduce additional x-lines and trigger the formation of magnetic islands. If this occurs, then the external field tangential to the current layer will be modified so that there is more than one pinch point. However, to the extent that the flow in the sheet is quasi-steady, the x-line should be located close to the pinch point.

There are also cases where we might expect acceleration of flow through the x-line to occur. One example would be early in an eruption, when the background field changes from symmetric to asymmetric, and the x-line moves rapidly from a point at the center of the current layer to a point near the lower tip of the layer. However, this case, and others in astrophysical and space plasmas, are highly time-dependent, and thus, our quasi-steady treatment of the problem does not apply. Nonetheless, there is considerable evidence that suggests that this property will hold in general for CMEs and flares. Numerical models of asymmetric current sheets (Linker et al., 2003; Reeves et al., 2008a) indicate that the x-line does indeed occur at (or very close to) this pinch point. EIT observations of CMEs also support this conclusion (Yokoyama et al., 2001).

3.2 Improving the Reeves & Forbes CME Model

Reeves & Forbes (2005) assumed that the Poynting flux entering the sheet is equally divided between the upward and downward directed jets. However, the partitioning of the Poynting flux is not equal in general, and it is very unequal when the x-line is not located near the middle of the current sheet, which is the case when the current layer becomes highly asymmetric.

In order to recalculate the trajectories of the flux rope, current sheet, and x-line, in the Reeves & Forbes model, we begin with their background magnetic field, which plays the same role in this calculation as the Syrovatskii field played in the last chapter. In Reeves & Forbes, the field along the current sheet is entirely in the tangential (now y, in our new coordinate system) direction, and is given by

$$B_{ya} = -\frac{2\lambda A_0 \left(\lambda^2 + h^2\right) \sqrt{\left(y^2 - p^2\right)\left(q^2 - y^2\right)}}{\pi \left(h^2 - y^2\right)\left(\lambda^2 + y^2\right)\sqrt{\left(\lambda^2 + p^2\right)\left(\lambda^2 + q^2\right)}}. \tag{3.6}$$

Finding the pinch point requires only that we find the point at which the B_{ya} is maximized, which we can find by solving the equation $dB_{ya}/dy = 0$ for y. Substituting Equation 3.6 into this expression, we obtain an equation for the location of the x-line

$$
\begin{aligned}
2\lambda A_0 y &\left(\lambda^2 + h^2\right) \left\{ 2y^6 + q^2 y^2 \left(\lambda^2 - 3y^2\right) \right. \\
&+ p^2 \left[y^2 \lambda^2 - 3y^4 + q^2 \left(4y^2 - 2\lambda^2\right) \right] \\
&\left. + h^2 \left[q^2 \left(y^2 + \lambda^2\right) + p^2 \left(-2q^2 + y^2 + \lambda^2\right) - 2y^2\lambda^2 \right] \right\} = 0.
\end{aligned}
\tag{3.7}
$$

Excluding the trivial solution $y = 0$, this is a cubic equation for y^2, so solving this equation gives 6 roots. These roots can be obtained explicity using the exact solution for cubic equations or numerically using a root finder. Only one of these roots will be both real and positive; this is the root that gives the location of the x-line in the current sheet.

There are two limiting cases of interest. In the limit where the current sheet is very short, p and q are close together and there is no significant variation of the short

length of the current layer. Thus the formula for the x-line location becomes

$$y_0 \approx \frac{p+q}{2}, \quad \text{for} \quad (q-p) \ll \lambda, \tag{3.8}$$

which is the relation assumed by Reeves & Forbes. In this limit, the field in Equation 3.6 is well approximated by the Syrovatskii described in section 2.3. This limit occurs early in an eruption, when the current sheet (or layer) first appears.

The other limit of interest occurs late in an event, when h and q are both large compared to p and λ. In this case, the formula for the x-line location becomes

$$y_0 \approx \sqrt{\lambda^2 + 2p^2}, \quad \text{for} \quad h \,\&\, q \gg \lambda \,\&\, p \tag{3.9}$$

Thus, in the limit where the current sheet becomes very long and the flux rope is at a high altitude in the corona, the x-line remains low in the corona, close to the bottom tip of the current sheet. This result implies that the quasi-steady position of the x-line in a reconnecting current sheet is much lower in the corona than the midpoint of the current sheet. In fact, it should be low enough in the corona throughout the duration of an eruption that several solar-imaging instruments, such as the X-Ray Telescope and EUV Imaging Spectrometer on board *Hinode*, may be able to detect it when an eruptive event occurs on the limb. Both of these instruments have relatively restricted fields of view that only cover a region of about 1 solar radius beyond the solar limb (Deluca, 2007). Thus, in contrast to the predictions of the Reeves & Forbes model that the x-line would spend most of its lifetime well outside of the fields of view of these instruments, we predict that the x-line should remain contained in the field of view for most of the lifetime of the event.

3.2.1 Recalculating Trajectories

Before we can examine the dynamics of the current layer itself, we must first understand the evolution of the background magnetic field during the eruption. In order

to do this, we revisit the calculation of the trajectories of the erupting flux rope and current sheet first reported by Lin & Forbes (2000) and Reeves & Forbes (2005). Because their calculation relies on the assumption that the x-line lies at the midpoint of the current sheet (see Equation 3.3), their calculation of the trajectories overestimates the height of the x-line throughout most of the eruption. Because the unnormalized reconnection rate (as measured by the electric field at the x-line) depends on the location of the x-line, a change in the location of the x-line will cause a change in the dynamics of the entire system. It is the unnormalized reconnection rate, $E\left(0, y_{x-line}\right)$ that determines the rate at which the magnetic flux is actually reconnected. So even if the normalized rate, $M_A = E\left(0, y_{x-line}\right)/V_{A0}B_{x0}$, remains the same, the actual rate will change when the x-line is relocated to a new position. Therefore, in order to see how the new location of the x-line effects the trajectories, we need to recalculate them from scratch. Thus we repeat the calculation outlined in section 2.3 of Reeves & Forbes (2005), following equations 19 through 26, but using the correct location of the x-line, which we determined in section 3.1.

For the purposes of this dissertation, we compare our new calculation to a specific case from Reeves & Forbes, where the background field, $B = A_0/(\pi\lambda_0)$, is 120 G. This treatment assumes the following parameters: the Alfvén Mach number at the x-line is $M_A = 0.025$, the photospheric footpoint separation is $\lambda_0 = 2 \times 10^9\,\mathrm{cm}$, the mass of the flux rope is $m = 2.1 \times 10^{16}\,\mathrm{g}$, the length of the flux rope is $L = 10^{10}\,\mathrm{cm}$, and the proton density at the base of the corona is $\rho = 1.67 \times 10^{-16}\,\mathrm{g}$. Using these values, we calculated trajectories assuming first that $y_0 = (p + q)/2$, the old Reeves & Forbes assumption, and then assuming that y_0 is located at the pinch point. The resulting trajectories are shown in Figure 3-2.

Figure 3-2A shows a plot of trajectories of h, q, y_0, and p, calculated using the Reeves & Forbes assumption that the x-line is located in the middle of the current
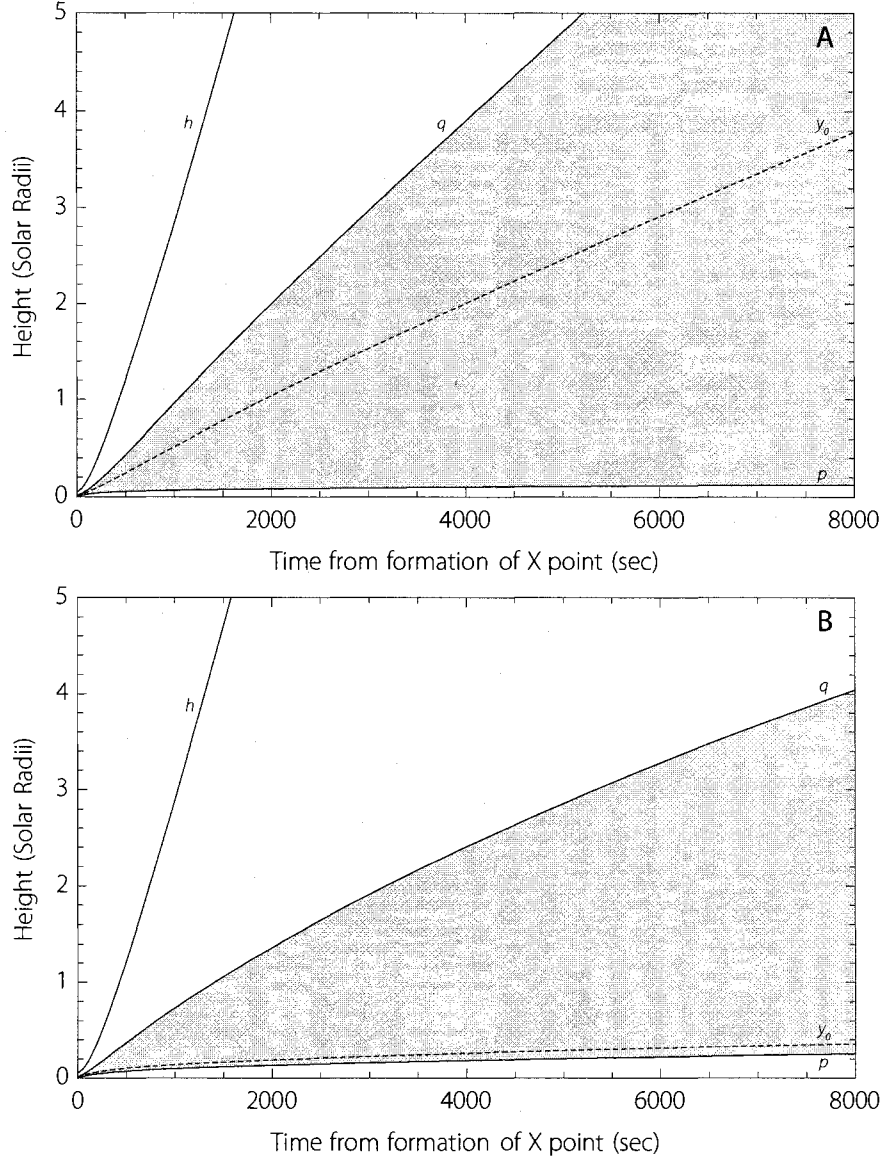
Figure 3-2: Trajectories of h (flux rope), q (upper current sheet tip), y_0 (x-line), and p (lower current sheet tip) calculated using the Reeves & Forbes assumption (Plot A) that $y_0 = (p + q)/2$ and the improved model (Plot B) where the x-line is placed at the pinch point. Both panels use the same reconnection rate, $M_A = 0.025$. The shaded region represents the length of the current sheet. The solid lines represent the parameters h, q, and p, while the dashed line represents y_0, the x-line's trajectory.

sheet, while figure 3-2B shows trajectories calculated using the improved model, where the x-line is located at the pinch point. Both calculations assume that the reconnection rate is $M_A = 0.025$. In the improved model, the eruption takes place a little faster (that is, the flux rope, h, rises a little more quickly) and the current sheet does not grow as long (p rises higher in the corona while q stays lower, for a net shorter current sheet). Since the Reeves & Forbes model uses the electric field to set the reconnection rate, the electric field is given by

$$E_z = M_A V_A(0, y_0) B_y(0, y_0)/c,$$

where $V_A(0, y_0)$ is the Alfvén speed measured at the x-line in the current sheet, and $B_y(0, y_0)$ is the background magnetic field measured in the same place. If y_0 is moved to a substantially lower point in the corona, the magnetic field measured there will be stronger. Since both the Alfvén speed and the background field depend on this value, an increase will result in an enhanced electric field and, therefore, an enhanced reconnection rate. For the case shown in Figure 3-2, E_z is enhanced by about an order of magnitude for a value of $M_A = 0.025$. Thus the event unfolds more quickly, the flux rope rises faster, and the current sheet reconnects away more quickly as well. However, one can recover a trajectory whose behavior is very similar to those obtained by Lin & Forbes (2000) and Reeves & Forbes (2005) by decreasing the value of M_A by the same factor as the increase in E_z. Since M_A is a free parameter in these models whose value has been adjusted to match observed flare emission, we conclude that Reeves & Forbes (2005) overestimated the values of M_A by about an order of magnitude.

Figure 3-4 shows a plot of trajectories for h, p, q, and y_0 plotted from a numerical CME model produced by the SAIC MHD code. (Figure 3-4 shows overview images from this MHD model.) Although this model does not correspond to the same parameters and background field strength, as those of Figure 3-2, it clearly confirms

that the x-line remains low in the current layer rather than rising to the midpoint of the current sheet as q becomes large.

One of the properties of the 2D model is that the flux rope cannot escape unless the reconnection rate exceeds a critical value (Lin & Forbes, 2000; Lin, 2002). If the reconnection rate is too slow, the current sheet will not reconnect away fast enough, and the erupting flux rope will slow down and, eventually, bounce back towards the surface. Figure 3-5 shows two examples of this type of behavior. In the first example, the flux rope bounces once before escaping, while in the second example, the flux rope bounces many times without escaping. The former case occurs when the inflow Alfvén Mach number, M_A, is too low for a straightforward escape, but high enough that an escape is physically possible. The latter case occurs when the inflow rate is so slow that the forces restraining the flux rope cannot be overcome until many bounces have occurred.

Using the assumption that the x-line is located at the center of the current sheet and using a density model (Sittler & Guhathakurta, 1999) like the one used in this model, Lin (2002) found that when $M_A < 0.013$ the flux rope cannot escape without at least one bounce, when $0.013 < M_A < 0.034$ the flux will not bounce, but will undergo deceleration. Finally, for $M_A \geq 0.034$ the flux rope will escape smoothly. Using the revised model discussed above with the same initial configuration as Lin used, we find that when M_A is less than about 3×10^{-4}, the flux rope cannot escape without at least one bounce. This number is around two orders of magnitude lower than its counterpart in Lin's work because the lower x-line location in our model yields a faster reconnection rate for the same value of M_A than that in the Lin & Forbes (2000) model. Thus the reconnection unfolds faster for a given inflow rate, and the flux rope escapes more easily. However, in terms of the value of the electric field at the x-line (i.e. $E_0 = -1/c \, dA_0/dt$) the rate is nearly the same. That is, the amount
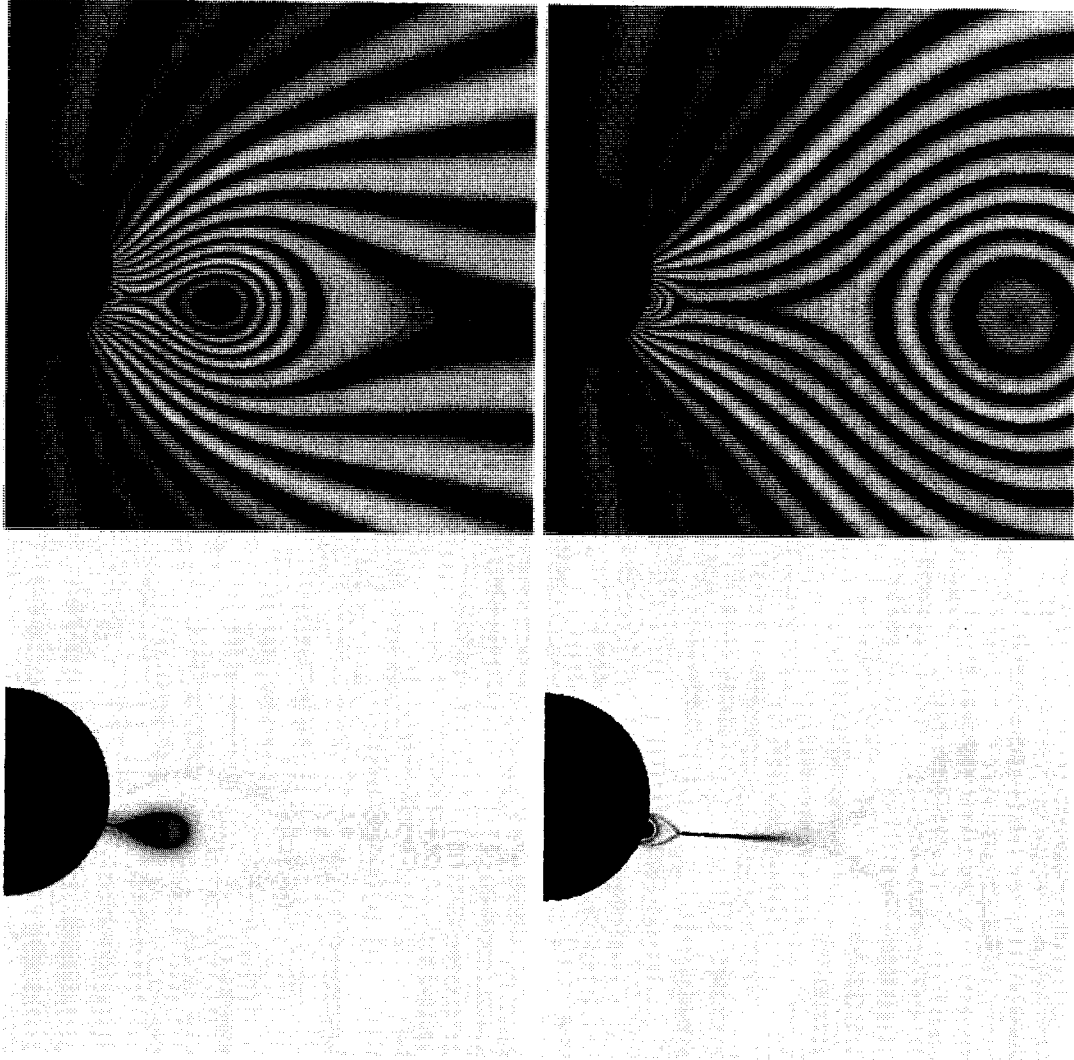
Figure 3-3: Panels from an SAIC CME model like the one from which the trajectories in Figure 3-4 are calculated. The top panels show projected field lines at two different times during the event, while the bottom panels show current density at the same times. (Figure from Forbes et al., 2006, used with permission.)
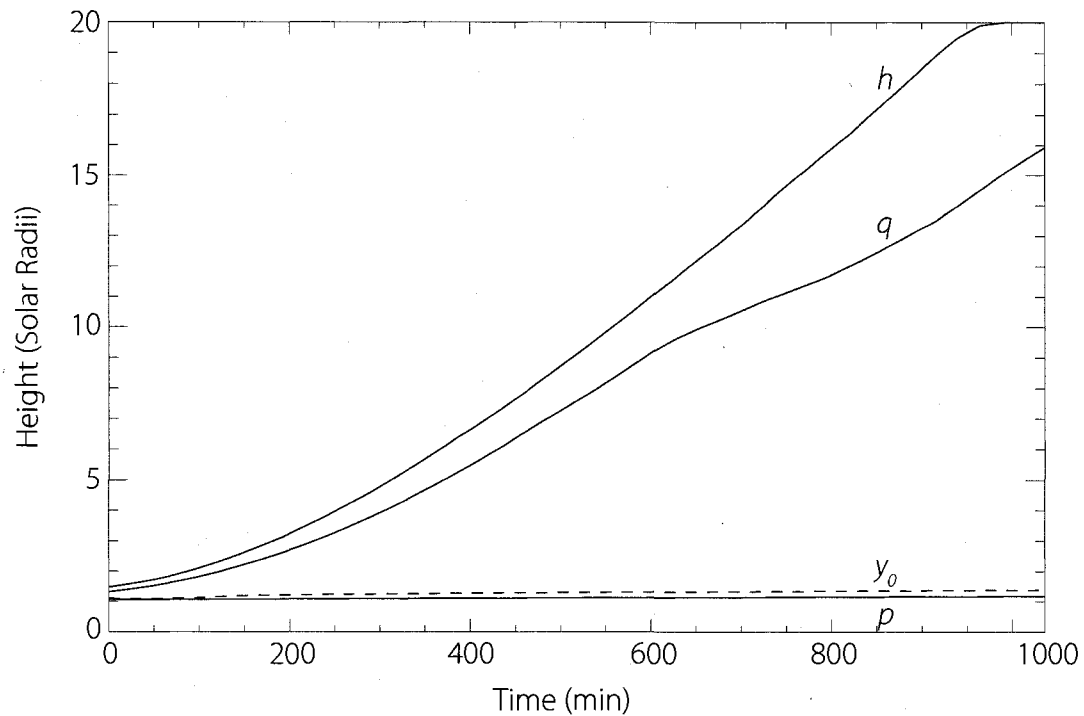
Figure 3-4: Smoothed trajectories for h, p, q, and the x-line location, y_0, dashed, computed with a numerical CME model (Reeves et al., 2008a). (Note that this case does not correspond to the same values of M_A and background fields as the case shown in Figure 3-2.) The bump in the curve for q may be a numerical artifact caused by difficulties in determining the position of q in the numerical model. (Data courtesy of K. Reeves, private communication, 2008.)

of magnetic flux that is being reconnected per unit time remains approximately the same. Because of the lower position of the x-line, the flow into the current sheet needed to maintain this rate is greatly reduced. Such a reduced value of M_A is actually more consistent with the value inferred from observations by Yokoyama & Shibata (2001) than the value obtained by Reeves & Forbes. Yokoyama & Shibata estimated an inflow rate of $M_A \approx 0.004$ during the late phase of the flare, a value that is more consistent with our own predicted value of M_A.

3.2.2 Improving Estimates of the Energy Release

Changes in the reconnection rate and length of the current layer affect the amount of the Poynting flux channeled into the current sheet. Since the Poynting flux is the source of the heat generated by reconnection, the heat channeled into the flare loops and ribbons is sensitive to any change in the reconnection rate and to any change in the division of energy between upward and downward directed flows. The location of the x-line determines the division point for upward and downward directed reconnection jets. So when the x-line location is significantly closer to the bottom tip of the current sheet the majority of incoming Poynting flux that is converted into heat and kinetic energy is channeled into the upward jet. Here, we will continue with the same case as above (120 G background field) and examine the effect of the relocation of the x-line on the overall energy budget of the reconnecting current sheet.

The total energy of this system is, at any time, given by

$$W_{mag} + W_{KE} + W_{th} = W_0, \tag{3.10}$$

where W_{mag} is the free magnetic energy, W_{th} is the kinetic energy of the flux rope, W_{th} is the thermal energy, and W_0 is the initial energy of the system. Since, W_0 is not a function of time,

$$\frac{d}{dt}(W_{mag} + W_{KE} + W_{th}) = 0. \tag{3.11}$$
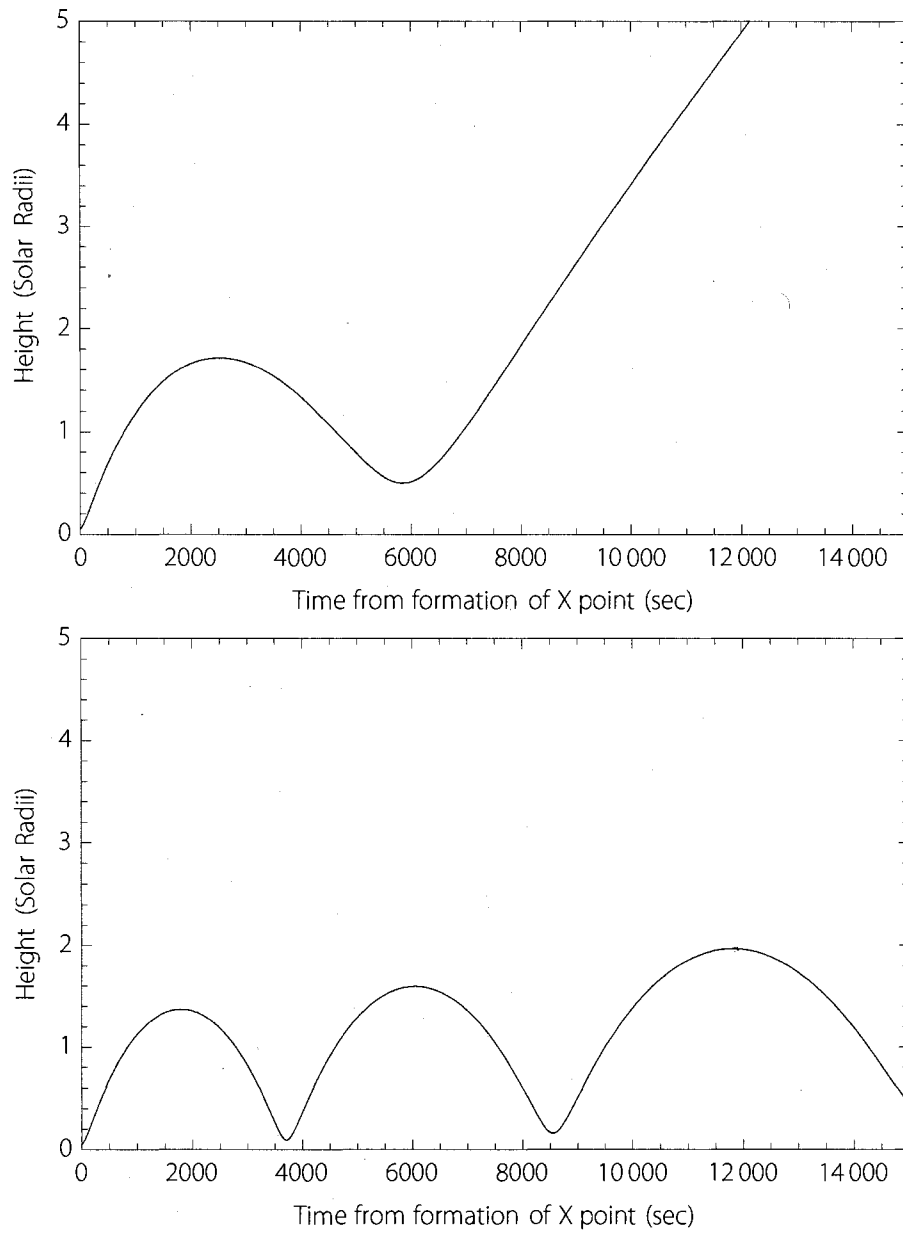
Figure 3-5: Flux rope height versus time for two scenarios containing a bouncing flux rope under the new asymmetric reconnection model. The upper curve ($M_A = 10^{-4}$) bounces once before escaping. The lower curve ($M_A = 2.5 \times 10^{-5}$) continues to bounce without an escape.

Following Reeves & Forbes we can then write the rate of change of the kinetic energy of the flux rope—the kinetic power—

$$\frac{d}{dt}\left(\frac{1}{2}m\dot{h}^2\right) = m\ddot{h}\dot{h} = F\dot{h}, \tag{3.12}$$

where m is the mass of the flux rope and, F, the force on the flux rope, is given by $F = (I/c)B_{ext}$. Here I is the current in the flux rope, given by Equation 3.2 and B_{ext} is the external magnetic field, which is given as B_{ya} in Equation 3.6.

To calculate changes in time as a function of the model parameters h and p we write

$$\frac{d}{dt} = \frac{\partial}{\partial h}\dot{h} + \frac{\partial}{\partial p}\dot{p}. \tag{3.13}$$

Here the first term represents changes due to the motion of the flux rope, while the second term accounts for changes due to reconnection. In the case of the thermal energy,

$$\frac{\partial W_{th}}{\partial h}\dot{h} = 0$$

because there is no reconnection when p remains constant and, therefore, no heating in the model. Thus we can write the thermal power as

$$\frac{dW_{th}}{dt} = \frac{\partial W_{th}}{\partial p}\dot{p}.$$

If we hold h constant and rewrite Equation 3.11, we find

$$\left.\frac{\partial W_{mag}}{\partial t}\right|_h + \frac{\partial W_{th}}{\partial p}\dot{p} = 0.$$

We can then use the preceeding two equations, along with the fact that

$$\left.\frac{\partial W_{mag}}{\partial t}\right|_h = -S(t),$$

where $S(t)$ is the integral of the Poynting flux along the current sheet, to conclude that
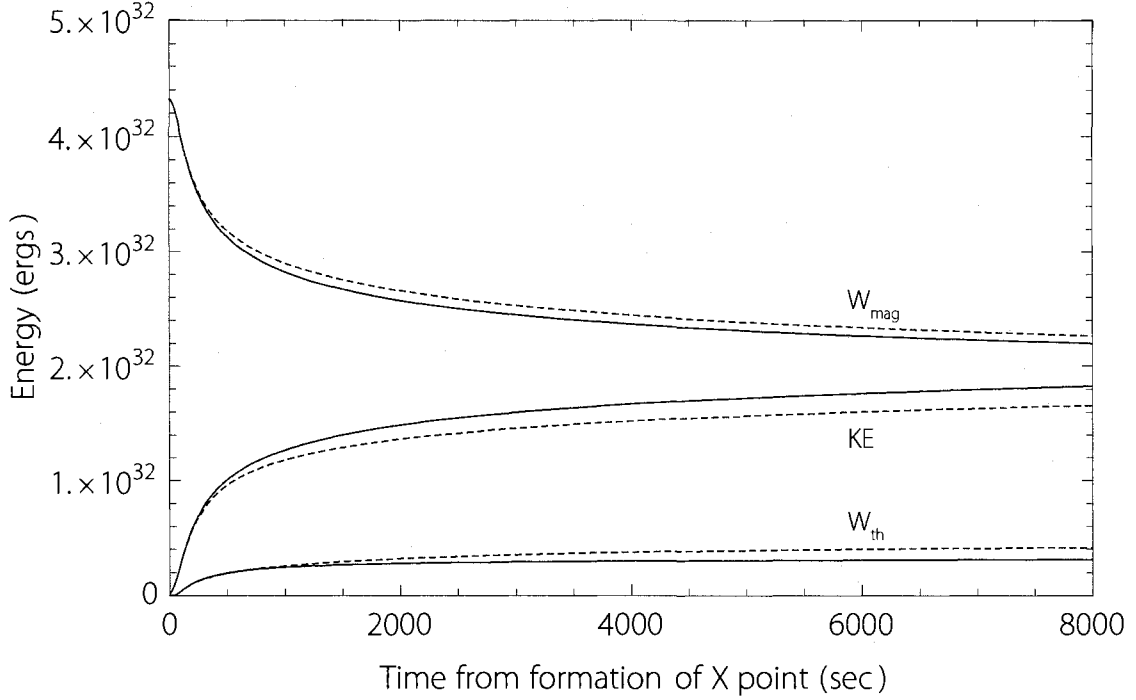
Figure 3-6: Eruption energy as a function of time for the Reeves & Forbes model and our new model. In both cases, the plots correspond to an inflow Alfvén Mach number $M_A = 0.025$ and background field of 120 G. The dashed curves refer to the Reeves & Forbes results (with $y_0 = (p + q)/2$), while the solid curves refer to the new result with y_0 located at the pinch point. Because the eruption proceeds faster in the new model, the kinetic energy is increased slightly, while the faster overall reconnection reduces the heating slightly.

$$\frac{dW_{th}}{dt} = S(t). \tag{3.14}$$

Making use of Equation 3.11, finding the magnetic energy is then straightforward. We can then solve the differential equations described in Reeves & Forbes and solve the system to obtain the energetics of the system.

Figure 3-6 shows the energetics of the system for both the Reeves & Forbes current sheet assumptions (dashed lines) and the new pinch point model (solid lines). Because

the eruption occurs more quickly in the newer model, there is more kinetic energy. At the same time, the faster reconnection rate leads to a shorter current sheet and less integrated Poynting flux, and thus less heating. Overall, the new model uses up slightly more of the background magnetic energy.

These adjustments in the overall energy are small, however, compared to the adjustments in power, particularly the adjustment to the thermal power that enters the downward jet. Reeves & Forbes arbitrarily assumed that half of the total thermal power goes up and half down. Now that we have a more physically-based model for the location of the x-line, we can determine the diversion of the incoming magnetic energy as a function of the parameters and time. According to our reconnection model, any Poynting flux that enters the current sheet below the x-line will energize the downward directed plasma, while any Poynting flux that enters above the x-line will energize the upward directed plasma. Thus in order to calculate the amount of power entering the downward jet, we simply integrate the Poynting flux entering the current sheet between p and y_0. As did Reeves & Forbes, we assume that all of the Poynting flux is eventually thermalized, although in practice some of the kinetic energy in the jet may be thermalized in the system.

Figure 3-7 shows plots of the amount of thermal power that enters the downward jet, and is therefore available to heat the lower corona. Because the current sheet is essentially symmetric at the beginning of the event, both curves are very similar at the beginning of the eruption. However, in our case, the power drops quickly to only about 1/10 of the power available in the Reeves & Forbes case. Figure 3-8 shows the power in the new case as a function of the total thermal power (or Poynting flux) entering the current sheet. After the first 100 seconds of the event, only about 10% of the total incoming flux enters the downward directed jet.

We can also take a broader look at the division of flux flow in the current layer.
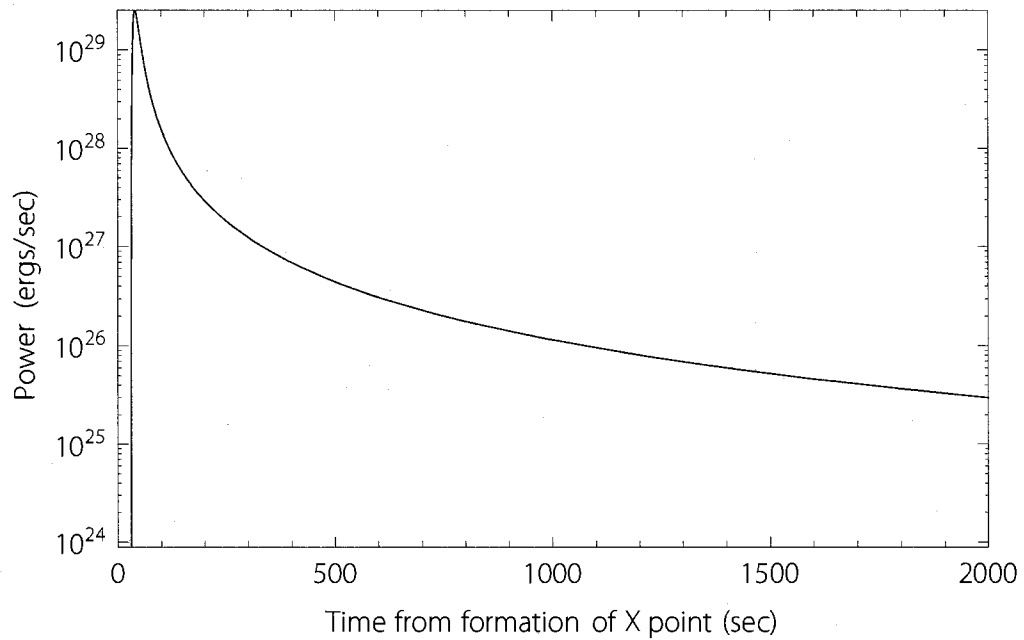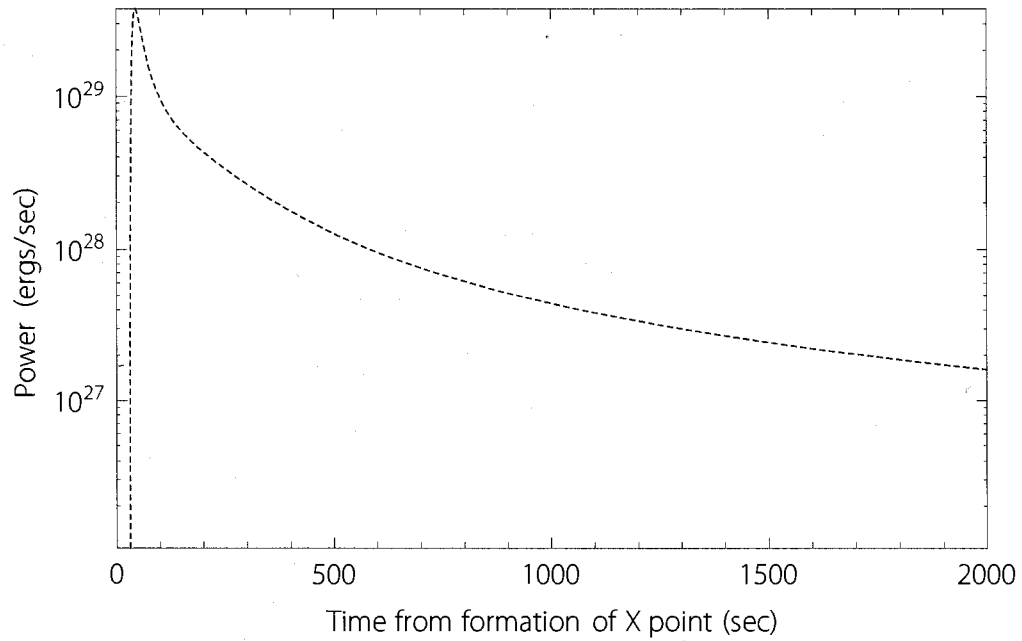
Figure 3-7: Power entering the downward jet for the Reeves & Forbes assumption that the x-line is located in the middle of the current sheet (dashed line) and the new model, where the x-line is located at the pinch point (solid line). The parameters for the CME modeled in these plots are the same as those used in the energy calculation shown in figure 3-6.
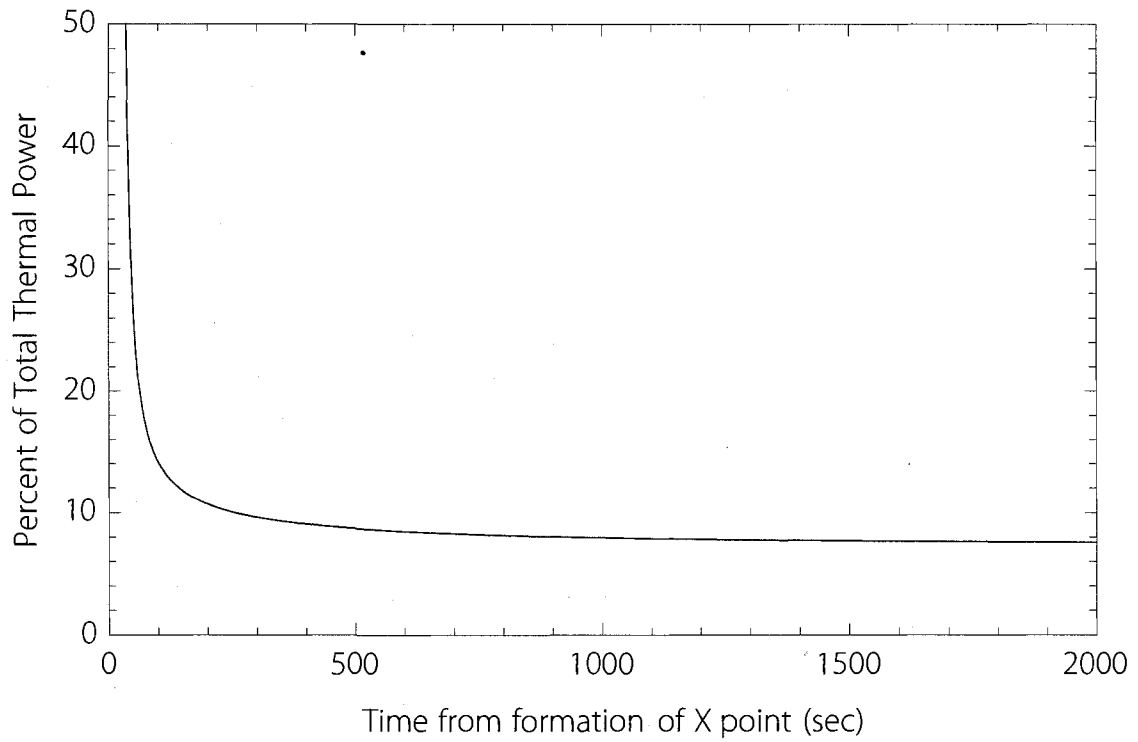
Figure 3-8: Power in the downward jet for the new model with the x-line located at the pinch point. The case shown here is for the same parameters as the case shown in 3-7. The power is plotted as a percentage of the total Poynting flux entering the current sheet.
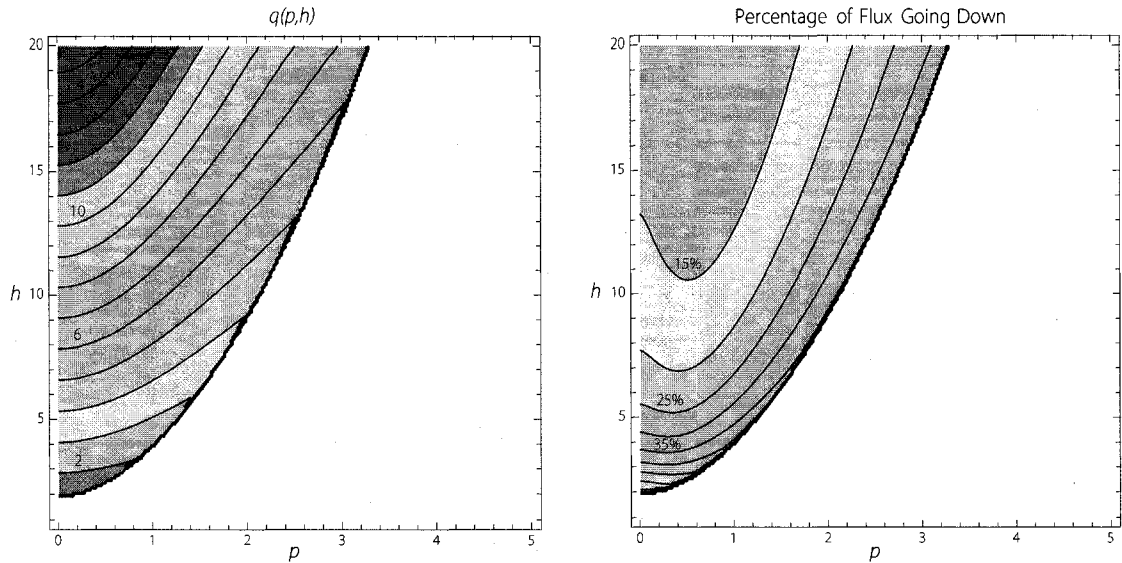
Figure 3-9: The location of the upper tip of the current sheet, q (left panel), and the percentage of flux in the downward jet (right panel) plotted as a function of the location of the bottom of the current sheet, p, and the flux rope, h, calculated for the case of a very small flux rope radius.

The right panel of figure 3-9 shows what percentage of incoming Poynting flux enters the downward jet as a function of p and h. The left panel shows the location of q in the same case. We note that the incoming Poynting flux is only distributed evenly between the upward and downward jets in the case where h, p, q, and λ are all of the same order, and thus the sheet is very symmetric. As soon as h begins to lift off, a much larger percentage of entering flux is diverted into the outgoing jet, while only about 10 to 15% of the incoming flux enters the downward jet.

These results suggest that, for a given value of M_A, Reeves & Forbes over-estimated the amount of heating during an eruption by a considerable amount. There are two contributions to this discrepancy between the new and old models. First, because the Reeves & Forbes model underestimates the effective rate of reconnection for a given value of M_A, they predict more overall heating to take place during the event

than should, in fact, occur. As Figure 3-6 makes clear, this is a relatively small effect. Second, and more significantly, their model assumes that 50% of the incoming Poynting flux is directed into the downward jet, when, in fact, only about 10% of the incoming flux should enter the jet once the eruption is well underway (that is, after a few minutes). An important point to keep in mind, however, when comparing the old and new models, is that the dimensionless reconnection rate M_A remains an adjustable parameter. As we noted earlier, Reeves & Forbes adjusted this parameter to provide the best match between model behavior and observations. However the values obtained are larger than those inferred in the Yokoyama & Shibata (2001) observations. With the new model there is no longer a significant discrepancy between the observed and predicted values of M_A.

3.3 Modeling the Asymmetric Current Layer

Although the Somov-Titov formalism is insufficient to determine the reconnection rate, it does provide a more realistic description of the magnetic field and flow structure of the current layer than the previous models of Lin & Forbes (2000) and Reeves & Forbes (2005). A key issue that we will address in this section is the effect of the asymmetry introduced into the flare reconnection process by the decrease of the solar magnetic field with height. So far, very little work has been done within the solar research community which specifically addresses this issue.

Although several numerical simulations have been carried out in 2D (e.g. Yokoyama & Shibata, 1997, 2001) and 3D (e.g. Roussev et al., 2003; Kliem & Török, 2006) which are asymmetric, there have been no studies published that examine the nature of the outflow from the reconnection region. One of the main reasons for this may be that most of these simulations lack a realistic resistivity model. In most cases (especially the 3D cases) the resistivity is numerical. Another reason may be that most of the

solar MHD models do not use a proper energy equation, but instead use an equation of state with an *ad hoc* polytropic index to relate the gas pressure to the density. In either case, obtaining a physically meaningful description of the diffusion region becomes problematic.

In this section, we will apply the Somov-Titov procedure to a current layer whose exterior field is consistent with the asymmetric field of the Lin & Forbes (2000) and Reeves & Forbes (2005) models (Equation 3.6 above). We use equations 2.13 through 2.16 from Chapter 2 (for the $\langle B_x \rangle = 0$ case), replacing only B_{xa} with the new external field (Equation 3.6). As before, we normalize magnetic field to B_{xa} at the point $x = 0$, $y = a_0$ so that $B_{xa}(0) = -1$.

3.3.1 Sweet-Parker and Petscheck-like Solutions in the Asymmetric Case

In chapter 2, we discussed the Somov-Titov solutions that use a symmetric, Syrovatskii-like background magnetic field. These solutions range from Sweet-Parker-like to Petscheck-like, depending on the assumed length of the diffusion region, α. When the length of the diffusion region is small compared to the length of the Syrovatskii current layer, the solutions become Petschek-like, with the small diffusion region in the center of the current layer, and most of the current layer composed of the slow-mode shocks. In these Petschek-like cases, plasma parameters such as the flow speed, $\langle V_x \rangle$, and field strength, $\langle B_y \rangle$, rise rapidly inside the diffusion region, reaching their maximum values (V_{Ai} and M_A) quickly, and then remain nearly uniform in the shocks region. When α is near unity, we obtain solutions that look like the Sweet-Parker solution. Here $\langle V_x \rangle$ and $\langle B_y \rangle$ gradually increase over the length of a large diffusion region that runs the full length of the current layer.

Solutions to the asymmetric current sheet problem share many of the same general characteristics as their symmetric-system counterparts. These solutions can exhibit

both Sweet-Parker and Petschek-like behavior, depending on the value of α and, to a lesser extent, β (see chapter 2). However, because of the asymmetric nature of the external background field, the character of the solution on either side of the x-line will tend to be different. If we choose α such that it produces a Sweet-Parker-like solution on the upward flowing part of the current layer, then the downflowing part contains a normal magnetic field component that reverses sign (i.e. a magnetic island). Figure 3-12 shows an example of a solution featuring this type of magnetic field reversal. If we choose α such that it produces a Sweet-Parker-like solution on the downflowing end, the upflowing end will be Petschek-like. As figure 3-11 shows, using the highly asymmetric background field shown in Figure 3-10, only one side of the current layer (the downward flowing side) is Sweet-Parker-like. Cases that are Petschek-like on both ends of the current sheet do exist, but the shocks region is considerably more extended above the x-line than it is below. It is only possible to obtain Sweet-Parker solutions through the current layer by choosing model parameters that result in a current layer so short that it is nearly symmetrical.

This result leads to the following conclusion: in the case of asymmetric, steady-state reconnection, it is impossible to acheive a simple Sweet-Parker solution (i.e. one without a magnetic island and without a Petschek region) in the presence of magnetic field that decreases rapidly with altitude in the corona.

The reason for this is straightforward: for a given variation of the external field, there exists a particular value of α (near unity) that will produce a Sweet-Parker type current sheet. In a highly asymmetric case, however, the external field variation is different above and below the x-line, so that the value of α needed to obtain a Sweet-Parker solution is different in the two regions. Because $\alpha = 1/\left(L_u M_A^2\right)$ and L_u and M_A are globally defined parameters, there cannot be different values of α above and below the x-line. Thus a Sweet-Parker solution can exist in only one of the two
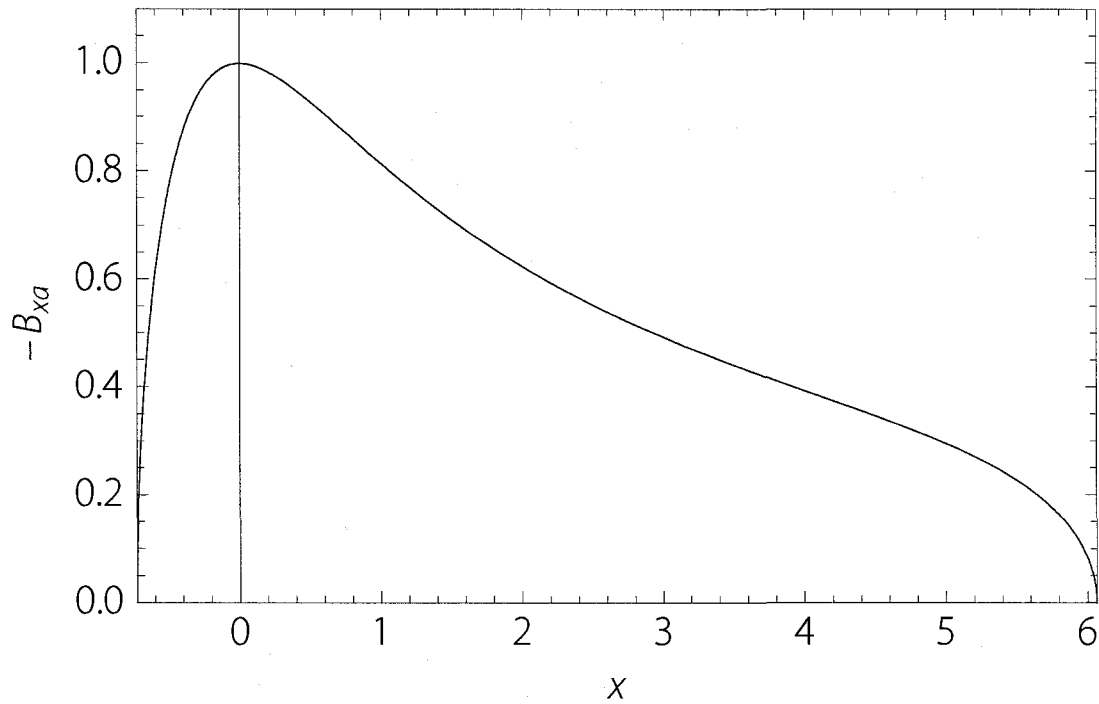
Figure 3-10: Tangential magnetic field component of Lin & Forbes (2000) along the length of the current layer. The location $x \approx -0.6$ corresponds to the lower tip of the current layer (or sheet) and $x \approx 6.1$ to the upper tip. The x-line is located at $x = 0$, the pinch point. This field is used in the calculation of solutions seen in Figure 3-11.
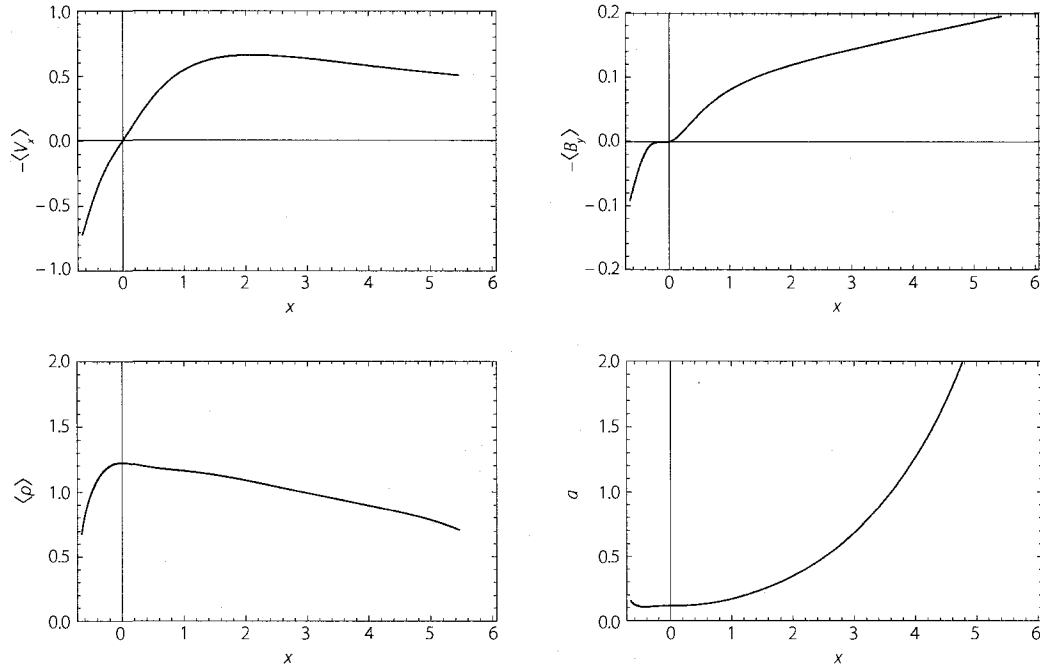
Figure 3-11: An asymmetric solution for the outflow speed, $\langle V_x \rangle$, the magnetic field, $\langle B_y \rangle$, the density, $\langle \rho \rangle$, and current layer thickness, a, as a function of the distance x along the layer. Outside the diffusion region a corresponds to the distance between the slow shocks. Here $M_A = 0.1$, $L_u = 85$, and $\beta = 0.1$, while the background magnetic field corresponds to that shown in Figure 3-10. Notice that, while the downward pointing jet is Sweet-Parker-like, the upward jet resembles Petschek. A pure Sweet-Parker solution is not possible in the case of an asymmetric current sheet.
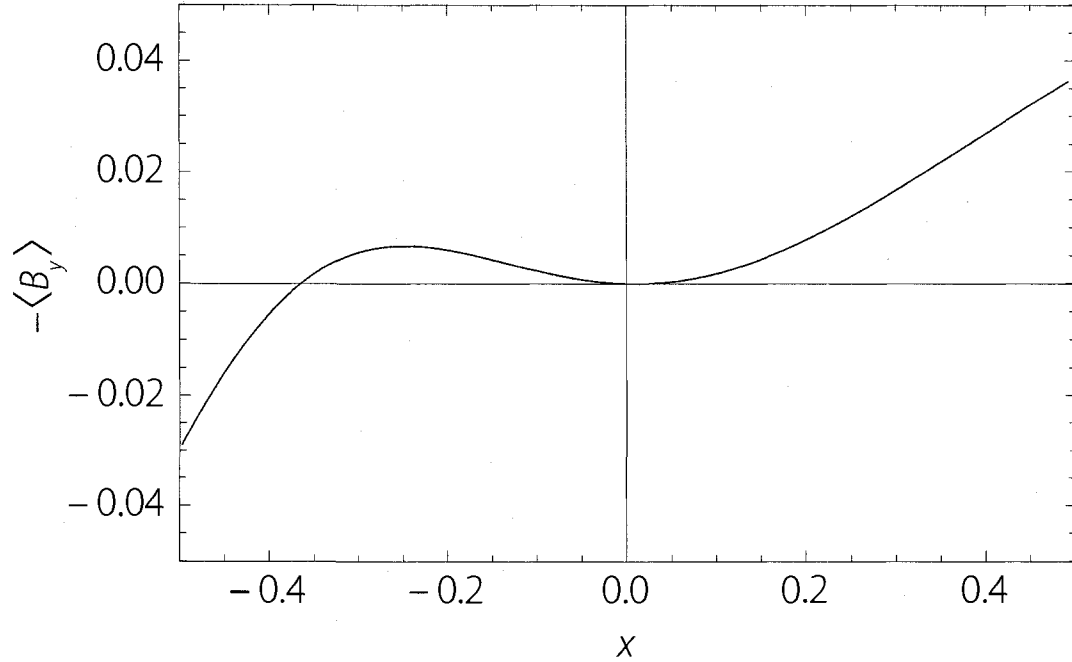
Figure 3-12: A close-up example of the type of magnetic island that can form when the α chosen is less than the critical value of α (see chapter 2) on one side of the x-line (the left side, in this case) while greater than the critical value of α on the other (right side).

regions for a given set of parameters.

If the upper region is forced to be Sweet-Parker-like, then the lower region will have a field reversal (i.e. a magnetic island), so it is no longer a simple Sweet-Parker current sheet. The formation of an island in the downflow region may indicate a breakdown of the steady-state assumption since such stationary islands are not seen in numerical simulations to our knowledge. Two-dimensional MHD numerical simulations by Forbes (1986) suggest that the downward jet is greatly reduced in solutions with β greater than about 1 and that most inflowing plasma is directed into the upper jet. For low β solutions ($\beta \ll 1$) with outflow fast-mode Mach numbers greater than 1, a downward jet does occur. However, as in our steady-state solutions, the length of this jet is very short compared to the upper jet.

That the Sweet-Parker solution seems to be difficult to obtain in this asymmetric framework does not necessarily mean that such asymmetric Sweet-Parker solutions will be impossible to obtain in general. We know from our expansions near $x = 0$, for example, that the addition $\langle B_x \rangle$ will increase the critical value of α. Thus the addition of tangential magnetic field to the solution may help to allow the upper jet to be more Sweet-Parker-like without triggering a field reversal in the lower jet. Additionally, a more general approach to this problem such as a complete numerical model might allow the formation of additional external current structures or other complex effects that cannot occur in this relatively simple model. Thus, while we cannot conclude that Sweet-Parker will not occur in an asymmetric framework, there is some evidence to suggest that slow reconnection solutions in this region are more complex than the simple Sweet-Parker treatment.

Obtaining Petschek-like solutions throughout the current layer requires only that we choose α to be much smaller than the length of the shorter of the two jets, so the length of the diffusion region will be short. It is possible to choose α so that the diffusion region in both the upward and the downward jets is much shorter than the length of the current layer. In this case, while the asymmetry in the external background field outside the current layer will continue to have an effect on the solution, the short diffusion region essentially forces Petschek-like behavior on each side of the x-line. Thus it remains possible to recover solutions that are fundamentally Petschek-like, albeit with a diffusion region that may be asymmetrically shaped.

3.3.2   Properties of the Asymmetric Solutions: Flows

In the past ten years or so, several authors have reported on their observations of flows above postflare arcades during flares and other eruptions. One of the most dramatic examples of these features are the downflows observed by the *Transition*

Region and Coronal Explorer (TRACE) spacecraft (Handy et al., 1999) during the X-flare on 21 April 2002. These flows, referred to as supra-arcade downflows (SADs), appeared as dark voids in a diffuse structure, interpreted to be high temperature plasma (15–20 K) producing emission in the Fe XXIV line (Gallagher et al., 2002). Because these flows are embedded in such high temperature plasma, they have been interpreted as being outflows from reconnection (Asai et al., 2004). Earlier, using the Soft X-ray Telescope (Tsuneta et al., 1991) on *Yohkoh*, McKenzie & Hudson (1999) and McKenzie (2000) observed similar flows moving with speeds between 50 and 500 $km\,s^{-1}$ above post-flare arcades. Because observations of such post-flare flows remain relatively rare, this phenomenon is still not well understood. Several authors have expressed hope that *Hinode* observations will help shed light on their nature (McKenzie et al., 2007). Such flows have already been observed by *Hinode*, but because *Hinode* was launched in October 2006 during solar minimum, there have been few flares observed and the type of large limb event needed to see these flows well has yet to be observed.

Inflows have also been observed in the extended corona using the LASCO coronagraph onboard *SOHO* by Sheeley & Wang (2002). These flows, which reach maximum speeds between 50 and 100 $km\,s^{-1}$, occur frequently during periods of solar activity. Occasionally the inflow is accompanied by an outgoing partner. These events, which are called "in-out pairs" are believed to be the result of a special class of CMEs called "streamer blowouts" (Sheeley & Wang, 2007). Because of their relationship to eruptions, it is reasonable to infer that at least some of these events are also the product of (or related to) magnetic reconnection.

Because all of these flows occur at speeds much slower than the Alfvén speed, some authors have dismissed the idea that they could be directly related to reconnection outflow, which is generally thought to occur at or near the Alfvén speed (McKenzie

& Hudson, 1999). However, because so few models of such reconnection flows in a realistic, asymmetric background exist, confirming this interpretation has been difficult. So one of the questions we would like to answer with this model is exactly what characteristics we might expect such post-flare flows to exhibit.

The speeds of the outflows from the reconnection site are strongly influenced by the presence of thermal conduction, so we will return to this question in chapter 4 of this thesis. Nonetheless, the symmetry of the background field also influnces the characteristics of these flows as well.

In most cases, both symmetric and highly asymmetric, both the upwards and downwards directed jets reach approximately the same maximum speed (the exact speed depends on the model's input parameters, but the two jets nontheless share about the same maximum to within 5%). However, the downward jet tends to achieve its maximum speed only as it reaches the lower tip of the current layer. In highly asymmetric cases, the upper jet reaches its maximum speed close to the x-line. This appears to be the related to the dramatic widening of the upper layer that occurs in highly asymmetric cases (an example of which can be seen in Figure 3-11) and is indicitave of the divergence of the slow-mode shocks above the x-line.

In no case does the velocity of a jet reach, or exceed, the inflow Alfvén speed, corresponding to a value of 1 in normalized units. This behavior mirrors the behavior of the symmetric solutions, which, at their fastest, come within a few percent of the Alfvén speed, but do not exceed it.

On the other hand, the fast-mode Mach number of each jet, which depends strongly on the temperature of the flow, behaves in the opposite way. The temperature of the upward directed jet tends to be lower than the temperature of the downward directed jet. As a result the fast-mode velocity is lower in the upper jet, which serves to increase the fast-mode Mach number of the upper jet slightly, by a

factor of about 1.5 at the most. There are many cases where the upper jet's Mach number is higher than 1, while the lower jet's Mach number is not. Of course, because of the role of temperature in determining the fast-mode Mach number, the presence of thermal conduction plays a much bigger part in determining the Mach number than the background field. Thus we will revisit this question, in particular, in chapter 4, which considers the effects of thermal conduction on the solutions.

We also considered whether the formation of magnetic islands might have a significant effect on the behavior of the jets. (In particular, the downward jet, since that is where magnetic islands most commonly form.) While it does appear that the velocity curve develops a very slightly kinked shape when a magnetic island is present, this effect is small, and it does not appear to cause any other behavior of note.

The observations of in-out pairs by Sheeley & Wang (2007) have some interesting characteristics that are worth noting in the context of these results for our asymmetric model. Many of these pairs are triggered by the eruption of a CME. When these pairs of flows occur, the downflowing component is generally narrow, while the upward flows begin as wide features that expand as they rise in the corona. Like these, our asymmetric models show a downward pointed jet that is very narrow compared to the upward going jet and is also relatively uniform in thickness along its length. The upward jets, however, often widen dramatically, until they may be just as thick as they are wide. Both of these properties are very similar to the features of in-out pairs. Sheeley & Wang (2007) interpret their observations of the outgoing component of these pairs to be a signature of a flux rope rising in the corona. However, our model results suggest a possible alternative interpretation: that the outgoing flow is related to reconnection in a highly asymmetric field.

3.3.3 Properties of the Asymmetric Solutions: Other Characteristics

Ciaravella et al. (2002), Raymond et al. (2003), and Ciaravella et al. (2006) studied the properties of the current sheets that formed in the wake of several CMEs using the Ultraviolet Coronagraph Spectrometer (UVCS) onboard *SOHO* (Kohl et al., 1995). UVCS allows observers to obtain a series of spectra for a number of prominent coronal emission lines for points all along a long slit. Thus it provides a way to measure the properties of the plasma—temperature, density, etc.—across a cross-section of the corona.

Ciaravella *et al.* placed the slit perpendicular to the direction of CME travel, so that as the CME lifted off, the slit spanned the current sheet they expected would form in its wake. Using diagnostic emission lines they were able to estimate some of the properties of the current layer, most specifically, that the density was enhanced by a factor of about 2.5 over ordinary coronal values, and the temperature (for different current sheets during different events) spanned a range of values from 10^6 K, close to the coronal background temperature, to 10^7 K, a full order of magnitude hotter. Thus we asked whether these properties might be affected by the asymmetric nature of the background field.

In the symmetric case, the density at the x-line depends strongly on plasma β, ranging from 1, in normalized units, in the incompressible, very high β case, up to about 1.25 in the case of low β. When the reconnection is Sweet-Parker-like, this value often represents the maximum value, and density falls off as you approach the ends of the current layer. When the reconnection is Petschek-like, the density is often at a maximum at a point about 25% of the way between the x-line and the tip of the current layer and, while this maximum value also depends on the plasma β, it never reaches a value much higher than about 1.75.

The asymmetric case behaves similarly. Although the variation in density along

the current layer is functionally different from the symmetric cases, the basic properties remain the same. The degree of density enhancement in both jets is nearly the same, and the maximum and minimum values are about the same as well. In highly asymmetric cases the density falls off more slowly in the upper jet than in the lower one, but the degree of the falloff is about equal, with the density reaching approximately the background value near the tips of the current layer.

Temperature and density are linked, so it is perhaps not unsurprising that our findings about the asymmetric background field's effect on temperature are similar to our findings about its effect on density. In both the symmetric and asymmetric cases, the temperature reaches a maximum at the x-line. The exact value of this temperature depends on plasma β. In the case of very low β, high temperatures are achieved, while in the case of very high β, little heating occurs and the temperature does not rise much above the background. For $0.1 < \beta < 1$, values corresponding to those observed in the corona, the maximum temperature ranges from about 10 times the background in the lower β case to 2 times the background in the higher β case. These predictions agree well with the Ciaravella et $al.$ findings.

There is, however, an important difference between temperature behavior in the symmetric and asymmetric cases. In both cases, the temperature falls off with distance along the current layer, reaching temperatures that range from the background temperature in a few cases up to a few times the background temperature in others. In the asymmetric case, the temperature of the upper jet consistenly cools more than that of the lower jet. In the most extreme cases, the temperature of the outgoing jet may be as much as 2 times the temperature of the downgoing jet.

As we will see in chapter 4, density and temperature are both strongly affected by the presence of thermal conduction. So we will revisit this question later to see how thermal conduction affects these properties.

CHAPTER 4

THE EFFECTS OF THERMAL CONDUCTION

Thermal conduction plays a major role in both energetic losses and the dynamics of reconnecting current sheets. The conduction of energetic particles and electrons along field lines that map from the reconnection site to the chromosphere is essential for the creation of flare ribbons and loops (see chapter 1 for a complete discussion of these phenomena). During the last ten years, several numerical similations have been carried out to test various proposals (such as those by Cargill et al., 1995) on how reconnection and conduction lead to the formation of flare loops, and to a lesser extent, flare ribbons. Perhaps the most significant simulations of this type are those carried out by Yokoyama & Shibata (1997, 2001). They conducted MHD simulations of flare current sheets with models that both included and excluded thermal conduction, so their work makes especially clear the specific effects of conduction on the plasma in and around the reconnecting current sheet. Their simulations impose a nonuniform resistivity at the x-line at $t = 0$ to initiate the Petschek-type reconnettion in the current layer. Their later simulations (e.g. Yokoyama & Shibata, 2001) also include the effects of line-tying of the magnetic field to the solar surface, as well as the effects of chromospheric evaporation (see chapter 1).

Figure 4-1 and Figure 4-2 show comparisons of the temperature and pressure, as well as field lines and fluid flow, in and around the current layer for one set of

simulations (1997) when conduction is not present and when it is. One of the most notable effects of conduction is to expand the region in which plasma has been heated to include not only the current sheet, but also the surrounding plasma. (The fact that thermal conduction causes heat to flow from the high temperature current layer into the surrounding plasma may seem obvious, but very few studies have examined how this process happens and how it affects other parameters.) We refer to this region of hot plasma surrounding the current layer as the "thermal halo" region. Figure 4-3 shows cuts across the current layer of temperature and density taken from another of the Yokoyama & Shibata models (2001). These plots make clear the location of the hot current layer and the surrounding thermal halo.

It is clear from these figures that conduction noticably changes the behavior of the plasma near the current layer. In addition to increasing its temperature, conduction also affects the flows and magnetic field in this layer, accelerating the tangential flow while reducing the tangential field. Therefore, in order to understand the complete effects of thermal conduction, we want our model to include the effect of thermal conduction on the thermal halo surrounding the current layer, as well as the current layer itself.

4.1   Thermal Conduction & Slow Shock Structure

Somov & Oreshina (2000) have previously done a rough analysis of how thermal conduction modifies the reconnection process, but their analysis is too simple to allow direct comparison with numerical simulations like those of Yokoyama & Shibata (1997, 2001). First, Somov & Oreshina treat the thermal conduction in their model as a simple energy loss term, and do not consider the effects of heat flow out of the current sheet on the surrounding plasma. Consequently, their model mixes together the halo and the jet regions, so that they do not accurately predict the properties
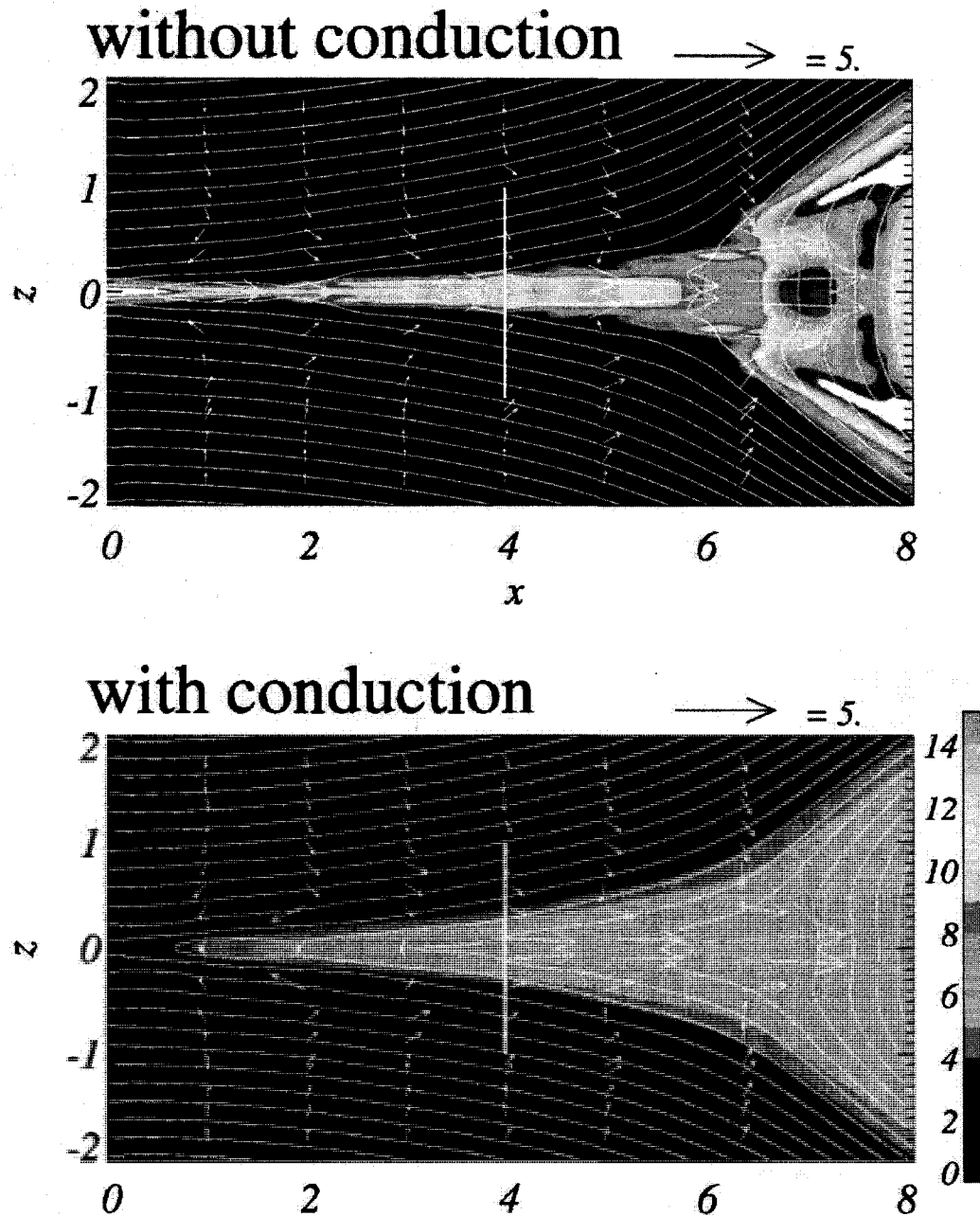
Figure 4-1: Temperature maps shown without (top) and with (bottom) conduction, from Yokoyama & Shibata (1997). The vertical line shows the approximate location at which parameters were measured, while arrows show flow velocity vectors. (Figure from Yokoyama & Shibata, 1997, used with permission.)
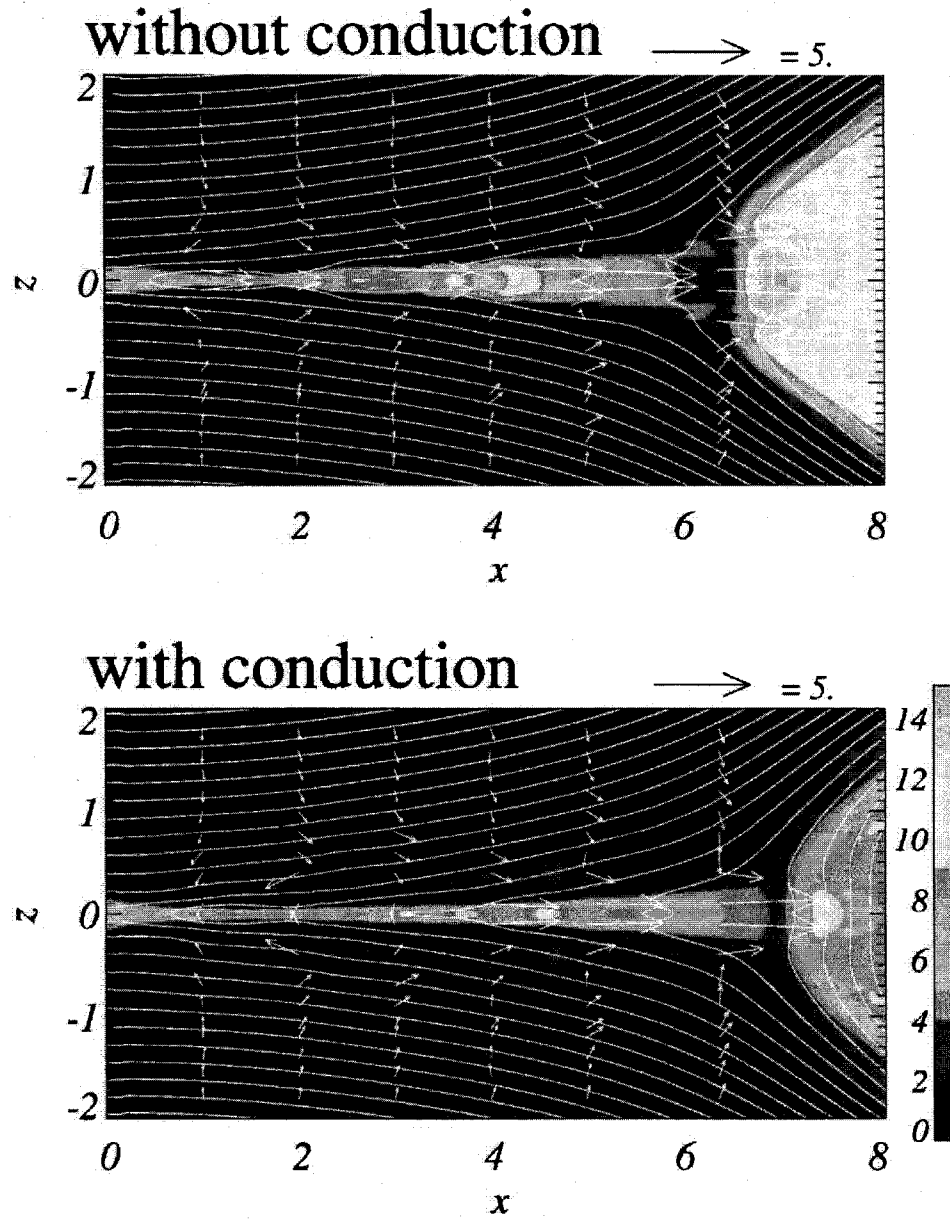
Figure 4-2: Pressure maps shown without (top) and with (bottom) conduction, from Yokoyama & Shibata (1997). (Figure from Yokoyama & Shibata, 1997, used with permission.)
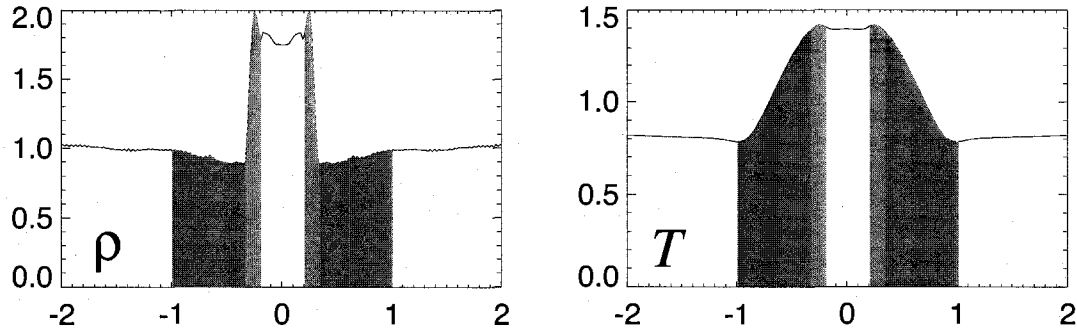
Figure 4-3: Cross-sections showing the variation of density (left) and temperature (right) across the thermal halo and current layer in Yokoyama & Shibata (2001). The dark shaded region represents the thermal halo region, the light shaded region represents the locations of the slow-shocks which surround the current layer. (Figure from Yokoyama & Shibata, 2001, used with permission.)

of either region. Here, we offer a more complete model, where we do consider the effects of heat flowing out of the current layer on the plasma that surrounds it. This allows us to make a better comparison between the results of our own modeling efforts and other numerical models, which consider both the current layer and surrounding regions. Figure 4-4 shows a schematic of the configuration of the revised solution with a thermal halo and central current layer. As we will see in the next section, we can use work by Xu & Forbes (1992) to determine the relationship between properties of the thermal halo and current layer.

Second, they use an anomalous heat flux term in their energy equation for the thermal conduction (Manheimer & Klein, 1975; Manheimer, 1977). However, evidence from the case with no thermal conduction, described in chapter 2, suggests that the temperature of the current layer in weak magnetic field eruptions may not be high enough to require the use of this anomalous heat flux term. Additionally, Yokoyama & Shibata use a classical heat flux, so in order to compare to their numerical models, we should adopt the same basic fomula.
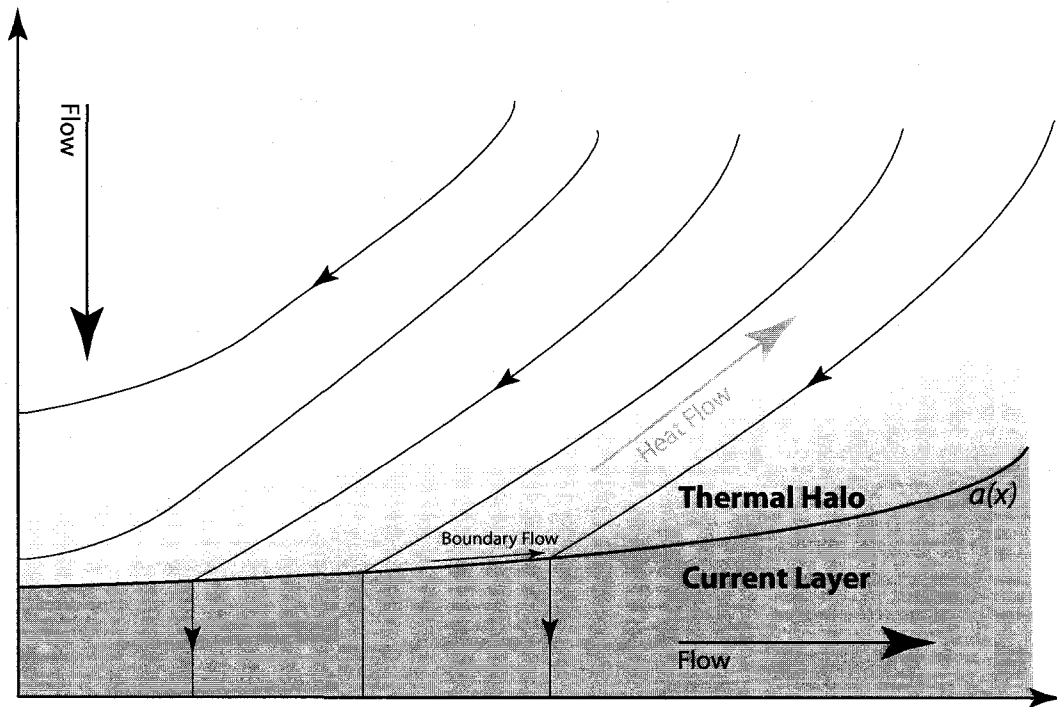
Figure 4-4: Schematic of the configuration of the current layer and thermal halo in this reformulation of the Somov-Titov system including thermal conduction. The addition of conduction creates flow and variation in the magnetic field along the boundary at $a(x)$ which are calculated using a modified version of the shock properties determined by Xu & Forbes (1992).

Finally, the current sheets in the cases considered by Somov & Oreshina appear to be exceptionally thin—on the order of a few meters thick. These values are not consistent with observations (Ciaravella et al., 2002) or models (Yokoyama & Shibata, 2001) of coronal current sheets. Thus for a reasonable analysis of the effects of thermal conduction on current sheets in the corona, we must reconsider the problem with appropriate solar values. Thus there are several reasons why our approach to this problem represents an improvement over the existing solution by Somov & Oreshina.

Because we wish to compare directly with the results of Yokoyama & Shibata, we will use the classical formula for our heat flux term. That is,

$$\mathcal{L} = -\kappa \nabla T, \tag{4.1}$$

where κ is the thermal conduction tensor, $\mathcal{L}$ is the energy loss function (see the full MHD energy equation, 2.3), and T is the temperature. In this case, we assume that strong magnetic fields are present, and therefore conduction occurs only along magnetic field lines; no conduction perpendicular to the field is allowed. Because we have already assumed that pressure and density are essentially constant in the y-direction inside the current layer, we must conclude temperature is also constant (in y) in the current layer. Therefore, all of the conduction in our model takes place in the halo region that connects the main outflow jet to the chromosphere. For simplicity, we assume that the field is connected directly to a thermal sink at temperature T_0 at some distance L_c, which represents the distance from the current sheet to the chromosphere. Therefore, we can estimate the temperature gradient in the halo region as,

$$\nabla T \approx \frac{T - T_0}{L_c}.$$

To obtain a better estimate of the actual temperature gradients in the external region requires a full 2D model of the entire flare loop-chromosphere system. Such a model is beyond the scope of our analysis here, which is focused on the current layer

93

region. Thus the estimated energy lost to thermal conduction is

$$\mathcal{L} = \lambda T^{5/2} \nabla T \tan \theta$$

$$\mathcal{L} = \lambda \frac{2}{7} \nabla T^{7/2} \tan \theta$$

$$\mathcal{L} \approx \lambda \frac{2}{7} \frac{\left(T^{7/2} - T^{7/2}_{sink} \right)}{L_c} \frac{\langle B_y \rangle}{B_{xa}},$$

where θ is the angle between the magnetic field and current layer (and thus the tangent term can be rewritten as above) and λ is a constant, based on the Spitzer formula (Priest, 1982), so

$$\lambda = 1.8 \times 10^{-10} \frac{1}{\ln \Lambda} \mathrm{W\,m^{-1}K^{-1}}.$$

We can then rewrite the conduction term in our normalized units,

$$\mathcal{L} = \lambda^* \left(\langle T \rangle^{7/2} - T^{7/2}_{sink} \right) \frac{\langle B_y \rangle}{B_{xa}}. \tag{4.2}$$

where, λ^* represents the *normalized* thermal conduction coefficient, into which we have absorbed all the constants in the equation, and is given by

$$\lambda^* = \frac{2}{7} \frac{\lambda}{L_c} \frac{T_0^{7/2}}{\rho_0 V_{A0}^3},$$

where the additional terms T_0, ρ_0, and V_{A0} are included to ensure proper normalization. Respectively these parameters represent global temperature, density, and Alfvén speed, measured upstream of the current layer at $x = 0$.

The dimensionless parameter λ^* is the ratio of the energy loss due to thermal conduction to the energy input by Poynting flux carried at the Alfvén speed into the current layer. Here λ^* must be in the range of approximately $0 \leq \lambda^* \leq 1$. (In fact, it is possible to choose parameters such that $\lambda^* > 1$, but because the sheet cannot cool beyond the background temperature, any such choice returns the same solution as when $\lambda^* = 1$.) The ratio $\langle B_y \rangle / B_{xa}$ is equal to the tangent of the angle field lines make with the current layer boundary, which appears as a consequence of the tensor product in the general form of $\mathcal{L}$.

4.1.1 Equations for Reconnection Jet within a Thermal Halo

The main consequence of adding thermal conduction to our model is that heat can now flow out of the central current layer and into the halo region. In order to model the transition from the jet to the halo, we need to model the interface between the two. In general this is a very complex problem, but the problem is considerably simplified when slow-mode shocks are present. The structure of slow-mode shocks in the presence of thermal conduction has been previously considered by Xu & Forbes (1992). They obtained exact solutions for the structure of the slow-mode shocks in the presence of both conduction and radiation. However, they assumed that the net loss was due to radiation rather than thermal conduction. They did not include the effect of energy lost by conduction to the chromosphere. Here we re-work their analysis to replace the effect of loss due to radiation with the effect of loss due to conduction.

The addition of thermal conduction modifies the boundary values upstream of the shock, so that V_{xa} and B_{ya} are no longer zero. Thermal conduction raises the temperature of plasma immediately upstream of the slow shock so the shocks become isothermal. Xu & Forbes give the relationships for the shock transition in the presence of an energy loss. These relations are:

$$B_{xa} = B_{xu}\sqrt{\frac{3}{5} + \frac{2}{5}I_0},$$
(4.3)

$$V_{xa} = \langle V_x \rangle \left(1 - \frac{B_{xa}}{B_{xu}}\right),$$
(4.4)

$$V_{ya} = \frac{V_{xa}\langle B_y \rangle + M_a}{B_{xa}} + V_{xa}\frac{da}{dx},$$
(4.5)

$$\rho_a = \rho_u,$$
(4.6)

$$p_a = \frac{\beta}{2} + \frac{B_{xu}^2}{2} - \frac{B_{xa}^2}{2},$$
(4.7)

where the dimensionless parameter I_0 is the ratio of the energy loss rate to the incoming Poynting flux. In Xu & Forbes, I_0 included just the energy loss due to radiation.

Here, where the energy loss is thermal conduction, this ratio is

$$I_0 = -\frac{\lambda \left(\langle T \rangle^{7/2} - T_{sink}^{7/2} \right) \frac{\langle B_y \rangle}{B_{xa}}}{M_a B_{xa} + \frac{5}{2} p_a V_{ya}}.$$

(4.8)

Here we use $\langle T \rangle = (2 \langle p \rangle)/(\beta \langle \rho \rangle)$ and the isothermal condition that the temperature must be the same both inside and outside of the current layer. We assume that the background field is unchanged from before, but, because we now have expanded the shock into three regions (downstream, the jet boundary, and far upstream), in the equations above, in order to differentiate between quantities in the subshock region and those far upstream of the shock we use the subscript a—e.g. B_{xa}—to signify quantities at the jet boundary, a, and the subscript u—B_{xu}—to signify quanties far upstream. Thus we now refer to the background field as B_{xu}.

One key difference between our treatment of the slow-mode shock with heat conduction and the Xu & Forbes treatment is that the reconnection current layer is two-dimensional, while theirs was only one-dimensional. In the Xu & Forbes model, all heat that is conducted into the upstream region is necessarily convected back downstream (since, with only one dimension, there is no way to remove heat from the system entirely). In our model, heat can escape the system entirely if it flows to the heat sink before convection can carry it back into the current layer. Thus, there is always a net energy loss in our model.

To address the effect of the conductive heat loss, we have modified the Xu & Forbes equations by replacing the radiative heat loss with a conductive heat loss. Since the relative heat loss, I_0 depends on the properties of the jet, we need to iterate the combined system of slow-shock jump conditions and the Somov-Titov current layer. We first obtain an internal solution without including loss terms, then use this internal solution to find the appropriate shock jump conditions using equations 4.3 through 4.8. Next, we use these new jump conditions to obtain the boundary conditions for the Somov-Titov system. This procedure is repeated until the solution

converges.

Bearing in mind the iterative nature of the solution, and using the relationships above, we can rederive the MHD equations, now including thermal conduction. The Somov-Titov equations become:

$$-\rho_a V_{ya} + \rho V_{xa} \frac{da}{dx} = \frac{d}{dx}\left(a\rho \langle V_x \rangle\right), \tag{4.9}$$

for the continuity equation;

$$\frac{d}{dx}\left(a\rho \langle V_x \rangle^2\right) + V_{xa}\left(V_{ya} - \frac{da}{dx}V_{xa}\right) = -a\frac{d\langle p \rangle}{dx} + B_{xa} \langle B_y \rangle, \tag{4.10}$$

for the momentum equation; and

$$\frac{d}{dx}\left[a\left(\frac{5}{2}\langle p \rangle + \frac{\rho}{2}\langle V_x \rangle^2\right)\langle V_x \rangle\right] - \frac{da}{dx}\left(\frac{5}{2}p_a + \frac{\rho_a V_{xa}^2}{2}\right)V_{xa} +$$
$$+\lambda\left(\langle T \rangle^{7/2} - T_{sink}^{7/2}\right)\frac{\langle B_y \rangle}{B_{xa}} = -\frac{5}{2}p_a V_{ya} - M_a B_{xa}, \tag{4.11}$$

for the energy requation. Ohm's law is unchanged from its previous form.

This system of equations, including thermal conduction, is solved similarly to the system without thermal conduction described in chapter 2. We again obtain explicit analytic solutions to the equations at $x = 0$, which we use as the initial conditions for obtaining solutions numerically for the rest of the layer. However, in this case we must be cautious in our interpretation of the results for the diffusion region (the region where $x < \alpha$). Because the Xu & Forbes equations hold only for slow shocks, and the slow shocks are not present in the diffusion region, the solutions including the effects of these shocks are only meaningful in the region outside the diffusion region ($x > \alpha$). We also note that the Xu & Forbes jump conditions hold only in the case that the thickness of the subshock transition is much less than the halo thickness— that is, the subshock thickness must be much less than the total shock thickness. This is another reason why we cannot apply the Xu & Forbes results to the diffusion region.

4.1.2 Solutions

Because a principal effect of thermal conduction is to remove energy from the system, it is perhaps unsurprising that two of the most immediate consequences of adding thermal conduction to our equations are to cool the system and slow the outflow jet in the current layer. Figure 4-5 shows the effect of increasing thermal conduction given an otherwise identical set of input parameters. The top plot shows the speed of the outflow jet, $\langle V_x \rangle$, the middle plot shows the temperature, $\langle T \rangle$, of the current layer, while the bottom plot shows the density of the current layer, $\langle \rho \rangle$. In the case with no thermal conductions (red curves), the outflow jet nearly reaches the Alfvén speed at the end of the current layer. Additionally, because there is no cooling, the temperature of the current layer is relatively uniform and very high. In the case with modest thermal conduction (green curves), the outflow jet reachs only about 80% of the Alfvén speed, and, because some heat is carried out of the current layer by conduction, the temperature cools by nearly a factor of 10. In the case with maximum conduction (that is, the largest value of λ for which we can still obtain solutions), indicated by blue curves, the outflow jet reaches only about 50% of the Alfvén speed, and the temperature is almost uniformly equal to the background temperature. The dashed portion of the curves refer to the diffusion region solution, where the Xu & Forbes equations do not hold.

As we discussed in chapter 3, McKenzie & Hudson (1999) and McKenzie (2000) used Yohkoh to observe post-flare downflows above a reconnecting loop system in the corona and found that downflow speeds were only about half of the estimated local Alfvén speed. As a result, they concluded that the observed flows were considerably slower than those predicted by the standard reconnection models (i.e. Sweet-Parker or Petschek). However, the results shown in figure 4-5 suggest that even modest conduction may reduce the speed of the outflow jet by as much as a factor of two.
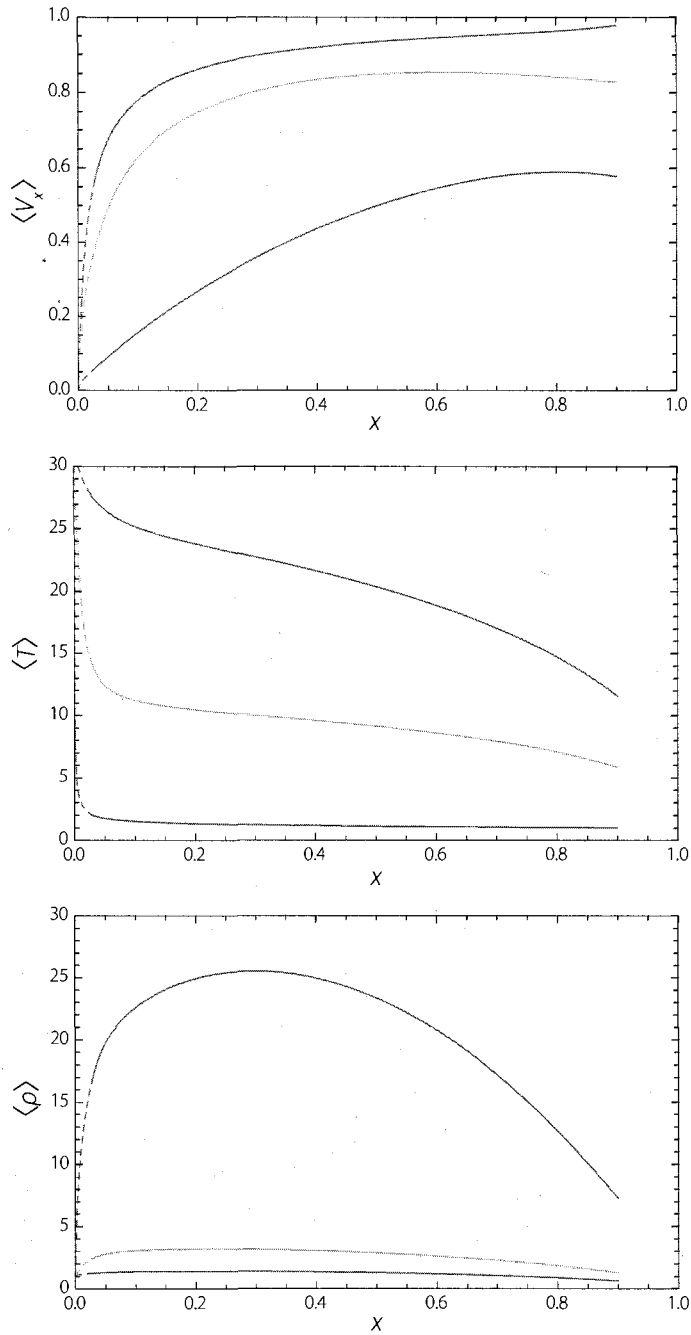
Figure 4-5: The effect of different thermal conductivity levels on the variation of outflow speed, temperature, and density with distance x along the current layer. The red curve corresponds to no conduction, the green to a modest amount of conduction, and the blue to very high conduction. The curves are dashed inside of the diffusion region, where the solutions including thermal conduction are not valid.

Thus we conclude that the downflows may in fact be reconnection outflow, and the relatively slow speed due to thermal conduction.

In chapter 3 we also discussed observations of current sheet temperatures and densities by Ciaravella et al. (2002), Raymond et al. (2003), and Ciaravella et al. (2006). They found that densities inside of the current layer were usually enhanced by about 2.5 times over background coronal densities, while our predicitions for densities without thermal conduction remained somewhat lower than that. The addition of thermal conduction, however, allows the plasma to cool substantially, which increases its density. Even modest amounts of conduction can increase the density to 5 times the background as seen in Figure 4-5. So a small amount of thermal conduction, that might only reduce the temperature of the plasma by a few percent, may account for the higher densities observed by these authors.

4.2   Comparison with Numerical Simulations

The numerical simulations by Yokoyama & Shibata were motivated by earlier predictions by Forbes et al. (1989) that the strong thermal conduction that exists in the corona would modify the standard Petschek configuration by replacing the slow MHD shocks with a combination of conduction fronts and isothermal slow-mode shocks. The basic idea was confirmed by Yokoyama & Shibata, but a detailed comparison between their simulation and the isothermal slow-mode jump conditions shows descrepancies on the order of a factor of two or so. This is because the jump relations of Xu & Forbes must be modified to include the energy lost by conduction of heat from the reconnection region to the chromosphere. Here we will see that this modification leads to good agreement between the modified Somov-Titov formalism and Yokoyama & Shibata's numerical simulations of reconnection including conduction.

In order to evaluate our model, we compared it to two numerical models by

Yokoyama & Shibata (1997, 2001). These two-dimensional models make use of a numerical code that includes nonlinear, anisotropic heat conduction. Unlike our steady-state model, these simulations are time-dependent, so our benchmarking comparison corresponds only to a snapshot of their model at some point in its evolution. These simulations do achieve quasi-steady configurations, but even in these cases there are low-level fluctuations.

Yokoyama & Shibata use a classical Spitzer-type conduction coefficient that is proportional to $T^{5/2}\nabla T$, so we have used the same form so as to facilitate a good comparison. In real flares the thermal conduction is likely to be anomalous because of the very high temperature of the flare plasma. Somov & Oreshina use a conduction coefficient proportional to $T^{3/2}$ and which is independent of the temperature gradient. Their model corresponds to the free escape of energetic electrons from the flare plasma. A noteworthy difference between the Somov & Oreshina model and the Yokoyama & Shibata simulation is the presence of a tangential field (B_x) inside the current layer. Because Somov & Oreshina assume that $\langle B_x \rangle$ is zero everywhere, the conductive loss goes to zero at their x-line. However, in the Yokoyama & Shibata model, heat flows not only out of the current layer and into the surrounding plasma, but also flows along field that exists in the diffusion region. Consequently, Somov & Oreshina predict very high temperatures in the diffusion region that simply do not occur in numerical simulations. If anything, the temperature in the diffusion region in the simulations are cooler than the rest of the layer. Thus it is clear that the Somov-Titov formalism can only be used to model the effects of thermal conduction outside the diffusion region, where normal field dominates any tangential field. In this region conduction in both models is predominantly out of the current layer (rather than along it).

In order to make the actual comparison to our results, we have estimated average

values of key parameters in the Yokoyama & Shibata model both inside the current layer and at the boundary in the thermal halo region. This estimation is done by visually inspecting plotted cross sections from the two Yokoyama & Shibata papers (see Figures 4-1, 4-2, and 4-3). Most of the small-scale variations seen in these plots are due to temperature fluctuations. Nonetheless, in most cases it is possible to estimate an average value, treating the fluctuations as a measure of the error in the estimate. These cross-sectional measurements are made well outside the diffusion region in both cases (in the location of the white line in Figure 4-1), where our analytic model should be valid.

We can see in Figures 4-1 and 4-2 that conduction has a significant effect on the results of the simulation, most obviously, broadening the heated region and increasing the uniformity (in temperature and other parameters) of the current layer. The expansion of the heated region occurs because heat flows out from the hot current layer and into the surrounding plasma, creating—as we have discussed above—a thermal halo. The increase in uniformity occurs because heat flows along lines of magnetic field faster than the plasma would otherwise naturally diffuse. Thus, without conduction, small regions of plasma can be heated to high temperatures, and there is no mechanism to cool them or spread the thermal energy into the surrounding plasma. With conduction, even if heating only occurs in a particular region, heat can quickly flow throughout the entire current layer and thermal halo, leading to an even distribution of temperature.

We compared our results to the Yokoyama & Shibata results by measuring plasma parameters inside the current layer and thermal halo and comparing the relative values of each. If our model works correctly, we would expect that comparisons of ratios of these values in both models would agree. The four tables that follow show input parameters and results from analyses with our model and the Yokoyama & Shibata

numerical models. Tables 4.1 and 4.3 show the input parameters used to match those in the 1997 and 2001 papers, respectively. Tables 4.2 and 4.4 show a comparison of ratios of values inside and outside the current sheet in the two models. Error in the measurements of the Yokoyama & Shibata results arises from both the time-varying nature of their solution (which leads to many small fluctuations throught the current layer that make it impossible to assign an exact average value at any location) and the fact that values are read off of a graph with limited resolution. Fluctuations throughout the solution, however, account for the bulk of the error, which was estimated by eye.

Note that for ratios of the form

$$z = x/y,$$

we use the formula for propagation of standard deviations to calculate error, given in Parratt (1961) by:

$$\Delta z = \sqrt{\frac{\Delta x^2}{y^2} + \frac{\Delta y^2 x^2}{y^4}}.$$

Because of the differences between our own, essentially 1-dimensional model, and the Yokoyama & Shibata 2-dimensional, numerical model, we would never expect exact agreement between the two models. However, as we can clearly see from the tables, there is systematic agreement between our model and the more complex numerical model. In general, the ratios measured in the Yokoyama & Shibata model were within about 20-30% of the same ratios measured in our model, although there are a few cases where there are larger differences. The most notable of these is the velocity ratio in the 1997 paper, which, because of rapid fluctuations in the thermal halo region, was difficult to measure. In this case, however, measurements of the same ratio in the 2001 paper confirm that our results appear to agree. Additionally, Yokoyama & Shibata do not include cross sectional plots of magnetic field in their 2001 paper, thus these ratios are omitted from our comparison.

Physical Parameter	Symbol	Value
Cooling Length Scale	L_c	6×10^8 m
Particle Number Density	n_0	1×10^{15} m^{-3}
Background Magnetic Field	B_0	21.7 gauss
Background Temperature	T_0	4×10^6 K
Plasma β	β	0.03
Conduction Coefficient	$\lambda = \frac{T_0^{7/2}}{\rho_0 V_{A0}^3 L_c} \frac{2}{7}$	3.4×10^{-4}
Alfvén Mach Number	M_A	0.1
Lundquist Number	L_u	3.6×10^3

Table 4.1: Input Parameters for comparison with Yokoyama & Shibata (1997) results.

Physical Parameter	Symbol	Y&S '97 Model	Theory
Density Ratio	$\rho_a/ <\rho>$	0.20 ± 0.04	0.34
Pressure Ratio	$p_a/ <p>$	0.20 ± 0.02	0.30
Velocity Ratio	$V_{xa}/ <V_x>$	0 ± 0.2	0.15
Mag. Field (x-direction) Ratio	B_{xa}/B_0	0.88 ± 0.04	0.85
Mag. Field (y-direction) Ratio	$B_{ya}/ <B_y>$	1.10 ± 0.07	1.4

Table 4.2: Comparison of ratios calculated from Yokoyama & Shibata (1997) and our 2D model.

Physical Parameter	Symbol	Value
Cooling Length Scale	L_c	6×10^7 m
Particle Number Density	n_0	1×10^{15} m^{-3}
Background Magnetic Field	B_0	5.9 gauss
Background Temperature	T_0	2×10^6 K
Plasma β	β	0.20
Conduction Coefficient	$\lambda = \frac{T_0^{7/2}}{\rho_0 V_{A0}^3 L_c} \frac{2}{7}$	0.015
Alfvén Mach Number	M_A	0.1
Lundquist Number	L_u	1×10^4

Table 4.3: Input parameters for comparison with Yokoyama & Shibata (2001) results.

Physical Parameter	Symbol	Y&S '01 Model	Theory
Density Ratio	$\rho_a/<\rho>$	0.48 ± 0.03	0.52
Pressure Ratio	$p_a/<p>$	0.47 ± 0.02	0.45
Velocity Ratio	$V_{xa}/<V_x>$	0.11 ± 0.01	0.18
Mag. Field (x-direction) Ratio	B_{xa}/B_0	—	0.82
Mag. Field (y-direction) Ratio	$B_{ya}/<B_y>$	—	1.4

Table 4.4: Comparison of ratios calculated from Yokoyama & Shibata (2001) and our 2D model.

It is important to note that, while both models treat the shock and thermal dynamics similarly, there are a few major differences. Most obviously, Yokoyama & Shibata include two-dimensional effects in their model that our own cannot accomodate. It seems likely that two-dimensional effects account for the bulk of the difference between the two models. Other factors which may contribute to the differences are the numerical noise in the Yokoyama & Shibata model, as well as the presence of non-steady-state features.

4.3   Fast Shock Formation in the Presence of Conduction

During flares, hard X-ray emission is often observed co-located with the tops of the post-flare loop arcade (Sui et al., 2002). These x-ray emissions are often linked to Type II radio bursts, and may be caused by particle acceleration due to fast-mode shock waves that form in the reconnection outflow jets above the post-flare loop systems (Tsuneta & Naito, 1998; Mann et al., 2001; Mann & Klassen, 2005). Since the strength of these shocks is related to the amount of particle acceleration, we investigated the role that thermal conduction plays in generating these shocks, and conduction's effect on the shock's strength. (For a complete summary of fast shock formation in reconnection jets see Forbes, 1986.)

In our normalized units, we can calculate the fast-mode Mach number of the outflow jet using the formula

$$M_{FM} = \frac{\langle V_x \rangle}{\sqrt{\frac{\langle B_y \rangle^2}{\langle \rho \rangle} + \frac{5p}{3\langle \rho \rangle}}}.$$ (4.12)

Since the highest value of M_{FM} occurs near the tip of the current layer, we measure the fast-mode Mach number at the point $1 - M_A$. Beyond this location our assumptions break down as B_{xa} approaches zero at the tip of the Syrovatskii current layer (see chapter 2). Measuring at this point generally allows us to calculate the Mach number
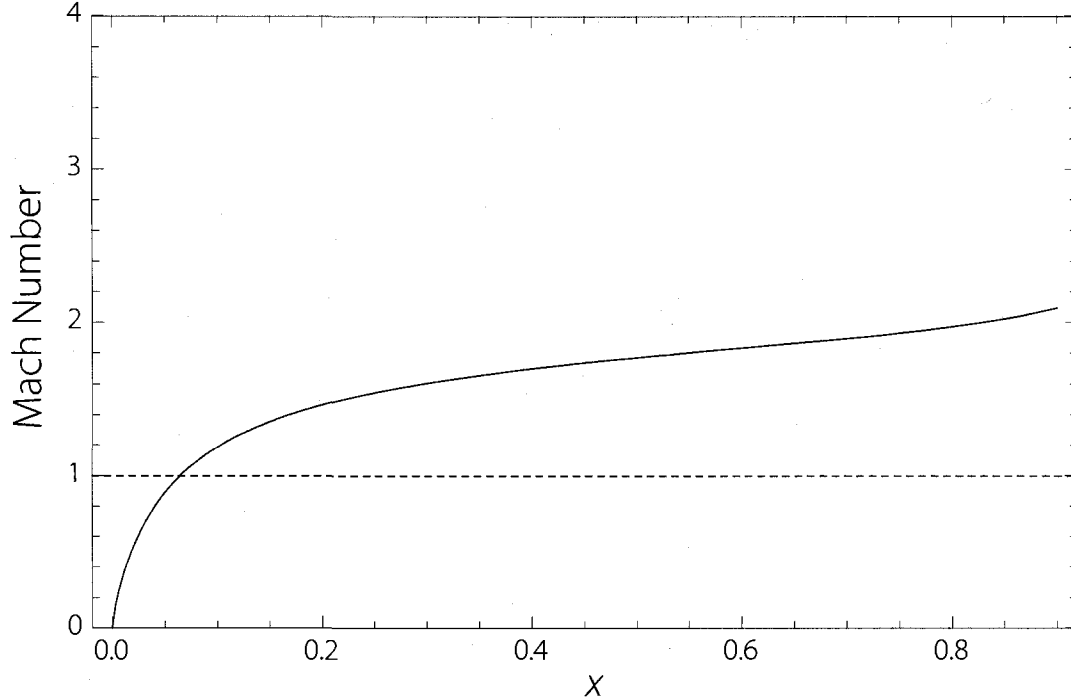
Figure 4-6: An example of the fast-mode Mach number shown as a function of distance along the current layer, x, plotted for the case corresponding to the Yokoyama & Shibata (1997) input parameters that appear in table 4.1. The dashed-line corresponds to a Mach number of 1, and shows where the flow becomes super-magnetosonic.

for the fastest flow, and therefore gives the maximum Mach number for a given set of parameters. Figure 4-6 shows an example of the behavior of fast-mode Mach number as a function of the distance along the current layer. The Mach number is generally low in the diffusion region, then rises rapidly in the shocks region as the temperature cools and the flow reaches its maximum speed.

Based on thermal conduction's effect on outflow jet speed, one might expect that increasing thermal conduction would simply reduce the outflow jet's fast-mode Mach number, and thus the strength of the shock in the outflow jet. However, the Mach number depends on more than just the outflow speed, it also depends on the fast-mode wave speed. Increased thermal conduction actually acts to cool the jet, which

in turn reduces the local sound speed. This dramatically increases the fast-mode wave speed in the jet, since the contribution from the weak magnetic field in the jet is negligible. To show this effect, we plot the fast-mode Mach number as a function of conduction coefficient and plasma β (Figures 4-7 and 4-8, respectively). For a given plasma β (denoted by color in both figures), as conduction coefficient rises, the Mach number increases to a point, then decreases slightly. For any conduction coefficient greater than one, the Mach number remains constant. Figure 4-9 is a surface plot that shows the effect of both conduction coefficient and plasma β simultaneously.

The normalized conduction coefficient represents the ratio of energy flow due to thermal conduction to free energy available; a conduction coefficient of one represents a case where all the free energy in a system is being removed by heat flow. As we noted before, a conduction coefficient greater than one does not remove any more energy from the system, so increasing the conduction coefficient beyond one has no effect on the fast mode Mach number.

As the conduction coefficient increases, the temperature of the current layer decreases (see section 4.1.2), and, correspondingly, so does the sound speed. If the sound speed decreases while the outflow speed stays relatively constant, the fast-mode Mach number increases. However, as the conduction coefficient approaches one, the temperature of the current layer approaches equilibrium with the outside, and thus the sound speed reaches a minimum. Meanwhile, as energy is lost to thermal conduction, the jet also slows. If the sound speed remains relatively constant while the outflow jet slows, the fast-mode Mach number is reduced. Thus we see—as in Figure 4-7— that the maximum Mach number for a given plasma β occurs when the conduction coefficient is slightly less than one.

Figure 4-8 shows how varying the plasma β effects the fast-mode Mach number of the outflow jet. For each β, there is a family of possible solutions, depending on the
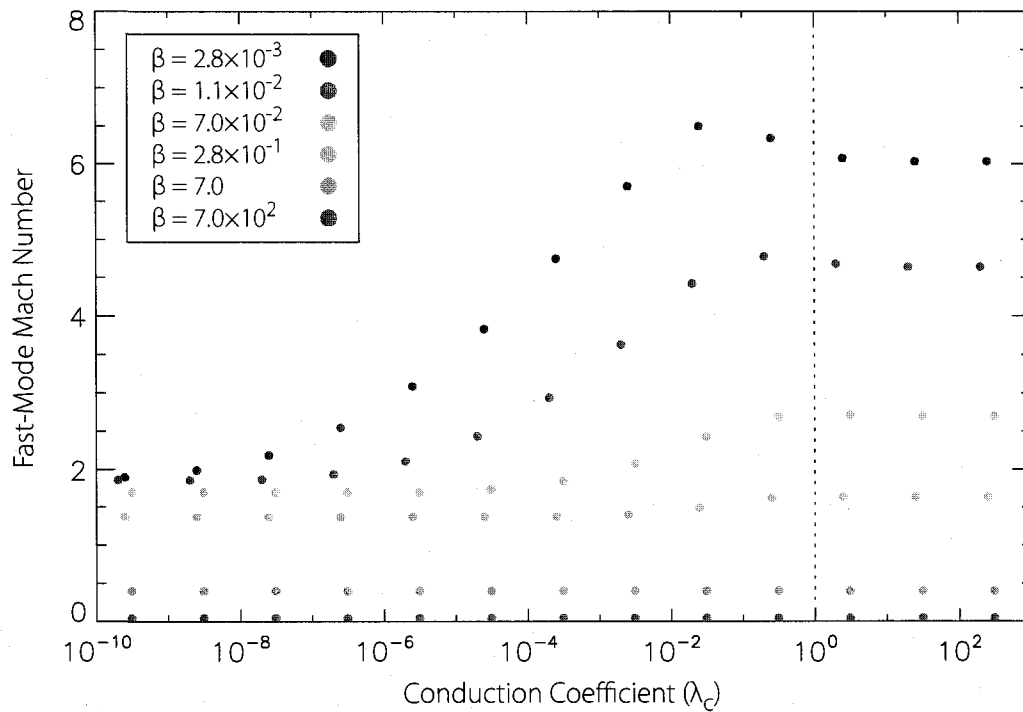
Figure 4-7: The effect of conduction coefficient on fast-mode Mach number. The colored dots correspond to different plasma β cases, which are identified in the inset in the upper left. The dashed vertical line shows where the effect of increasing conduction ceases to have an effect. (Once the plasma is cooled to the background temperature, it cannot cool any more and conduction switches off.) The peak in Mach number occurs when conduction is slightly less than maximum.
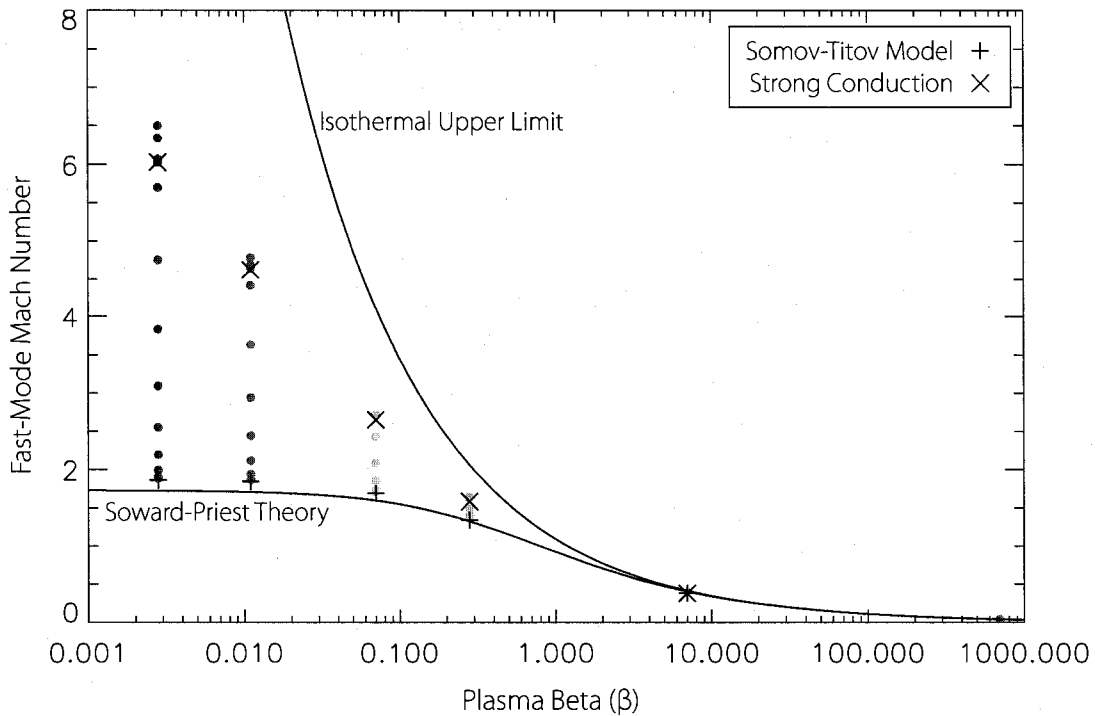
Figure 4-8: The effect of plasma β on fast-mode Mach number for the same individual cases as shown in figure 4-7. Cases with low Mach number correspond to low conduction, while cases with large Mach numbers correspond to high conduction. The + signs indicate Mach numbers calculated for the Somov-Titov case with no conduction, and the × signs indicate a Somov-Titov-like case where the energy equation is replaced by the assumption that the plasma in the sheet has cooled to the background temperature. The two curves refer to the theoretical limits for Mach numbers: the lower one is the Soward & Priest (1982) calculation of Mach number without conduction, while the upper curve is the Mach number for a flow at the Alfvén speed in an isothermal plasma.
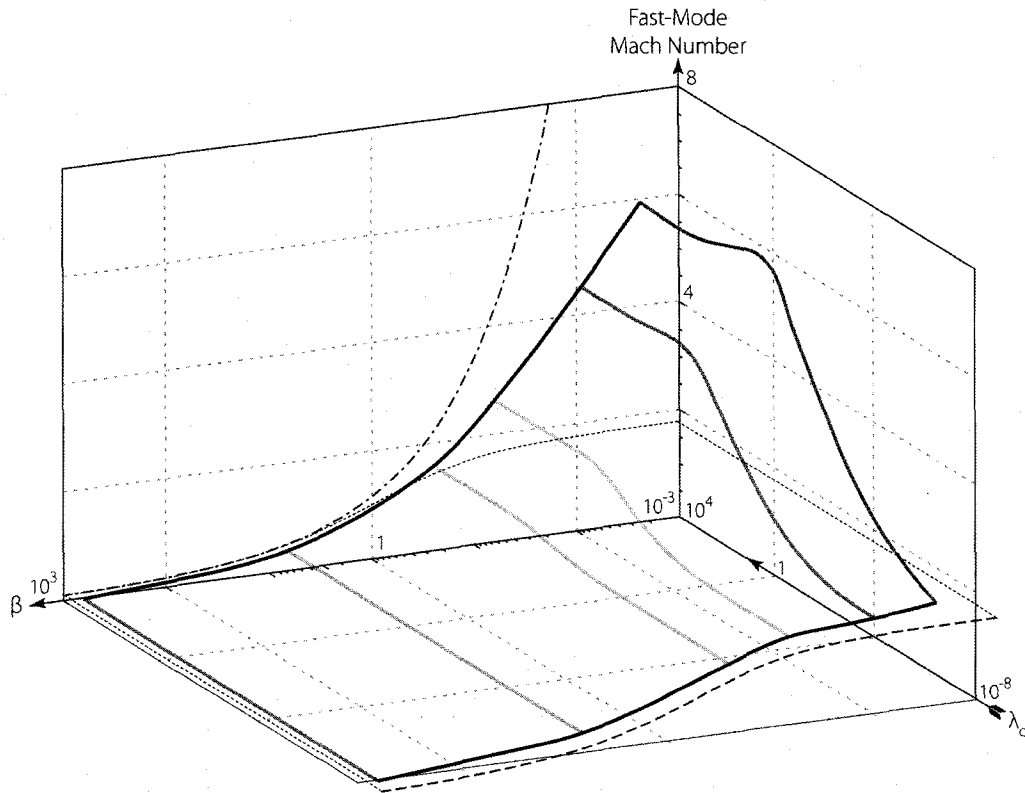
Figure 4-9: The results shown in figures 4-7 and 4-8 shown as a 3D surface plot. The colored lines refer to the respective β cases described in figure 4-7. The Soward-Priest lower limit is represented by a surface bounded by a dashed line, while the isothermal upper limit is represented by a dashed-dotted line.

choice of conduction coefficient. We know from Figure 4-7 that higher Mach numbers occur when the conduction coefficient becomes large, while low Mach numbers occur when the plasma β is low. Figure 4-8 also shows the Mach number for several special cases. The lower curve refers to the Mach number (Forbes, 1986) that results from the use of the Soward & Priest (1982) reconnection theory. This theory is a compressible Petschek-type reconnection model with no thermal conduction. The upper curve gives the isothermal upper limit on Mach number—that is, the highest possible Mach number, assuming outflow at exactly the Alfvén speed. The + signs refer to Mach numbers calculated for the Somov-Titov theory with no thermal conduction for a given plasma β, while the × signs refer to Mach numbers for outflow for a modified Somov-Titov theory where the energy equation is modified to force the current layer and surrounding plasma to be entirely isothermal. We note that the results for the Somov-Titov model correspond closely to our results for zero conduction, while the strong-conduction Somov-Titov case correspond closely to our own isothermal model. Further, no result approaches the upper limit (for small β). This is because conduction removes energy from the jet, preventing it from reaching the Alfvén speed.

The excellent agreement between our results for $\lambda_c = 0$ and those of Soward & Priest (1982) provide confirmation of the overall validity of the Somov-Titov formalism for Petschek-type reconnection. The Soward & Priest theory uses a completely different mathematical approach than that of Somov & Titov. It is a rigorous two-dimensional analysis of the compressible MHD equations and does not make use of averaging of any kind. It only assumes, as we have here (and as Petschek implicitly assumed) that the length of the diffusion region is a free parameter.

CHAPTER 5

CONCLUSIONS & FUTURE

RESEARCH

In this dissertation we have developed an improved analytical model for the reconnection process in eruptive flares. Our model extends the formalism developed by Somov (1992) and Somov et al. (1987) that averages quantities over the thickness of the reconnection outflow layer, a procedure that is very similar to the standard treatment for 1D nozzle flow. We have extended the Somov-Titov formalism to the asymmetric reconnection process that occurs in flares and we have also used it to analyze the effects of thermal conduction on the reconnection region. At the conclusion of this work, it is appropriate to ask the question: what have we learned about reconnection and solar eruptions from this model and what are its prospects for future research? Thus, in the sections that follow, we will attempt to highlight some of the important conclusions we can draw from our work and point out some of the interesting research questions that remain unanswered.

5.1 Conclusions

Before using the Somov-Titov formalism, we first undertook a thorough analysis of it and the assumptions on which it is based, including a determination of the strengths and weaknesses of the system. Since little documentation about how Somov & Titov

obtained their equations exists—the only papers, to our knowledge, about this system (Somov et al., 1987; Somov, 1992) provide almost no comment on the origin of the equations—it was necessary to completely rederive the system from first principles.

This analysis revealed three very important assumptions that restrict the family of possible reconnection solutions that the model predicts. The first is that the approach assumes there is no significant tangential flow outside the current layer, which eliminates a large class of possible reconnection type solutions (e.g. stagnation-point-flow type solutions). The second assumption, that the background magnetic field is Syrovatskii-like, actually represents an improvement to the assumptions made in other Petschek-like models. The third major assumption is that there is no significant tangential magnetic field inside the current layer.

Like Petschek, Somov & Titov obtain a family of solutions whose reconnection rate ranges from slow to fast. The solution with the slowest rate corresponds to the Sweet-Parker solution, with a diffusion region that is nearly the same length as the current layer. The solution with the fastest rate corresponds to the Petschek solution, with a diffusion region whose length equals the thickness of the current layer.

Our analysis shows that the Somov-Titov system of equations is insufficient to provide a unique solution because the number of equations is one less than the number of unknowns. Thus their formalism fails to predict the reconnection rate. It only provides an accurate description of the reconnection process if the reconnection rate (or, equivalently, the length of the diffusion region) is given. A long standing question concerning Petschek's solution is why simulations such as those of Yan et al. (1992); Baty et al. (2006) and others have found nonuniform resistivity to be a prerequisite for the production of Petschek-like results. We found that even when a nonuniform resistivity is explicitly added to the Somov-Titov system, the reconnection rate still remains undetermined. However, this addition does provide some insight as to why

nonuniformity leads to a Petschek-like solution. The nonuniformity can restrict the range of α to small values (that is, the Petschek range).

Another result of our investigation of the Somov & Titov formalism is that their assumption that the tangential field component in the current layer is negligible everywhere is not valid in the diffusion region. Strictly speaking, this assumption is only valid in the slow-shock region. Nevertheless, we find, after recalculating their solution in the diffusion region with a model tangential field that is not zero, that the qualitive character of the solution remains the same, but that their predictions for the properties of the diffusion region are changed.

That said, the assumption that the tangential magnetic field is zero is a significant limitation of the Somov-Titov model, especially in the case where the diffusion region (where this assumption is at its worst) is large. The need for this assumption arises from the fact that the number of averaged equations is insufficient to solve for all of the unknowns in the system. Thus, without an additional equation, it is impossible to improve the solution and remove this limitation.

Our principal goal here has been to apply our new understanding of the Somov-Titov formalism to improving analytical models of eruptive flares by Lin & Forbes (2000) and Reeves & Forbes (2005). We accomplished this in two ways. First, we applied the formalism to the asymmetric background field produced by these models, and second, we used it to analyze the effect of field-aligned thermal conduction. We use our improved model to explain several features that have been previously seen in observations and simulations of CMEs and flares. Additionally, we make several predictions about the nature of the current sheet that can be tested by future observations and simulations.

One of the most significant of these predictions is the location of the x-line within a reconnecting current layer. We find that the x-line will occur at the location where

the external magnetic field reaches a maximum, a point we refer to as the pinch point. Using the same magnetic field as in CME models by Lin & Forbes (2000) and Reeves & Forbes (2005) we find that during most of the evolution of a CME, this location is very near the lower tip of the current sheet.

The determination of this location within the current sheet (or layer) has several important implications for both observations and theory. First, we find that the amount of incoming Poynting flux that enters the downward directed jet is, for the majority of the development of the CME only a small fraction of the total incoming flux. Thus significantly less energy enters the downward jet than was supposed by Reeves & Forbes. Second, the lower location corresponds to a higher effective reconnection rate for a given inflow Alfvén Mach number. Thus we conclude that Reeves & Forbes (2005) over-estimated the inflow speed in their predictions; improved values give better agreement with observations by Yokoyama & Shibata (2001). Finally, the lower x-line location may be observable with X-ray and EUV telescopes, which have limited fields of view and cannot observe features that are very high in the corona. Direct observations of the reconnection outflow in flares would constitute a major confirmation of the correctness of the flare reconnection model. It would also greatly help in determining how the reconnection works in flares.

In addition to the observational predictions, we show that in the presence of a highly asymmetric background field, it is no longer possible to recover a simple Sweet-Parker-like solution. This is because the critical α, which produces a Sweet-Parker solution, depends on the background field, which is not the same in the upward jet as it is in the downward jet. Thus when we choose α to produce a Sweet-Parker-like solution in one jet, we generally get either Petschek-like behavior or the formation of magnetic islands in the other. It is possible to obtain a Sweet-Parker solution in the upper jet by using a sufficiently large value of α. However, when this is done,

116

the field structure in the lower jet no longer resembles a standard Sweet-Parker-like solution. An island-like structure occurs which may be unstable or may indicate the existence of a more complex current structure.

The addition of thermal conduction to the model also has significant effects on the properties of the outflow jets. Most notably, conduction leads to an increase in the temperature of the plasma that surrounds the current layer, a region we refer to as the thermal halo. In order to model the isothermal slow-mode jump conditions we apply work on the structure of slow-mode shocks by Xu & Forbes (1992) to the Somov-Titov formalism. The addition of this shock model allows us to relax the Somov-Titov assumptions at the shock boundaries and determine the behavior of the plasma in the thermal halo. The existence of such a halo region was predicted by Forbes et al. (1989) and confirmed by numerical simulations by Yokoyama & Shibata (1997, 2001). Our analysis shows good agreement with the Yokoyama & Shibata (1997, 2001) result provided that the isothermal slow-mode jump conditions are modified to include the effect of the conductive heat loss.

We also find that thermal conduction produces several effects that are important for the interpretation of observations. First, strong conduction reduces the outflow speed significantly, by as much as a factor of two, in some cases. This result may explain the observations of unexpectedly slow supra-arcade downflows by McKenzie & Hudson (1999) and McKenzie (2000). These flows are thought to be produced by reconnection, but they were found to have speeds only about half as fast as the local Alfvén speed. Standard reconnection models predict that such jets should have velocities near the local Alfvén speed. However, our thermal conduction results suggest that the slower observed flow velocities may be due to the effect of thermal conduction. Thermal conduction drains energy out of the jet so there is less magnetic energy available to accelerate the flow. Second, observations by Ciaravella et al. (2002), Ray-

mond et al. (2003), and Ciaravella et al. (2006) showed that densities inside of the flare/CME current layer are usually enhanced about 2.5 times over background densities. We find that, the addition of thermal conduction, leads to a similar increase in the density of the current layer over the background.

Third, we find that thermal conduction plays an important role in determining the fast-mode Mach number (and therefore the shock strength) of the outflow jet. Previous analyses (Soward & Priest, 1977) that did not consider thermal conduction predict much weaker shocks with Mach numbers from 1.5 to 2.0. These weak shocks are unlikely to produce the energetic particle acceleration that is thought to be responsible for the appearance of hard X-ray sources observed near post-flare loop arcades (Tsuneta & Naito, 1998). Here we find that for small β solutions, thermal conduction can produce Mach numbers as high as 7, a considerably higher prediction than those of non-conductive models.

5.2 Future Research

Full reconnection solutions like Petschek's provide a prescription for how the field and flow vary in the region upstream of the current layer. The famous logarithmic scale of Petschek's reconnection rate is, in fact, due to the logarithmic variation of the magnetic field in this region. Thus one improvement that could be made to the Somov-Titov formalism would be to extend the solution to the external region as well. In fact, Somov (1992) offers a method by which this can be done. The combined solution for the external and internal regions requires an iterative approach, where we obtain an internal solution using the Syrovatskii background field, then calculate a more accurate external field using the method described by Somov (1992). This improved field can be used to produce a refinement of order $\approx M_A$ in the internal solution.

It is also worthwhile to note that the Syrovatskii field, and the similar asymmetric field used in chapter 3, are not the only possible background configurations for which this model may be useful. Other phenomena may lead to other field configurations in which the Somov-Titov system may prove useful. For example, Tur & Priest (1976) describe current sheets that form as the result of magnetic flux emergence from below the photosphere into different overlying magnetic fields. While the background fields in these cases differ from those explored in this dissertation, a version of the Somov-Titov model with these new field configurations could provide insight into the process and consequences of flux emergence for the corona.

It would be especially useful to compare our model to additional simulations beyond those of Yokoyama & Shibata (see chapter 4). This would be useful both in benchmarking our own work and testing the predictions we have made concerning the position of the x-line, the effect of the asymmetric background field on the behavior of the internal solution, and the relative speed and density of the upward and downward directed jets. A simulation with field aligned conduction could also test our predictions concerning the fast-mode Mach numbers of the outflow jets. Because our model is analytical, it could also be used to provide insight into otherwise unexplained behavior occuring in complex simulations.

Finally, we can expand the work using the Reeves & Forbes flare model discussed in chapter 3. For example, we can calculate both the the full evolution of the outflow jet and postflare loop system in time. Reeves & Forbes (2005) studied the evolution of the postflare loop system in time, but did not model the dynamics of the current layer. Our improvements in the energy calculations of Reeves & Forbes, the addition of a model for the evolution of the current layer and outflow jets, as well as the availability of a next-generation loop cooling model (Klimchuk et al., 2007) could be used to produce a useful tool for the interpretation of observations of events like the

21 April 2002 X-flare (Gallagher et al., 2002). Improvements could also be made in the Reeves & Forbes model's reconnection rate estimates. Finally, this improved model could be used as a predictive tool to help choose passbands and pointings for best observing flares using XRT.

In addition to those making use of the Reeves & Forbes model, there are several other observational tests of the predictions made by this model that could be carried out as solar activity increases over the next several years using new space-based solar observatories such as *Hinode*. In particular, we have made several verifiable predictions about the appearance and dynamics of the current sheet during a flare that could be tested with X-ray and EUV observations.

First, we have predicted that the x-line that forms in a current sheet during a CME is likely to be low in the corona. Some observations of a CME-related flare by XRT have already shown evidence of accelerating flow with an origin low in the corona (McKenzie, 2008, private communication). Thus, as the rate and intensity of solar flares increases with the solar cycle over the next few years, it is likely that XRT could actually image the x-line. Additionally, the Sun Watcher using Active Pixel detectors (SWAP), an EUV telescope on the *PROBA2* mission, will have the ability to off-point from the Sun (Katsiyannis et al., 2005) by several solar radii. Thus there is a good chance to confirm this prediction with observations during the next few years.

We also have made several predictions about the structure of the current sheet and thermal halo that could be confirmed with observations by EIS, on *Hinode*. Spectroscopic observations across the current layer could reveal details of density and temperature flucuations, as well as some of the properties of the reconnection jet. Such observations could be especially useful in determining the role that thermal conduction plays during eruptions. If conduction is important, we expect to see a

current layer with relatively uniform temperature and density, while observations of strong variation in temperature and density structure would suggest that conduction is not strong during these events. Since conduction plays an apparently important role in determining the speed and Mach number of reconnection outflow jets in our model, such observations have important implications for the source of flows such as the SADs reported by McKenzie & Hudson. These observations could provide very important insights into the nature of the reconnection that drives solar flares and CMEs.

BIBLIOGRAPHY

Antiochos, S. K., DeVore, C. R., & Klimchuk, J. A. 1999, ApJ, 510, 485

Antiochos, S. K. & Sturrock, P. A. 1978, ApJ, 220, 1137

Asai, A., Shibata, K., Yokoyama, T., & Shimojo, M. 2004, in Astronomical Society of the Pacific Conference Series, Vol. 325, The Solar-B Mission and the Forefront of Solar Physics, ed. T. Sakurai & T. Sekii, 361–+

Baty, H., Priest, E. R., & Forbes, T. G. 2006, Physics of Plasmas, 13, 2312

Bhattacharjee, A. & Wang, X. 1991, ApJ, 372, 321

Biskamp, D. 2000, Cambridge monographs on plasma physics, Vol. 3, Magnetic Reconnection in Plasmas (Cambridge, UK: Cambridge University Press)

Canfield, R. C., Cheng, C.-C., Dere, K. P., Dulk, G. A., McLean, D. J., Robinson, Jr., R. D., Schmahl, E. J., & Schoolman, S. A. 1980, in Solar flares, p. 451 - 469, 451–469

Cargill, P. J., Mariska, J. T., & Antiochos, S. K. 1995, ApJ, 439, 1034

Carmichael, H. 1964, in The Physics of Solar Flares, ed. W. N. Hess, 451–+

Carrington, R. C. 1859, MNRAS, 20, 13

Chapman, S. & Ferraro, V. C. A. 1931, Terr. Mag. and Atmosph. Elec., 36, 171

Ciaravella, A., Raymond, J. C., Li, J., Reiser, P., Gardner, L. D., Ko, Y.-K., & Fineschi, S. 2002, ApJ, 575, 1116

Ciaravella, A., Raymond, J. C., & Lin, J. 2006, in COSPAR, Plenary Meeting, Vol. 36, 36th COSPAR Scientific Assembly, 2109–+

Clark, A. J. 1964, Physics of Fluids, 7, 1299

Cowling, T. G. 1953, Solar Electrodynamics (The Sun), 532–+

Craig, I. J. D., Fabling, R. B., Henton, S. M., & Rickard, G. J. 1995, ApJL, 455, L197+

D'Azambuja, L. 1955, Vistas in Astronomy, 1, 695

Deluca, E. E. 2007, in Astronomical Society of the Pacific Conference Series, Vol. 369, New Solar Physics with Solar-B Mission, ed. K. Shibata, S. Nagata, & T. Sakurai, 19–+

Demastus, H. L., Wagner, W. J., & Robinson, R. D. 1973, Sol. Phys., 31, 449

Dennis, B. R. & Zarro, D. M. 1993, Sol. Phys., 146, 177

Dodson, H. W. 1949, ApJ, 110, 382

Dryer, M. 1982, Space Science Reviews, 33, 233

Dungey, J. W. 1953, Phil. Mag., 44, 725

Emslie, A. G., Brown, J. C., & Machado, M. E. 1981, ApJ, 246, 337

Fletcher, L. & Martens, P. C. H. 1998, ApJ, 505, 418

Forbes, T. G. 1986, ApJ, 305, 553

Forbes, T. G. 1993, in Astronomical Society of the Pacific Conference Series, Vol. 46, IAU Colloq. 141: The Magnetic and Velocity Fields of Solar Active Regions, ed. H. Zirin, G. Ai, & H. Wang, 415–+

—. 2003, Advances in Space Research, 32, 1043

—. 2007, in Reconnection of Magnetic Fields: Magnetohydrodynamics and Collisionless Theory and Observations, ed. J. Birn & E. R. Priest (Cambridge, UK: Cambridge Univ. Press), 16–25

Forbes, T. G. & Acton, L. W. 1996, ApJ, 459, 330

Forbes, T. G. & Isenberg, P. A. 1991, ApJ, 373, 294

Forbes, T. G., Linker, J. A., Chen, J., Cid, C., Kóta, J., Lee, M. A., Mann, G., Mikić, Z., Potgieter, M. S., Schmidt, J. M., Siscoe, G. L., Vainio, R., Antiochos, S. K., & Riley, P. 2006, Space Science Reviews, 123, 251

Forbes, T. G., Malherbe, J. M., & Priest, E. R. 1989, Sol. Phys., 120, 285

Forbes, T. G. & Priest, E. R. 1987, Reviews of Geophysics, 25, 1583

—. 1995, ApJ, 446, 377

Gallagher, P. T., Dennis, B. R., Krucker, S., Schwartz, R. A., & Tolbert, A. K. 2002, Sol. Phys., 210, 341

Giovanelli, R. G. 1946, Nature, 158, 81

Gold, T. 1962, Space Science Reviews, 1, 100

Golub, L. & Pasachoff, J. M. 1997, The Solar Corona (Cambridge, UK: Cambridge University Press)

—. 2001, Nearest Star: The Surprising Science of our Sun (Cambridge, MA: Harvard University Press)

Gopalswamy, N., Yashiro, S., Liu, Y., Michalek, G., Vourlidas, A., Kaiser, M. L., & Howard, R. A. 2005a, Journal of Geophysical Research (Space Physics), 110, 9

Gopalswamy, N. et al. 2005b, in International Cosmic Ray Conference, Vol. 1, International Cosmic Ray Conference, 169–+

Gosling, J. T. 1993, J. Geophys. Res., 98

Gosling, J. T., Hildner, E., MacQueen, R. M., Munro, R. H., Poland, A. I., & Ross, C. L. 1974, J. Geophys. Res., 79, 4581

—. 1976, Sol. Phys., 48, 389

Green, R. M. 1965, in IAU Symposium, Vol. 22, Stellar and Solar Magnetic Fields, ed. T. Gold, 398–+

Hale, G. E. 1931, ApJ, 73, 379

Handy, B. N., Acton, L. W., Kankelborg, C. C., Wolfson, C. J., Akin, D. J., Bruner, M. E., Caravalho, R., Catura, R. C., Chevalier, R., Duncan, D. W., Edwards, C. G., Feinstein, C. N., Freeland, S. L., Friedlaender, F. M., Hoffmann, C. H., Hurlburt, N. E., Jurcevich, B. K., Katz, N. L., Kelly, G. A., Lemen, J. R., Levay, M., Lindgren, R. W., Mathur, D. P., Meyer, S. B., Morrison, S. J., Morrison, M. D., Nightingale, R. W., Pope, T. P., Rehse, R. A., Schrijver, C. J., Shine, R. A., Shing, L., Strong, K. T., Tarbell, T. D., Title, A. M., Torgerson, D. D., Golub, L., Bookbinder, J. A., Caldwell, D., Cheimets, P. N., Davis, W. N., Deluca, E. E., McMullen, R. A., Warren, H. P., Amato, D., Fisher, R., Maldonado, H., & Parkinson, C. 1999, Sol. Phys., 187, 229

Harra-Murnion, L. K., Schmieder, B., van Driel-Gesztelyi, L., Sato, J., Plunkett, S. P., Rudawy, P., Rompolt, B., Akioka, M., Sakao, T., & Ichimoto, K. 1998, A&A, 337, 911

Harrison, R. A. 1986, A&A, 162, 283

—. 1991, Advances in Space Research, 11, 25

Harrison, R. A., Hildner, E., Hundhausen, A. J., Sime, D. G., & Simnett, G. M. 1990, J. Geophys. Res., 95, 917

Harrison, R. A., Waggett, P. W., Bentley, R. D., Phillips, K. J. H., Bruner, M., Dryer, M., & Simnett, G. M. 1985, Sol. Phys., 97, 387

Hiei, E. & Hundhausen, A. J. 1996, in IAU Colloq. 153: Magnetodynamic Phenomena in the Solar Atmosphere - Prototypes of Stellar Magnetic Activity, ed. Y. Uchida, T. Kosugi, & H. S. Hudson, 125–+

Hildner, E., Gosling, J. T., MacQueen, R. M., Munro, R. H., Poland, A. I., & Ross, C. L. 1976, Sol. Phys., 48, 127

Hirayama, T. 1974, Sol. Phys., 34, 323

Hodgson, R. 1859, MNRAS, 20, 15

Howard, R. A., Sheeley, Jr., N. R., Michels, D. J., & Koomen, M. J. 1986, in Astrophysics and Space Science Library, Vol. 123, The Sun and the Heliosphere in Three Dimensions, ed. R. G. Marsden, 107–111

Hoyle, F. 1949, Some recent researches in solar physics. (Cambridge, UK: Cambridge University Press)

Isenberg, P. A., Forbes, T. G., & Demoulin, P. 1993, ApJ, 417, 368

Jing, J., Yurchyshyn, V. B., Yang, G., Xu, Y., & Wang, H. 2004, ApJ, 614, 1054

Kahler, S. W. 1992, ARAA, 30, 113

Kahler, S. W., Sheeley, Jr., N. R., & Liggett, M. 1989, ApJ, 344, 1026

Kan, J. R., Akasofu, S.-I., & Lee, L. C. 1983, Sol. Phys., 84, 153

Katsiyannis, A. C., Berghmans, D., Hochedez, J.-F., Nicula, B., Lawrence, G., Defise, J.-M., Ben-Moussa, A., Delouille, V., Dominique, M., Lecat, J.-H., Schmutz, W., Theissen, A., & Slemzin, V. 2005, in Presented at the Society of Photo-Optical Instrumentation Engineers (SPIE) Conference, Vol. 5901, Solar Physics and Space Weather Instrumentation. Edited by Fineschi, Silvano; Viereck, Rodney A. Proceedings of the SPIE, Volume 5901, pp. 236-243 (2005)., ed. J. M. Davis, E. A. West, R. L. Moore, G. A. Gary, K. Kobayashi, J. E. Oberright, D. C. Evans, H. J. Wood, J. L. R. Saba, & D. Alexander, 236–243

Kliem, B. & Török, T. 2006, Physical Review Letters, 96, 255002

Klimchuk, J. A. 2001, Space Weather (Geophysical Monograph 125), ed. P. Song, H. Singer, G. Siscoe (Washington: Am. Geophys. Un.), 143 (2001), 125, 143

Klimchuk, J. A., Patsourakos, S., & Cargill, P. J. 2007, ArXiv e-prints, 710

Kohl, J. L., Esser, R., Gardner, L. D., Habbal, S., Daigneau, P. S., Dennis, E. F., Nystrom, G. U., Panasyuk, A., Raymond, J. C., Smith, P. L., Strachan, L., van Ballegooijen, A. A., Noci, G., Fineschi, S., Romoli, M., Ciaravella, A., Modigliani, A., Huber, M. C. E., Antonucci, E., Benna, C., Giordano, S., Tondello, G., Nicolosi, P., Naletto, G., Pernechele, C., Spadaro, D., Poletto, G., Livi, S., von der Lühe, O., Geiss, J., Timothy, J. G., Gloeckler, G., Allegra, A., Basile, G., Brusa, R., Wood, B., Siegmund, O. H. W., Fowler, W., Fisher, R., & Jhabvala, M. 1995, Sol. Phys., 162, 313

Kopp, R. A. & Pneuman, G. W. 1976, Sol. Phys., 50, 85

Leipmann, H. W. & Roshko, A. 1957, Elements of Gas Dynamics (New York, NY: John Wiley and Sons)

Lin, J. 2001, PhD thesis, University of New Hampshire

—. 2002, Chinese Journal of Astronomy and Astrophysics, 2, 539

Lin, J. & Forbes, T. G. 2000, J. Geophys. Res., 105, 2375

Lin, R. P. & Hudson, H. S. 1976, Sol. Phys., 50, 153

Linker, J., Mikic, Z., Lionello, R., & Riley, P. 2003, Plasma Phys., 10, 1971

Linker, J. A., Lionello, R., Mikić, Z., & Amari, T. 2001, J. Geophys. Res., 106, 25165

Linker, J. A. & Mikic, Z. 1995, ApJL, 438, L45

Linker, J. A., van Hoven, G., & Schnack, D. D. 1990, J. Geophys. Res., 95, 4229

Litvinenko, Y. E., Forbes, T. G., & Priest, E. R. 1996, Sol. Phys., 167, 445

Low, B. C. 1996, Sol. Phys., 167, 217

MacNeice, P., Antiochos, S. K., Phillips, A., Spicer, D. S., DeVore, C. R., & Olson, K. 2004, ApJ, 614, 1028

MacQueen, R. M. & Fisher, R. R. 1983, Sol. Phys., 89, 89

Malville, J. M. & Moreton, G. E. 1963, PASP, 75, 176

Malyshkin, L. M., Linde, T., & Kulsrud, R. M. 2005, Physics of Plasmas, 12, 2902

Manheimer, W. M. 1977, Physics of Fluids, 20, 265

Manheimer, W. M. & Klein, H. H. 1975, Physics of Fluids, 18, 1299

Mann, G., Classen, H.-T., & Motschmann, U. 2001, J. Geophys. Res., 106, 25323

Mann, G. & Klassen, A. 2005, A&A, 441, 319

Martens, P. C. H. & Kuin, N. P. M. 1989, Sol. Phys., 122, 263

Martin, S. F. 1973, Sol. Phys., 31, 3

Martres, M. J., Michard, R., & Soru-Iscovici. 1966, Annales d'Astrophysique, 29, 249

Masuda, S., Kosugi, T., Hara, H., Tsuneta, S., & Ogawara, Y. 1994, Nature, 371, 495

McKenzie, D. E. 2000, Sol. Phys., 195, 381

McKenzie, D. E. & Hudson, H. S. 1999, ApJL, 519, L93

McKenzie, D. E., Savage, S., & Tolan, J. E. 2007, in Astronomical Society of the Pacific Conference Series, Vol. 369, New Solar Physics with Solar-B Mission, ed. K. Shibata, S. Nagata, & T. Sakurai, 489–+

Moon, Y.-J., Choe, G. S., Wang, H., Park, Y. D., Gopalswamy, N., Yang, G., & Yashiro, S. 2002, ApJ, 581, 694

Moore, R., McKenzie, D. L., Svestka, Z., Widing, K. G., Dere, K. P., Antiochos, S. K., Dodson-Prince, H. W., Hiei, E., Krall, K. R., & Krieger, A. S. 1980, in Skylab Solar Workshop II, ed. P. A. Sturrock, 341–409

Munro, R. H., Gosling, J. T., Hildner, E., MacQueen, R. M., Poland, A. I., & Ross, C. L. 1979, Sol. Phys., 61, 201

Neidig, D. F. & Cliver, E. W. 1983, Sol. Phys., 88, 275

Neupert, W. M. 1968, ApJL, 153, L59+

Newton, H. W. 1943, MNRAS, 103, 244

Oreshina, A. V. & Somov, B. V. 1997, A&A, 320, L53

—. 1998, A&A, 331, 1078

Parker, E. N. 1957, J. Geophys. Res., 62, 509

Parker, E. N. 1973, J. Plasma Phys., 9, 49

Parratt, L. G. 1961, Probability and Experimental Errors in Science (New York, NY: John Wiley and Sons)

Petschek, H. E. 1964, in The Physics of Solar Flares, ed. W. N. Hess, 425–+

Priest, E. & Forbes, T. 2000, Magnetic Reconnection (Cambridge, UK: Cambridge University Press)

Priest, E. R. 1982, Solar magneto-hydrodynamics (Dordrecht, Holland: D. Reidel Pub. Co.)

Priest, E. R. & Forbes, T. G. 1986, J. Geophys. Res., 91, 5579

Raymond, J. C., Ciaravella, A., Dobrzycka, D., Strachan, L., Ko, Y.-K., Uzzo, M., & Raouafi, N.-E. 2003, ApJ, 597, 1106

126

Reeves, K. K. 2006, PhD thesis, University of New Hampshire

Reeves, K. K. & Forbes, T. G. 2005, ApJ, 630, 1133

Reeves, K. K., Linker, J., Mikic, Z., & Forbes, T. G. 2008a, ApJ, in preparation.

Reeves, K. K., Seaton, D. B., & Forbes, T. G. 2008b, ApJ, 675, 868

Reeves, K. K., Warren, H. P., & Forbes, T. G. 2007, ApJ, 668, 1210

Roberts, P. H. 1967, An Introduction to Magnetohydrodynamics (New York, NY: American Elsevier Publishing)

Roussev, I. I., Forbes, T. G., Gombosi, T. I., Sokolov, I. V., DeZeeuw, D. L., & Birn, J. 2003, ApJL, 588, L45

Schreier, S. 1982, Compressible Flow (New York, NY: John Wiley and Sons)

Sen, H. K. & White, M. L. 1972, Sol. Phys., 23, 146

Servajean, R. & Olivieri, G. 1946, L'Astronomie, 60, 215

Sheeley, N. R., Walters, J. H., Wang, Y.-M., & Howard, R. A. 1999, J. Geophys. Res., 104, 24739

Sheeley, Jr., N. R., Bohlin, J. D., Brueckner, G. E., Purcell, J. D., Scherrer, V. E., Tousey, R., Smith, Jr., J. B., Speich, D. M., Tandberg-Hanssen, E., & Wilson, R. M. 1975, Sol. Phys., 45, 377

Sheeley, Jr., N. R., Howard, R. A., Koomen, M. J., & Michels, D. J. 1983, ApJ, 272, 349

Sheeley, Jr., N. R. & Wang, Y.-M. 2002, ApJ, 579, 874

—. 2007, ApJ, 655, 1142

Shivamoggi, B. K. 1985, Phys. Rep., 127, 99

Sittler, Jr., E. C. & Guhathakurta, M. 1999, ApJ, 523, 812

Somov, B. V. 1992, Astrophysics and Space Science Library, Vol. 172, Physical processes in solar flares (Dordrecht, Holland: Kluwer Academic Publishers), 65–+

Somov, B. V. & Oreshina, A. V. 2000, A&A, 354, 703

Somov, B. V., Titov, V. S., & Verneta, A. I. 1987, Itogi Nauki i Tekhniki Seriia Astronomiia, 34, 136

Sonnerup, B. U. O. 1970, J. Plasma Phys., 4, 161

Sonnerup, B. U. O. & Priest, E. R. 1975, Journal of Plasma Physics, 14, 283

Soward, A. M. & Priest, E. R. 1977, Royal Society of London Philosophical Transactions Series A, 284, 369

—. 1982, Journal of Plasma Physics, 28, 335

St. Cyr, O. C. & Webb, D. F. 1991, Sol. Phys., 136, 379

Starr, R., Heindl, W. A., Crannell, C. J., Thomas, R. J., Batchelor, D. A., & Magun, A. 1988, ApJ, 329, 967

Sterling, A. C. & Moore, R. L. 2005, ApJ, 630, 1148

Sturrock, P. A. 1968, in IAU Symposium, Vol. 35, Structure and Development of Solar Active Regions, ed. K. O. Kiepenheuer, 471–+

Sui, L., Holman, G. D., Dennis, B. R., Krucker, S., Schwartz, R. A., & Tolbert, K. 2002, Sol. Phys., 210, 245

Svestka, Z. F., Fontenla, J. M., Machado, M. E., Martin, S. F., & Neidig, D. F. 1987, Sol. Phys., 108, 237

Sweet, P. A. 1958, in IAU Symposium, Vol. 6, Electromagnetic Phenomena in Cosmical Physics, ed. B. Lehnert, 123–+

Syrovatskii, S. I. 1971, Sov. Phys. JETP (Engl. Transl.), 33, 933

Takakura, T., Kosugi, T., Sakao, T., Makishima, K., Inda-Koide, M., & Masuda, S. 1995, PASJ, 47, 355

Tanaka, K. & Nakagawa, Y. 1973, Sol. Phys., 33, 187

Tanaka, K., Nitta, N., & Watanabe, T. 1982, in Solar Flares, 20–+

Tang, F. 1987, Sol. Phys., 107, 233

Tousey, R., Bartoe, J. D. F., Bohlin, J. D., Brueckner, G. E., Purcell, J. D., Scherrer, V. E., Sheeley, Jr., N. R., Schumacher, R. J., & Vanhoosier, M. E. 1973, Sol. Phys., 33, 265

Tsuneta, S., Acton, L., Bruner, M., Lemen, J., Brown, W., Caravalho, R., Catura, R., Freeland, S., Jurcevich, B., & Owens, J. 1991, Sol. Phys., 136, 37

Tsuneta, S. & Naito, T. 1998, ApJL, 495, L67+

Tur, T. J. & Priest, E. R. 1976, Sol. Phys., 48, 89

Ugai, M. 1988, Computer Physics Communications, 49, 185

Uzdensky, D. A. & Kulsrud, R. M. 2000, Physics of Plasmas, 7, 4018

Vaiana, G. S., Davis, J. M., Giacconi, R., Krieger, A. S., Silk, J. K., Timothy, A. F., & Zombeck, M. 1973, ApJL, 185, L47+

van Ballegooijen, A. A. & Martens, P. C. H. 1989, ApJ, 343, 971

van Tend, W. 1979, Sol. Phys., 61, 89

van Tend, W. & Kuperus, M. 1978, Sol. Phys., 59, 115

Vasyliunas, V. M. 1975, Reviews of Geophysics and Space Physics, 13, 303

Vršnak, B., Sudar, D., & Ruždjak, D. 2005, A&A, 435, 1149

Wang, X., Bhattacharjee, A., & Ma, Z. W. 2000, J. Geophys. Res., 105, 27633

Webb, D. F., Cheng, C.-C., Dulk, G. A., Edberg, S. J., Martin, S. F., McKenna Lawlor, S., & McLean, D. J. 1980, in Solar flares, p. 471 - 499, 471–499

Webb, D. F. & Howard, R. A. 1994, J. Geophys. Res., 99, 4201

Webb, D. F. & Hundhausen, A. J. 1987, Sol. Phys., 108, 383

Wu, S. T. 1982, Space Science Reviews, 32, 115

Wu, S. T., Dryer, M., McIntosh, P. S., & Reichmann, E. 1975, Sol. Phys., 44, 117

Xu, P. & Forbes, T. G. 1992, Sol. Phys., 139, 315

Yan, M., Lee, L. C., & Priest, E. R. 1992, J. Geophys. Res., 97, 8277

Yeh, T. & Axford, W. I. 1970, Journal of Plasma Physics, 4, 207

Yokoyama, T., Akita, K., Morimoto, T., Inoue, K., & Newmark, J. 2001, Astrophys. J., 546, L69

Yokoyama, T. & Shibata, K. 1997, ApJL, 474, L61+

—. 2001, ApJ, 549, 1160

Zhang, J., Dere, K. P., Howard, R. A., Kundu, M. R., & White, S. M. 2001, ApJ, 559, 452

Zirin, H. & Tanaka, K. 1973, Sol. Phys., 32, 173

APPENDIX

Mathematica Code

Introduce Units & Physics Constants

Here we choose physical parameters in order to match to the Yokoyama & Shibata, 1997, model. All units should cancel out, so the final set of parameters (β, Lu, Ma, and λ) are all unitless.

■ Units

```
         m²
Joule = kg * ── ;
         s²

       Joule
Watt = ───── ;
         s
(* gauss=10⁻⁴ Tesla; *)
```

$$Joule = kg * \frac{m^2}{s^2};$$

$$Watt = \frac{Joule}{s};$$

(* gauss $= 10^{-4}$ Tesla; *)

■ Physical Constants

■ Proton Mass

$$m_p = 1.67 * 10^{-27} \text{ kg};$$

■ Boltzmann Constant

$$k_B = 1.38 * 10^{-23} \text{ Joule / K};$$

■ Definition of Mass Density

$$\rho_0 = n_0 * m_p;$$

■ Coronal Alfvén Speed

See Priest, Appendix II. Be careful about the inputs here, because this needs to end up unitless to not break everything.

$$V_{A0} = 2.18 * 10^{12} * B_0 * \left(\frac{1}{gauss}\right) * \left(n_0 \, m^3\right)^{-1/2} \frac{m}{s};$$

- **Model Values (in general, for the Corona)**

  - **Conduction Length Scale**

Height above Chromosphere of Diffusion Region, Y & S ' 97 give Lbox = $60 * 10^9$ cm

$$L_c = 6 * 10^8 \text{ m};$$

  - **Particle Number Density**

$$n_0 = 10^{15} \text{ m}^{-3};$$

  - **Background Field**

Chosen to match Y & S ' 97 Plasma β

$$B_0 = 21.7 \text{ gauss};$$

  - **Background Temperature**

$$T_0 = 4 * 10^6 \text{ K};$$

- **Derive & Set Model Parameters**

  - **Alfvén Speed**

`FullSimplify[V`$_{A0}$`]`

$$\frac{1.49595 \times 10^6 \text{ m}}{\text{s}}$$

  - **Plasma β**

$$\beta = \frac{2 \, k_B \, T_0}{V_{A0}{}^2 \, m_p}$$

0.0295407

  - **Conduction Coefficient**

$$\lambda = \left(9 * 10^{-12} \text{ Watt} * \text{m}^{-1} \text{ K}^{-7/2}\right) \frac{T_0{}^{7/2}}{\rho_0 \, V_{A0}{}^3 \, L_c} \frac{2}{7}$$

0.0000981224

  - **Incoming Alfvén Mach Number**

Estimated from Outflow and Inflow Velocity in Fig. 4 of Y&S.

131

```
Ma = 0.1

0.1
```

- **Lundquist Number**

```
Lu = 3.6 * 10^3

3600.
```

- **Length of Diffusion Region**

$(L_D$ and α are the same.)

$$L_D = \frac{1}{Lu * Ma^2}$$

```
0.0277778
```

Define Model Equations

- ## Set Up Relations Between Model Quantities

These relationships come, in general, from Somov (such as the Syrovatskii field) and Xu & Forbes.

- ### Field (Bx) Outside Halo Region (Background Field)

```
Bx0[x_] = -√(1 - x^2) ;
```

- ### Field (Bx) at Conduction Front

```
Bxa[x_] = Bx0[x] √(3/5) ;
```

- ### Flow Velocity in x-Direction (Vx) at Conduction Front

$$Vxa[x\_] = Vx[x] \left(1 - \frac{Bxa[x]}{Bx0[x]}\right);$$

- ### Flow Velocity in y-Direction (Vy) at Conduction Front

$$Vya[x\_] = \frac{Vxa[x] \, By[x] + Ma}{Bxa[x]} + Vxa[x] \, \partial_x a[x];$$

- ### Mass Density at Conduction Front

```
ρa[x_] = 1;
```

132

- **Pressure Outside Halo Region (Background Pressure)**

$$p[x\_] = \frac{Bx0[x]^2}{2} + \frac{\beta}{2};$$

- **Pressure at Conduction Front**

$$pa[x\_] = p[x] - \frac{(Bxa[x])^2}{2};$$

- **Temperature Inside Current Layer**

$$T[x\_] = \frac{p[x]}{\rho[x]} \frac{2}{\beta};$$

- **Sink Temperature**

```
Tsink = 1;
```

■ Set Up Model Equations

■ Ohm's Law

We can solve Ohm's Law directly and analytically, so we use it to eliminate a[x] from the numerical system.

$$a[x\_] = - \frac{Bxa[x]}{Lu\,(Ma + Vx[x] * By[x])};$$

■ Continuity Equation

$$Continuity = \partial_x\,(a[x] * \rho[x] * Vx[x]) == -\rho a[x]\,Vya[x] + \rho a[x]\,\partial_x\,a[x] * Vxa[x];$$

■ Momentum Equation

$$Momentum = \partial_x\left(a[x] * \rho[x] * (Vx[x])^2\right) + \rho a[x]\,Vxa[x]\,(Vya[x] - \partial_x\,a[x] * Vxa[x]) ==$$
$$-a[x] * \partial_x\,p[x] + Bxa[x]\,By[x];$$

■ Energy Equation

$$Energy = \partial_x\left(\left(\frac{5}{2}\,p[x] + \frac{\rho[x]}{2}\,(Vx[x])^2\right) Vx[x] * a[x]\right) - \partial_x\,a[x]$$
$$\left(\frac{5}{2}\,pa[x] + \frac{\rho a[x]\,Vxa[x]^2}{2}\right) Vxa[x] + \lambda * \left(T[x]^{7/2} - Tsink^{7/2}\right) Erf\left[\frac{x}{L_D}\right] \frac{By[x]}{Bxa[x]} ==$$
$$-\left(\frac{5}{2}\,pa[x] * Vya[x] + \frac{\rho a[x]\,Vxa[x]^2\,Vya[x]}{2} + Ma * Bxa[x]\right);$$

Work Out Initial Conditions

NDSolve requires values of Vx, By, and ρ at x = 0 in order to run. We can find these analytically, and we do so below.

■ Get Vx'[0] from Continuity

```
x = 0;
Vx[0] = 0;
Solve[Continuity, Vx'[0]];
VxPrimeCont = Re[Vx'[0] /. %[[1]]];
x =.;
Vx[0] =.;
```

■ Get By'[0] from Momentum

```
Mom2Der = ∂x Momentum;
x = 0;
Vx[0] = 0;
By[0] = 0;
Solve[Mom2Der, By'[0]];
ByPrime = By'[0] /. %[[1]];
x =.;
By[0] =.;
Vx[0] =.;
```

■ Use Vx'[0] to check By'[0]

(Not generally used, but nontheless useful in case it is needed.)

```
Vx'[0] = VxPrimeCont;
Simplify[ByPrime];
Vx'[0] =.;
```

■ Get Vx'[x] from Energy

```
x = 0;
Vx[0] = 0;
By[0] = 0;
Solve[Energy, Vx'[0]];
VxPrimeEnergy = Re[Vx'[0] /. %[[1]]];
x =.;
By[0] =.;
Vx[0] =.;
```

■ ρ[0] comes from Equality of two Vx'[0]'s

```
By[0] = 0;
Solve[Simplify[VxPrimeCont, Assumptions → {ρ[0] > 0}] ==
    Simplify[VxPrimeEnergy, Assumptions → {ρ[0] > 0}], ρ[0]];
ρZero = ρ[0] /. %[[1]];
By[0] =.;
```

■ Work Out Numerical Expressions for Initial Conditions

```
ρ[0] = ρZero;
Vx'[0] = VxPrimeCont;
By[0] = 0;
VxPrime = Simplify[Re[VxPrimeCont]];
ByPrime = Simplify[Re[ByPrime]];
ρZero = Simplify[Re[ρZero]];
By[0] =.;
Vx'[0] =.;
ρ[0] =.;
```

Solve Equations Numerically

This counts the number of iterations for the thermal conduction routines. We didn't run any yet, so it is set to zero.

```
iters = 0;
```

And then we set the domain of the region of interest.

```
xmin = 0.00001;
xmax = 1 - Ma;
```

What follows here is identical to the setup used in deriving initial values above, except we do not specify Bxa[x] so we can use the one calculated by the iterative method.

■ Set Up Bxa Separately

We begin with Bxa[x] corresponding to the I0 = 0 (or, in the case of this file, Z0=0, to avoid confusion with the Mathematica character for imaginary numbers) case.

$$
\text{Bxa}[x\_] = \text{Bx0}[x] \sqrt{\frac{3}{5}} \; ;
$$

■ Set Up Relations Between Model Quantities

We clear the values from before in case there is any residual trouble from the previous routine. Once we begin iterating, we restart the analysis after each iteration at the line below. Notice that Bxa[x] is the only value that is not reset from run-to-run.

```
Clear[T, Bx0, Vxa, Vya, ρa, p, pa, a, By, Vx, ρ]
```

■ Field (Bx) Outside Halo Region (Background Field)

$$
\text{Bx0}[x\_] = -\sqrt{1 - x^2} \; ;
$$

■ Flow Velocity in x-Direction (Vx) at Contudtion Front

$$
\text{Vxa}[x\_] = \text{Vx}[x] \left(1 - \frac{\text{Bxa}[x]}{\text{Bx0}[x]} \right) ;
$$

135

Flow Velocity in y-Direction (Vy) at Contudtion Front

$$\text{Vya}[x\_] = \frac{\text{Vxa}[x] \ \text{By}[x] + \text{Ma}}{\text{Bxa}[x]} + \text{Vxa}[x] \ \partial_x \text{a}[x];$$

- ### Mass Density at Conduction Front

  $\rho\text{a}[x\_] = 1;$

- ### Pressure Outside Halo Region (Background Pressure)

  $$\text{p}[x\_] = \frac{\text{Bx0}[x]^2}{2} + \frac{\beta}{2};$$

- ### Pressure at Conduction Front

  $$\text{pa}[x\_] = \text{p}[x] - \frac{(\text{Bxa}[x])^2}{2};$$

- ### Temperature Inside HTCS

  $$\text{T}[x\_] = \frac{\text{p}[x]}{\rho[x]} \ \frac{2}{\beta};$$

- ### Sink Temperature

  $\text{Tsink} = 1;$

■ Set Up Model Equations

- ### Ohm's Law

We can solve Ohm's Law directly and analytically, so we use it to eliminate a[x] from the numerical system.

$$\text{a}[x\_] = -\frac{\text{Bxa}[x]}{\text{Lu} \ (\text{Ma} + \text{Vx}[x] * \text{By}[x])};$$

- ### Continuity Equation

  $\text{Continuity} = \partial_x \ (\text{a}[x] * \rho[x] * \text{Vx}[x]) \ == \ -\rho\text{a}[x] \ \text{Vya}[x] + \rho\text{a}[x] \ \partial_x \ \text{a}[x] * \text{Vxa}[x];$

- ### Momentum Equation

  $\text{Momentum} = \partial_x \ \left(\text{a}[x] * \rho[x] * (\text{Vx}[x])^2\right) + \rho\text{a}[x] \ \text{Vxa}[x] \ (\text{Vya}[x] - \partial_x \ \text{a}[x] * \text{Vxa}[x]) \ ==$
  $-\text{a}[x] * \partial_x \ \text{p}[x] + \text{Bxa}[x] \ \text{By}[x];$

- **Energy Equation**

$$\text{Energy} = \partial_x \left(\left(\frac{5}{2} p[x] + \frac{\rho[x]}{2} \, (Vx[x])^2 \right) Vx[x] * a[x] \right) - \partial_x \, a[x]$$

$$\left(\frac{5}{2} pa[x] + \frac{pa[x] \, Vxa[x]^2}{2} \right) Vxa[x] + \lambda * \left(T[x]^{7/2} - Tsink^{7/2} \right) Erf\left[\frac{x}{L_D} \right] \frac{By[x]}{Bxa[x]} ==$$

$$- \left(\frac{5}{2} pa[x] * Vya[x] + \frac{pa[x] \, Vxa[x]^2 \, Vya[x]}{2} + Ma * Bxa[x] \right);$$

Run NDSolve and Set Up Solutions

■ Run NDSolve and Count How Many Steps it Takes

Here the variable **ct** is used to count the number of steps required for **NDSolve** to be completed. This code updates the step count every time that another 200 steps occur.

```
ct = 0;
solution = NDSolve[{Continuity, Momentum, Energy,
    ρ[xmin] == ρZero, Vx[xmin] == VxPrime * xmin, By[xmin] == ByPrime * xmin},
    {ρ, Vx, By}, {x, xmin, xmax}, MaxSteps → 10 000,
    StepMonitor :> If[Floor[ (ct++ + 1)/200 ] - (ct += 0)/200 == 0, Print[ct += 0]]}];
Print["Steps: ",
 ct]
```

■ Set Solution Functions

```
Vx[x_] = Vx[x] /. solution[[1]];
By[x_] = By[x] /. solution[[1]];
ρ[x_] = ρ[x] /. solution[[1]];
```

Compute Adjusted Bxa[x]

This routine executes the calculation of the improved Bxa based on conduction, and stores the old one as Bxaprevious so we can compare it to the new one and see when we have reached a steady state. This must be done numerically.

```
Bxaprevious[x_] = Bxa[x]
```

$$-\sqrt{1 - x^2} \, \sqrt{\frac{3}{5} + \frac{2}{5} \, \text{InterpolatingFunction}[\{\{0.00001, 0.90001\}\}, <>][x]}$$

■ Compute I0

See Xu & Forbes, Eq. 32

$$Z0 = \text{Interpolation}\left[\text{Table}\left[\left\{x, -\frac{\lambda * \left(T[x]^{7/2} - \text{Tsink}^{7/2}\right) \text{Erf}\left[\frac{x}{L_D}\right] \frac{By[x]}{Bxa[x]}}{Ma * Bxa[x] + \frac{5}{2} pa[x] * Vya[x]}\right\},\right.\right.$$

$$\left.\left.\{x, \text{xmin}, \text{xmax} + .001, .001\}\right], \text{InterpolationOrder} \rightarrow 25\right];$$

■ Define a New Bxa[x]

See Xu & Forbes, Eq. 27a

```
Clear[Bxa]
```

$$Bxa[x\_] = Bx0[x] \sqrt{\frac{3}{5} + \frac{2}{5} ZO[x]} ;$$

Consider Whether to Run Some More Iterations And Do It If Necessary

Now plot the new and old Bxa so we can compare and determine if the system is now steady-state. After this line, iterations begin at the **Clear** statement noted several sections above. The system has converged when the dashed and solid curves become indistinguishable.

```
iters = iters + 1
```

4

```
Plot[{-Bxa[x], -Bxaprevious[x]}, {x, xmin, xmax},
 PlotRange → {0, 1}, PlotStyle → {Dashing[{10}], Dashing[{0.03, 0.03}]}]
```